LRP 766/03 August 2003

Papers presented at the
30th EPS CONFERENCE ON CONTROLLED FUSION AND PLASMA PHYSICS

St. Petersburg, Russia
July 2003

Available in colour on the web at
crppwww.epfl.ch/archives

ISSN 0458-5895

LIST OF CONTENTS

Accessibility and Properties of ELMy H-mode and ITB Plasmas in TCV

Y.R.Martin[1], S.Alberti[1], P.Amorim[2], Y.Andrebe[1], K.Appert[1], G.Arnoux[1], R.Behn[1], P.Blanchard[1], P.Bosshard[1], A.Bottino[1], Y.Camenen[1], R.Chavan[1], S.Coda[1], I.Condrea[1], A.W.Degeling[1], V.N.Dokouka[3], B.P.Duval[1], D.Fasel[1], A.Fasoli[1,4], J.-Y.Favez[1], S.Ferrando[1], T.P.Goodman[1], M.A.Henderson[1], J.-P.Hogge[1], J.Horacek[1], P.Isoz[1], B.Joye[1], A.Karpushov[1], R.R.Khayrutdinov[3], I.Klimanov[1], J.B.Lister[1], X.Llobet[1], V.E.Lukash[5], T.Madeira[2], B.Marletaz[1], P.Marmillod[1], A.A.Martynov[1], S.Yu.Medvedev[6], J.-M.Moret[1], E.Nelson-Melby[1], P.Nikkola[1], P.J.Paris[1], A.Perez[1], R.A.Pitts[1], A.Pochelon[1], L.Porte[1], O.Sauter[1], A.Scarabosio[1], E.Scavino[1], S.-H.Seo[1], U.Siravo[1], G.Tonetti[1], M.Q.Tran[1], L.Villard[1], H.Weisen[1], M.Wischmeier[1], A.Zabolotsky[1], G.Zhuang[1]

[1]*Centre de Recherches en Physique des Plasmas, Association Euratom-Confédération Suisse, EPFL, CH-1015 Lausanne, Switzerland*
[2]*Association Euratom/IST, CFN, IST, Av. Rovisco Pais, 1049-001 Lisboa, Portugal*
[3]*TRINITI, Troitsk, Moscow Region, Russia*
[4]*PSFC, MIT, Cambridge, MA02139, USA*
[5]*RRC Kurchatov Institute, Moscow, Russia*
[6]*Keldysh Institute, Russian Academy of Sciences, Moscow, Russia*

Abstract

This paper presents experimental results on the accessibility and the properties of plasmas with improved confinement in TCV. First, the H-mode threshold power is measured in ohmic plasmas. Above an ohmic threshold density, the threshold power increases with the density. A lower threshold density is found when additional Electron Cyclotron Heating (ECH) is applied. At these low densities, the threshold power increases dramatically with decreasing density. Only a small fraction of the wide operational domain leading to the ohmic H-mode is found to lead to a stationary regime with Edge Localised Modes (ELMs). The ELMs have an irregular frequency, but in TCV they can be triggered by an external magnetic perturbation which induces a rapid vertical movement of the plasma. With this perturbation, the ELM frequency can be increased. The ELM triggering mechanism is provided by the vertical movement of the plasma away from the X-point of a single null configuration. This

movement induces a positive current at the plasma edge, and we deduce that the ELMs are being controlled by this modification of the plasma edge current.

Electron Internal Transport Barriers (eITBs) are produced deep in the plasma during the stationary phase of TCV discharges. Different scenarios of ECH or Electron Cyclotron Current Drive (ECCD) at different radial locations have been used to obtain eITBs with and without inductively driven current. The eITBs are characterised by steep electron temperature gradients, high confinement improvement and a large fraction of bootstrap current. In plasmas with fully non-inductively driven current the size and the strength of the eITB are controlled by the location of the power deposition and by the co or counter direction of the central ECCD. Finally, a small inductive perturbation of an otherwise non-inductively driven plasma current profile progressively shrinks the eITB, confirming the link between current profiles and eITBs.

1. Introduction

A fusion reactor relies on burning a high temperature plasma. Good energy confinement is required to limit the size of the reactor. Up to now, two major regimes of operation have emerged as good candidates for a reactor in view of their improved confinement properties. The so-called H-mode or 'high' confinement mode, as opposed to the 'normal' L-mode for low confinement mode, was discovered in 1982 in ASDEX [1]. Since then, this mode, characterised by an edge transport barrier, has been regularly obtained in most tokamaks [2,3,4,5,6,7,8,9,10,11,12] as well as in other magnetic confinement devices [13,14,15,16,17]. Internal Transport Barriers (ITBs) characterise the second major class of improved confinement modes [18,19,20]. The transition to either improved confinement mode is accompanied by a local suppression of turbulence. This in turn induces a local reduction in the transport

coefficients and the formation of a transport 'barrier' revealed by steep localised density and/or temperature gradients [21,22]. These improved confinement modes can even be produced together in the same plasma discharge [23,24,25] and the effect of both barriers is cumulative in the confinement improvement.

The access to improved confinement modes generally requires additional heating power. In the H-mode case, an empirical description of the access condition is widely used, based primarily on the discovery of a threshold value for the power input [26]. A scaling law for the threshold power was derived from a multi-machine comparison [27], expressed as

$$P_L = P_{OHM} + P_{AUX} - dW/dt > P_{thresh} = 0.061\, n_e^{0.62}\, B_\phi^{0.69}\, S^{0.88} \qquad (1)$$

P_L is the power flowing through the separatrix in MW, P_{OHM} the ohmic power (MW), P_{AUX} the additional absorbed power (MW), dW/dt the variation in plasma energy (MW), n_e the line averaged plasma density ($10^{20}m^{-3}$), B_ϕ the magnetic field on axis (T) and S the plasma outer surface in (m^2). This expression is calculated from experimental data taken in single null diverted plasmas with the ion ∇B drift directed towards the X point, the so-called favourable direction.

In other tokamaks, ITBs are usually produced by applying additional heating power during the plasma current ramp-up [28]. The additional heating power increases and broadens the plasma temperature profile, delaying the current diffusion into the plasma centre. This leads to a flat or hollow plasma current profile, which, in turn, leads to the formation of the transport barrier.

Although the routes to these improved confinement regimes are generally reliable, more understanding is needed to optimise the operation in such regimes. In the H-mode case, the uncertainty in the threshold power fit is still large (RMS=26%) with repercussions on the predicted ITER threshold power. On the other hand, creating an

ITB still relies, in most tokamaks, on a subtle coordination of the ramping of multiple parameters, such as the plasma current and heating power; for an ITB generated during the plasma current plateau, as demonstrated in TCV [29], an accurate control of multiple heating sources is necessary. These considerations motivate the work presented in this paper.

TCV (R=0.88m, a=0.25m, $I_p \leq 1$MA, $B_\phi \leq 1.5$T) has an unequalled plasma shaping capability ($0.9<\kappa<2.8$, $-0.6<\delta<0.9$)[30]. Together with its flexible ECH heating system (X2: 2^{nd} EC harmonic, 82.7GHz, 6 x 0.5MW, 2s, side launch; X3: 3^{rd} EC harmonic, 118GHz, 3 x 0.5MW, 2s, top launch) [31,32], it is contributing to the study of these improved confinement regimes. In TCV, L-mode to H-mode (LH) transitions are obtained with and without additional heating. Experiments have been performed to estimate the minimum threshold power in the single null diverted configuration. Results are presented in section 2.1. Different scenarios were developed to form electron internal transport barriers (eITBs) during a steady state phase of the plasma discharge. Stationary eITB plasmas with and without inductively driven plasma current are discussed in section 3.

Once a transport barrier is formed in the TCV plasma, the plasma properties may evolve considerably. In most tokamaks, LH transitions are generally followed by type III Edge Localised Modes (ELMs), which are in turn followed by an ELM free phase and then by type I ELMs as the power is increased. ELMs are classified in different types depending on the variation of their frequency with the input power and their size [33,34,35,36]. Each ELM is accompanied by a partial loss of plasma particles and energy, corresponding to a transient destruction of the transport barrier. The cyclic nature of the ELMs provides a regulation of the plasma energy, density and impurity content, which allows quasi-stationary operation in this mode. The quality of confinement during an ELM free phase causes particles and energy to accumulate in

the plasma centre, resulting generally in an uncontrolled rise in the plasma density. Plasmas in these conditions are therefore not stationary and the ELMy regime is operationally preferable. However, the particle and energy release accompanying the ELM may endanger the first wall components. Therefore, a control of the ELM energy release is necessary in a fusion reactor in an ELMy H-mode regime. Since the energy loss fraction is proportional to the time interval between ELMs [37], this control can be achieved by regulating the ELM frequency. In TCV, the coils located inside the vacuum vessel have been used to repeatedly perturb the vertical position of the plasma and thereby modify the current flowing at the plasma edge. This perturbation is observed to induce ELMs. These results are presented in section 2.2.

Once an ITB is formed, it is desirable to expand the radius of the transport barrier in order to increase the high confinement volume inside the barrier. In TCV, the radius of the deposited power is found to influence the width of the eITB and a modification of the current profile at the plasma centre is found to affect the strength of the transport barrier. Section 3.2 presents these results.

Finally, a small inductive perturbation of the plasma current profile has been imposed on a non-inductive plasma with an eITB, showing the direct link between the plasma current profile and the presence of an eITB. This experiment is presented in section 3.3.

2. H-mode

2.1 H-mode Threshold Power

In TCV ohmic discharges, the LH transitions are usually produced when the plasma becomes diverted. Such a scenario is incompatible with the widely recognised necessity to measure the threshold power during a power ramp. Therefore, specific experiments have been performed with the diverted plasma formed at low plasma

current, the plasma shape adjusted to the desired values of elongation and triangularity, κ=1.8 and δ=0.6, respectively, and the ion ∇B drift directed towards the X point. Then the plasma current is increased in steps of sufficient duration to permit full current diffusion and a stationary profile at each step. Typically, four steps are used in a single discharge, from 350 to 470kA, corresponding to edge safety factor (q_{95}) values between 2.4 and 3.3, with no problem at q_{95}=3. The plasma density is held constant during the current ramp and is varied from pulse to pulse. The toroidal magnetic field is kept constant. The ohmic power is deduced from the surface loop voltage and the variation in energy content is obtained from Thomson scattering measurements, coupled to an equilibrium reconstruction code. The measured loss power at the LH transition is $P_L = P_{OHM}$ - dW/dt. The observed density dependence of the threshold power, for these ohmic LH transitions in TCV, is fitted to a power law:

$$P_L = 0.77\ n_e^{0.69} \quad (\text{RMS}=8\%) \qquad (2)$$

with P_L in MW and n_e, the line averaged density, in $10^{20}m^{-3}$. The exponent is close to that of the ITER scaling, Eq.1, suggesting that the density dependence is similar in discharges with and without additional heating. However, the threshold power in TCV is, in average, slightly higher than the value given by the international power law scaling, as shown in Fig.1, (circles). Below an average density of 0.45 $10^{20}m^{-3}$, no LH transition was produced even when the ohmic power was raised to its maximum value, imposed by the q=2 limit. This observation is in agreement with the existence of a threshold density already reported by other tokamaks [38].

A scaling such as Eq. (1) represents the loss power, needed to obtain an LH transition for a particular density, magnetic field and plasma size. It includes an uncertainty when the RMS value of the fit is given, but does not provide any information on the probability of obtaining the LH transition. This probability can be less than 100%, since some discharges with identical plasma configuration, shape and magnetic field

did not transit into the H-mode even when their average density was higher than 0.45 $10^{20}m^{-3}$, and their loss power greater than the corresponding threshold. This indicates that additional 'hidden variables' play a significant role in the LH transition [39,40].

A few discharges were run with the toroidal field direction reversed but otherwise similar to those described above. Their threshold power was 40% higher, as shown in Fig.1(triangles). This difference can be attributed to the ion ∇B drift but is significantly lower than in other experiments in which a factor of two has been reported [41,42,43,44].

The LH threshold power was also measured in discharges with additional ECH-X2 power, and with an unfavourable ion ∇B drift. Since the ECH-X2 power has a cut-off density at 4.2 $10^{19}m^{-3}$, only densities below this value were investigated, even though this operational range does not overlap with that of the ohmic H-mode. The LH transitions produced by ECH at the second harmonic exhibit a higher threshold power than the corresponding ohmic cases, Fig.1(stars), in agreement with previous results showing that the threshold power increases with decreasing density below a given density [45]. The minimum in the threshold power is then located between these two groups of data. These experiments show that the threshold density can be lowered with the ECH but at the cost of more power.

The TCV ECH-X3 system has a higher cut-off density, 11.5 $10^{19}m^{-3}$, motivating an experiment to close the gap between the ohmic and ECH-X2 data. Two X3 gyrotrons were used, one at full power and the second with a 50% power modulation to measure the power absorbed by the plasma with a diamagnetic loop. The mirror aiming the beam at the plasma was slowly tilted during the heating pulse in order to vary the total interaction volume and thus the power absorption. An LH transition occurred when the absorbed power reached approximately 200kW. This LH transition is shown

in Fig.1(square), using the threshold power including the absorbed ECH power. This X3-assisted LH transition was obtained at a power and a density in agreement with the ohmic LH transitions. This similarity suggests that the underlying transition physics does not depend on the heating scheme and that the increase in threshold power observed in the ECH-X2 data is a general property of the low density transitions. The minimum H-mode threshold power in TCV then corresponds to the minimum value found with the favourable ion ∇B drift and was 0.45MW for this particular plasma shape, at a line averaged density of 4.5 $10^{19}m^{-3}$. The effect of the plasma shape on this minimum still has to be investigated. These results have to be compared with those obtained in other tokamaks to deduce a new threshold power scaling based on all the minima.

2.2 ELM control

A stationary ELMy regime is usually obtained soon after the LH transition when the plasma parameters are I_p=400kA, n_e=4.5 $10^{19}m^{-3}$, κ=1.7 and δ=0.6 and when the plasma becomes diverted [46]. Experiments on such an ELMy regime with additional heating have shown a reduction of the ELM frequency with increasing power [47], suggesting that these ELMs could be of type III, but other characteristics such as their amplitude, shape and energy release would suggest classifying them as type I. The irregularities in the time intervals between ELMs (Δt_{ELM}) initiated different studies: a search for determinism in the ELM series [48] and a study of the synchronisation between sawteeth and ELMs [49]. The observed correlation between the ELM amplitude and Δt_{ELM} implies that the heat flux to the divertor can be kept at a safe low level if the ELM frequency is kept high. New experiments with an external magnetic perturbation have been performed to keep the ELM frequency higher than its 'natural' value.

The perturbation consists of a series of rectangular pulses of 1ms duration, with a fixed or variable interval between pulses [50], injected into a pair of coils located inside the vacuum vessel (G coil) used for the fast vertical stabilisation of highly elongated plasmas. Because of the feedback loop, the shape of the pulse is distorted into a spike of up to 2kA which results in a rapid vertical movement of the plasma up to +/- 3mm. In order to characterise the effect of the perturbation we define the interval between pulses Δt_D, and the interval between the perturbation and the following ELM $\Delta t_{D->ELM}$.

In one experiment the perturbation was applied during the stationary phase of the plasma in 3 bursts of 200ms duration, each separated by 100ms. The perturbation frequency was constant at 200Hz. Figure 2 shows the D_α emission revealing the ELMs, the G coil current and the periods during which the perturbation is applied, the ELM frequency and $\Delta t_{D->ELM}$. At the beginning of the first perturbation burst the ELM frequency is not yet constant. Nevertheless, during two short periods before and after the ELM free phase around t=0.6s, the ELM frequency equals the perturbation frequency and $\Delta t_{D->ELM}$ remains constant. The ELM frequency returns to its 'natural' value when the perturbation is stopped. As soon as the perturbation is turned back on, the ELM frequency increases and $\Delta t_{D->ELM}$ remains constant at about 0.5ms indicating that the ELMs are synchronised to the perturbation. Three times in this second burst the locking is momentarily lost and a few ELMs are again separated by their 'natural' time delay. Locking is again lost during the following interruption of the perturbation. The ELM frequency increases just before the third perturbation burst and the synchronisation is also momentarily lost even though the ELM natural frequency becomes closer to the perturbation frequency. This might be explained by increased sawtooth-ELM interaction [51].

The synchronisation of the ELM to the perturbation is further illustrated in Fig. 3, where different signals are coherently averaged with respect to the perturbation for 3 different plasma discharges. The four rows contain, respectively, a) the input perturbation and the resulting voltage in the feedback loop, b) the G coil current, c) the vertical displacement of the plasma and d) the distribution of ELM occurrences. In the first and third columns, the perturbation is first positive then negative, whereas in the second column it is negative then positive. In the third column the plasma geometry has been reversed about the midplane with respect to the other two. This figure clearly shows that the ELMs are synchronised with the vertical movement of the plasma in the direction away from the plasma X-point. The edge current perturbation is modelled by the DINA code, a free boundary equilibrium evolution code including the transport of poloidal flux and thermal energy [52]. The simulation confirms that moving the plasma away from the positive divertor coil current induces a positive edge current by transformer action. The ELMs are therefore triggered when the plasma edge current is increased, in agreement with theoretical ELM models [53,54,55].

This also explains why in some cases the ELM frequency is decreased from its natural frequency as shown in [56]. The perturbation also induces a reduction in the edge current when the plasma movement is reversed, preventing the destabilisation of the ELM. It is only when the edge current recovers that the ELM occurs.

These experiments demonstrate that control of the ELM frequency and hence the ELM amplitude is possible. This is an important result since this perturbation technique could reduce the threat caused by the ELMs in a future reactor. However, before extrapolating this result to a reactor, this ELM control technique must be demonstrated using coils located outside the vessel. First experiments in TCV using

inboard E coils showed synchronisation but less well defined phase locking compared with the internal G coils.

3 Internal Transport Barriers

Electron Internal Transport Barriers (eITBs) are produced, in TCV, in a different operational domain from the H-mode. While H-modes are obtained at I_p=370-450kA and n_e=4.5-8 $10^{19}m^{-3}$ in diverted plasmas, eITBs are created in either limited or diverted plasmas at I_p=80-200kA and n_e=0.8-2 $10^{19}m^{-3}$. At these low densities, the electron-ion collision frequency is very low and, when heated, the electrons remain decoupled from the ions. The resulting barrier appears in the electron channel (eITB).

Two operational scenarios are regularly used in TCV, one with inductively driven current and the other with fully non-inductively driven current. In both scenarios, the eITB formation is initiated during the stationary plasma current plateau, unlike the more usual current ramp scenarios used in other tokamaks. ECH, in the inductive case, or co-ECCD (ECCD in the direction parallel to the plasma current), in the non-inductive case, is applied to the stationary target plasma away from the magnetic axis (off-axis), in order to broaden the temperature profile and consequently the current profile.

The temperature profile evolves quite rapidly (~5ms) during the formation of the eITB compared to the current redistribution time and the duration of the discharge. However, in contrast to the formation of an H-mode, no clear transition is observed: rather, the profiles evolve continuously. A parameter used to describe the eITB characteristics is

$$\rho_T^*(R,t) = \rho_s(R,t) / L_{Te}(R,t) \qquad (3)$$

where $L_{Te} = -T_e / (\partial T_e/\partial R)$ is the local temperature gradient scale length, T_e the electron temperature, R the plasma major radius on the equatorial plane, $\rho_s = c_s/\omega_{ci}$

the ion Larmor radius at the sound speed, c_s the ion sound speed and ω_{ci} the ion cyclotron frequency [57]. The strength of the ITB is quantified by the maximum value of the ρ_T^* profile: $\rho^*_{max}(t) = max_R(\rho_T^*(R,t))$ and its location by $\rho_{\rho^*}(t) = \rho_{vol}(\rho^*_{max}(t))$ where ρ_{vol} is the volume normalised radius.

3.1 ITB in plasmas with inductively driven current

In the inductively driven scenario, ECH is applied off-axis, at ρ_{vol}=0.4, to a stationary ohmic plasma, causing the temperature profile and consequently the current profile to broaden [58, 59]. Central Counter-ECCD is then applied either with a slow ramp or after a delay of the order of the current redistribution time (~0.2s) to increase the pressure profile, creating an eITB with steep gradients and large bootstrap current, I_{BS}. Up to 1MW of ECH and 1.5MW of Counter-ECCD were injected into 200kA plasmas, leading to very high central temperatures, $T_e(0)$=15-18keV and very steep electron temperature gradients, ρ^*_{max} =0.2. The transport barrier is located at ρ_{ρ^*} =0.4.

The electron energy confinement time increases during the creation of the eITB despite the simultaneous increase of the additional power. Once the eITB is formed, its properties remain constant for as long as the duration of the power pulse, typically over 300 energy confinement times. The quality of the confinement is described by the parameter H_{RLW}, the ratio of the measured confinement time over the confinement time estimated from the Rebut-Lallia-Watkins (RLW) confinement scaling [60]. The RLW scaling is used here because it is appropriate for a hot electron, cold ion regime and it accurately describes TCV ohmic plasmas [61]. In these eITB experiments, H_{RLW} can reach 4.5, highlighting the remarkable confinement properties of the eITB, even if the volume inside the transport barrier is small. The improvement in confinement can also be expressed relative to the ITER-98-L scaling [62]. The ratio

of the measured energy confinement to this scaling is approximately 1.6 in these discharges with eITBs.

The plasma current was varied from discharge to discharge while keeping the same ECH and ECCD powers and launching geometries to create the eITB. The major difference between the resulting eITBs is in their radial position. At high plasma current (200kA) the eITB radius was smaller (ρ_{ρ^*} =0.2) than at lower current (120kA, ρ_{ρ^*}=0.35) [63]. This is because the ohmic contribution to the total plasma current is peaked at the plasma centre and tends to oppose the current profile flattening. Moreover, more ECH and ECCD power is required to obtain the same efficiency in higher current plasmas.

In this current scan, the energy fraction contained within the eITB is higher for low plasma current since the eITB volume is larger. The confinement time, however, is roughly constant in the 3 cases, since the effect of the modification in the eITB volume is compensated by the inherent confinement increase with increasing plasma current. Relative to the RLW scaling, however the confinement improvement is more pronounced at low plasma current.

3.2 ITB in plasmas without inductively driven current

The other technique to produce eITBs consists of tailoring the plasma current profile by fully sustaining the current with co-ECCD off-axis. In these experiments, an ohmic plasma of about 80 - 100kA is created in TCV. The 1MW ECCD power drives a current equal to the initial ohmic current. The feedback on the plasma current is turned off, the current in the ohmic transformer is held constant and the loop voltage (V_{loop}) drops to zero. Typically, 500kW off-axis ($0.3<\rho<0.5$) ECCD can drive a current of about 30kA at the optimum ECCD injection angle through a combination of direct drive and bootstrap current generation [64]. After a delay of about 0.2s,

necessary for current profile redistribution, a flat current profile is obtained out to the power deposition radius, resulting in reduced central heat conductivity and in the formation of an eITB. ECH or counter-ECCD is then applied on axis, in the good confinement region, to further increase the central temperature. The electron temperature gradient increases at the transport barrier, reinforced by an increase of up to 20kA in the local bootstrap current [65], generated by the strong T_e gradient. This large contribution of the bootstrap current to the current profile leads to eITBs lasting for hundreds of confinement times and central temperature and H_{RLW} factors up to 5keV and 5.

The influence of the co-ECCD deposition radius was investigated in a series of discharges in which the deposition location was varied between $\rho_{co\text{-}ECCD}$=0.3 and $\rho_{co\text{-}ECCD}$=0.45. A discharge with the co-ECCD power deposited at the plasma centre, without an eITB, is used as a reference. The eITB radius, ρ_{ρ^*}, expands with the deposition location as shown in Figure 4. This is because, as $\rho_{co\text{-}ECCD}$ increases, the maximum in the pressure gradient moves outwards, increasing the bootstrap current, which in turn pushes the eITB further out, increasing both ρ_{ρ^*} and ρ^*_{max}. The increase in both of these parameters in turn causes an enhancement of H_{RLW} from 2 to 5.

The bootstrap current in these discharges is estimated from the T_e and n_e profiles. Its contribution to the total current increases with the EC power deposition radius, as shown in Fig.5, through the increase in the volume of the steep gradient region. The contribution from co-ECCD is then deduced from the total current and the bootstrap fraction. This contribution decreases with increasing EC power deposition radius, since the ECCD efficiency is a decreasing function of minor radius. In order to extend the ITB radius further, it will be necessary to either increase the co-ECCD power or increase the radius of the co-ECCD deposition during the plasma discharge.

The primary role of central ECH is to heat the good confinement region to increase the plasma energy content, but we find that counter-ECCD is even more efficient at doing this [66]. To illustrate this, a fine scan of the toroidal angle of the central ECH injection from 5° in the co direction to 5° in the counter direction was performed. In this scan, the ITB strength ρ^*_{max} increased from 0.33 to 0.5 as shown in Fig.6 and the radial location of the ITB remained approximately constant near ρ_{ρ^*}=0.45. The H_{RLW} factor increased along with ρ^*_{max}.

We have thus shown that the radial position of the co-ECCD power deposition and the toroidal angle of the ECH injection are two independent parameters, which strongly influence the eITB position and strength. These parameters can therefore be used separately for eITB control. The eITB radius can be adjusted by the co-ECCD deposition location. The eITB strength will also be influenced, but it can then be independently controlled by the ECH toroidal angle of injection.

The dependence of H_{RLW} on ρ^*_{max} and ρ_{ρ^*} has been characterised empirically by a figure of merit $\rho^*_{max} \cdot \rho_{\rho^*}^2$. Figure 7 shows the correlation between this figure of merit and H_{RLW} for the results of both inductive and non-inductive scenarios.

3.3 ITB perturbation with ohmic current

A new method to illustrate the direct relationship between the current profile and the eITB has been used on TCV. In scenarios in which eITBs are fully sustained with ECCD, the ohmic transformer can be used to impose a constant current perturbation. The ohmic transformer current is changed from a constant value to a constant slope of 2kA/s, corresponding to a loop voltage of about 0.12V and an induced current of 40kA. The perturbed power, 5kW, is negligible compared with the 1.4MW ECH power injected into the plasma.

This perturbation was applied to a well established eITB with a strongly reversed shear q profile resulting from the 50kA off-axis bootstrap current. The induced current perturbation penetrates through the plasma minor radius and results in a strongly peaked current density contribution, proportional to the $T_e^{3/2}$ profile, which can decrease or eliminate the strong reversed shear. Consequently the eITB decreases in strength and in radius, as shown in Fig.8, and the confinement decreases accordingly. This degradation in the eITB parameters and in the confinement takes place on a long time scale (~0.6s). The bootstrap current slowly decreases as well, indicating that these quantities are linked by a feedback loop characterised by a slow time constant: a current profile modification induces a change in the confinement, which induces a change in the pressure profile, which leads to a variation of the bootstrap current, which changes in turn the current profile. This 'negative' experiment, in which the eITB is lost, is a clear demonstration of the direct dependence of confinement time on the current profile, independent of the total power, held constant. In all other experiments presented here this loop was 'positively' used since the heating and the current drive were used to increase the temperature gradients to increase the bootstrap current, leading to more reversed current profiles and finally to increased confinement.

Conclusions

Enhanced confinement regimes, both H-mode and eITB, are routinely produced in TCV. The H-mode is accessible with and without additional ECH power. A threshold density of about 4.5 $10^{19}m^{-3}$ is found in the ohmic case. LH transitions are obtained at lower densities with ECH, but the total input power has to be increased considerably. The minimum threshold power is 0.45MW.

The ELM frequency has been increased and controlled by an external magnetic perturbation, which induces a vertical plasma displacement, which in turn induces a

brief variation in the plasma edge current. The ELMs are synchronised to the increased $\mathbf{j}_{edge}$. This proves the importance of the plasma edge current in the ELM trigger mechanism and its possible use in ELM control.

Electron ITBs have been formed without a current ramp, during the steady-phase of ohmic discharges by current profile tailoring both with and without inductively driven current. In both cases, the bootstrap current contributes significantly to a broadening of the plasma current profile. High central temperatures, above 15keV, and confinement improvement, H_{RLW}, of up to 4 have been obtained in the inductive case. In the non-inductive case, the energy confinement time was smaller than in the inductive case because of the smaller total plasma current, but the relative improvement was larger since the absence of ohmic current leads to broader current profile and therefore wider eITBs. The eITB radius and strength have been controlled by the co-ECCD deposition radius. The eITB strength has also been controlled by the toroidal direction of the central heating beams. Finally, an experiment in which the eITB in a non-inductive plasma vanishes progressively due to an inductive perturbation has proven the direct and delicate relationship between the current profile and the confinement.

Acknowledgements

Special thanks are due to the whole TCV team for its effort in support of our research. This work was partly supported by the Swiss National Science Foundation.

Figure captions

Figure 1: Loss power ($P_L = P_{OHM} + P_{AUX} - dW/dt$) as a function of the threshold power estimated from the ITER scaling ($P_{thresh} = 0.061\ n_e^{0.62}\ B_\phi^{0.69}\ S^{0.88}$) at the LH transition for different cases: circles=Ohmic with favourable ion ∇B drift;

triangles=Ohmic with unfavourable ∇B; square=ECH (X3) with favourable ∇B; stars=ECH (X2) with unfavourable ∇B.

Figure 2: Evolution of D_α emission, internal coil current, ELM frequency and ELM phase relative to the perturbation in a discharge with three perturbation phases indicated by rectangles in the second box from the top.

Figure 3: Perturbation voltage, internal coil current and plasma vertical displacement coherently averaged over the perturbation phase and histogram of the interval between perturbation and ELM for three discharges with different perturbation signs and different plasma configurations: 20333=positive then negative (+/-) perturbation in Single Null Down (SND) plasma; 20334= -/+ perturbation in SND plasma; 22768=+/- perturbation in SNU (up) plasma. The ELM are synchronised with a vertical speed away from the X-point.

Figure 4: ITB strength (ρ^*_{max}) and radius (ρ_{ρ^*}) as a function of the co-ECCD deposition radius in fully non-inductive discharges.

Figure 5: Contributions to the total plasma current (I_P) from co-ECCD (I_{CD}) and bootstrap (I_{BS}) as a function of the co-ECCD deposition radius in fully non-inductive discharges.

Figure 6: ITB strength (ρ^*_{max}) and radius (ρ_{ρ^*}) as a function of the toroidal angle of the injection of the on-axis heating in fully non-inductive discharges.

Figure 7: Improvement in confinement relative to the Rebut-Lallia-Watkins scaling against a figure of merit, $\rho^*_{max} \cdot \rho_{\rho^*}^2$, which describes the quality of the eITB, for discharges with and without inductive current.

Figure 8: Evolution of ρ^*_T : A) before the induced current perturbation. B) 0.2 s after the beginning of the perturbation. C) 0.8s after the beginning of the perturbation.

References

1 F.Wagner, G.Becker, K.Behringer et al. PRL **49** (1982) 1408
2 ASDEX Team, NF 29 (1989) 1959
3 A.Tanga et al. Proc IAEA Conf. on PPCF research, Kyoto, 1986
4 S.J.Fielding, P.G.Carolan, J.W.Connor et al, NF **41** (2001) 909
5 M.Greenwald, R.L.Boivin, F.Bombarda et al, NF 37 (1997) 793
6 N.Oyabu et al, NF 25 (1985) 49
7 K.H.Burrell, S.L.Allen, G.Bramson et al, PPCF 31 (1989) 1649
8 R.J.Groebner et al. PPCF 36 (1994) A13
9 M.Akiba et al. PPCF 30 (1988) 1405
10 G.R.Tynan et al. PPCF 36 (1994) A285
11 F.Hofmann et al. PPCF 36 (1994) B277
12 J.-M.Moret et al. PPCF 37 (1995) A215
13 V.Erckamnn et al PRL 70 (1993) 2086
14 F.Wagner et al, PPCF 36 (1994) A61
15 K.Toi et al, PPCF 36 (1994) A117
16 N.Ohyabu et al., PRL 84 (2000) 103
17 C.E.Bush, M.G.Bell, R.E.Bell et al, POP Vol.10, Num.5 (2003), 1755
18 S.Ide et al. PPCF 44 (2002) A137
19 T.Fukuda and JT-60U Team, PPCF 44 (2002) B39
20 B.Esposito et al. PPCF 45 (2003) 933
21 E.Joffrin et al. PPCF 44 (2002) 1739
22 E.J.Doyle et al. NF 42 (2002) 333
23 P. Gohil et al. PPCF 45 (2003) 601
24 J.E.Rice et al. NF 42 (2002) 510
25 S.V.Neudatchin et al. PPCF 44 (2002) A383
26 K.H.Burrell, S.L.Allen, G.Bramson et al, PPCF 31 (1989) 1649 - cf plus haut
27 F.Ryter, H-Mode Threshold Database Group, PPCF **44** (2002) A415
28 E.Joffrin et al. PPCF 44 (2002) 1739 - cf plus haut
29 Z.A.Pietrzyk et al. POP Vol.7 N.7 (2000) 2909
30 F.Hofmann, J.B.Lister, M.Anton et al, PPCF 36 (1994) B277 - cf plus haut
31 T.P.Goodman et al. Fusion Techn., proc. 19th SOFT (1996) Vol1, 565
32 J.P.Hogge et al. Proc. 12th Joint Workshop on ECE and ECRH, Aix-en-Provence (2002)
33 T.Kass et al. NF 38 (1998) 111
34 W.Sutttrop, PPCF **42** (2000) A1
35 H.Zohm, PPCF **38** (1996) 105
36 J.W.Connor PPCF 40 (1998) 191
37 A.W.Degeling et al. PPCF 43 (2001) 1671
38 T.Carlstrom, PPCF 38 (1996) 1149
39 T.Fukuda, PPCF 40 (1998) 543
40 Y.R.Martin et al. 18th IAEA-FEC, Oct. 2000, Sorrento, Italy, IAEA-CN-77/EXP5-14
41 ASDEX Team, NF **29** (1989) 1959
42 F.Ryter, W.Suttrop, B.Brüsehaber et al, PPCF 40 (1998) 725
43 J.G.Cordey, W.Kerner, O.Pogutse and A.Nassigh, PPCF **38** (1996) 1905
44 T.N.Carlstrom, K.H.Burrel and R.J.Groebner, PPCF **40** (1998) 669

45 S.J.Fielding, J.D.Ashall, P.G.Carolan et al, PPCF **38** (1996) 1091
46 Y.R.Martin et al. 18th IAEA-FEC, Oct. 2000, Sorrento, Italy, IAEA-CN-77/EXP5-14
47 L.Porte, S.Alberti, G.Arnoux et al. 19th IAEA-FEC, Oct. 2002, Lyon, France, IAEA-CN-94/EX/P5-15
48 A.W.Degeling et al. PPCF 43 (2001) 1671 cf plus haut
49 Y.R.Martin, A.W.Degeling, J.B.Lister, PPCF 44 (2002) A373
50 A.W.Degeling, Y.R.Martin, J.B.Lister et al. PPCF special issue December 2003
51 A.W.Degeling, Y.R.Martin, J.B.Lister, this conference: Europhysics Conference Abstracts Vol27XXX, P3-128
52 R.R.Kayrutdinov and V.E.Lukash, J. Comp. Phys. **109** (1993) 193
53 J.W.Connor PPCF 40 (1998) 191 - cf plus haut
54 J.W.Connor et al. PoP Vol.5 N.7 (1998) 2687
55 S.Saarelma et al. PPCF 42 (2000) A139
56 A.W.Degeling, Y.R.Martin, J.B.Lister et al. PPCF special issue December 2003, cf plus haut
57 G.Tresset, X.Litaudon, D.Moreau et al, NF 42 (2002) 520
58 Y. Camenen, A. Pochelon, F. Hofmann et al, Proceedings of the 12th Joint Workshop on ECE and ECRH, May 12-15th, 2002 Aix-en-Provence, p. 407.
59 A. Pochelon, G. Arnoux, Y. Camenen, et al., 19th IAEA-FEC, Oct. 2002, Lyon, France, IAEA-CN-94/EX/P5-14
60 P.H.Rebut, P.P.Lallia, M.L.Watkins, Proc. 12th Int. Conf. on Plasma Phys. and Contr. Fusion Research (IAEA, Nice, 1988) Vol.2, p.191
61 A.Pochelon et al. NF 39 (1999) 1807
62 K.Thomsen et al. 17th IAEA-FEC, Oct. 1998, Yokohama, Japan, IAEA-CN-69/ITER/3-ITERP1/07
63 R.Behn, this conference: Europhysics Conference Abstracts Vol27XXX, P3-208
64 O. Sauter et al. PoP Vol.8 N.5 (2001) 2199
65 A.G.Peeters, PPCF 42 (2000) B231
66 M.A.Henderson et al. PoP Vol.10 N.5 (2003) 1796

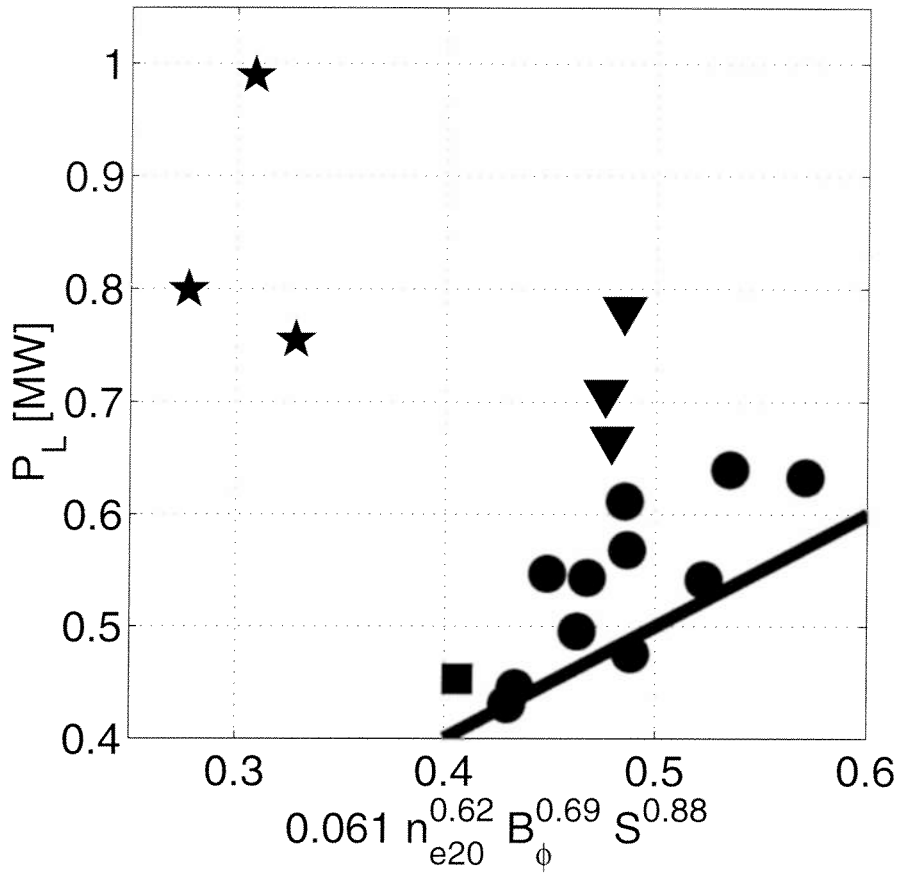

Figure 1

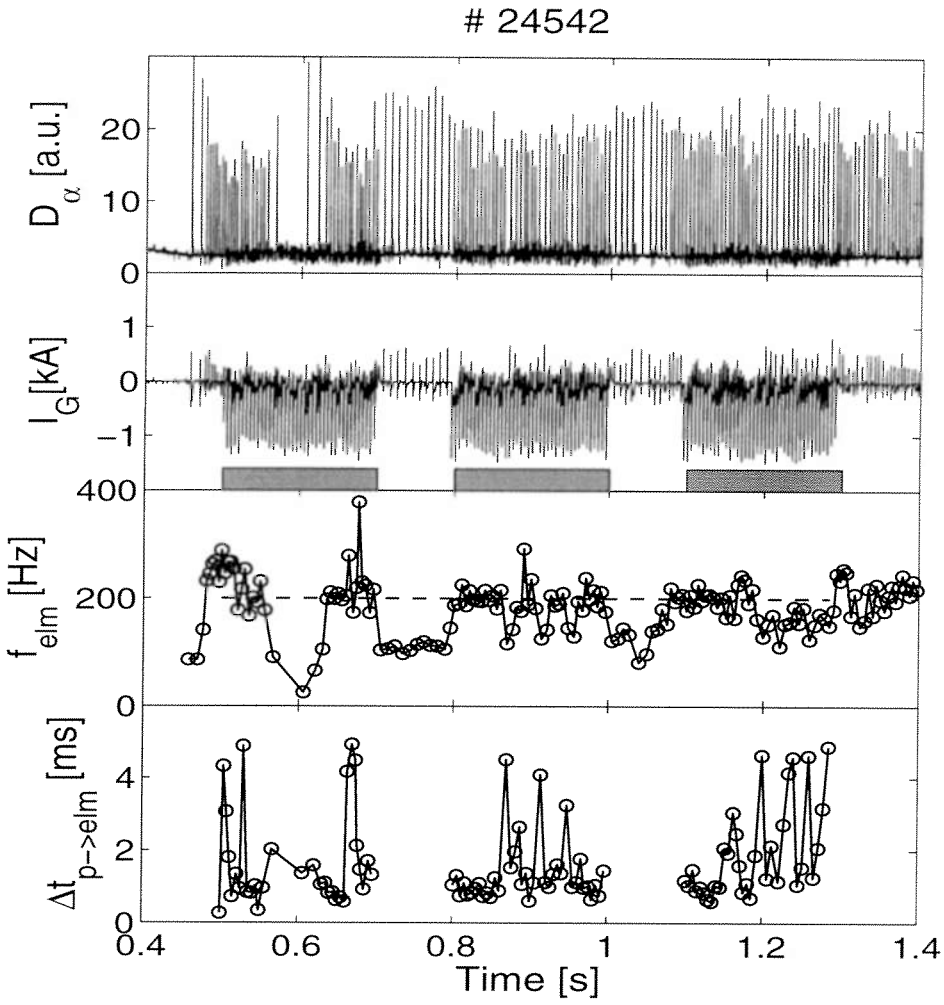
24542
D_α [a.u.]
20
10
0
I_G[kA]
1
0
−1
400
f_{elm} [Hz]
200
0
$\Delta t_{p->elm}$ [ms]
4
2
0
0.4
0.6
0.8
1
1.2
1.4
Time [s]

Figure 2

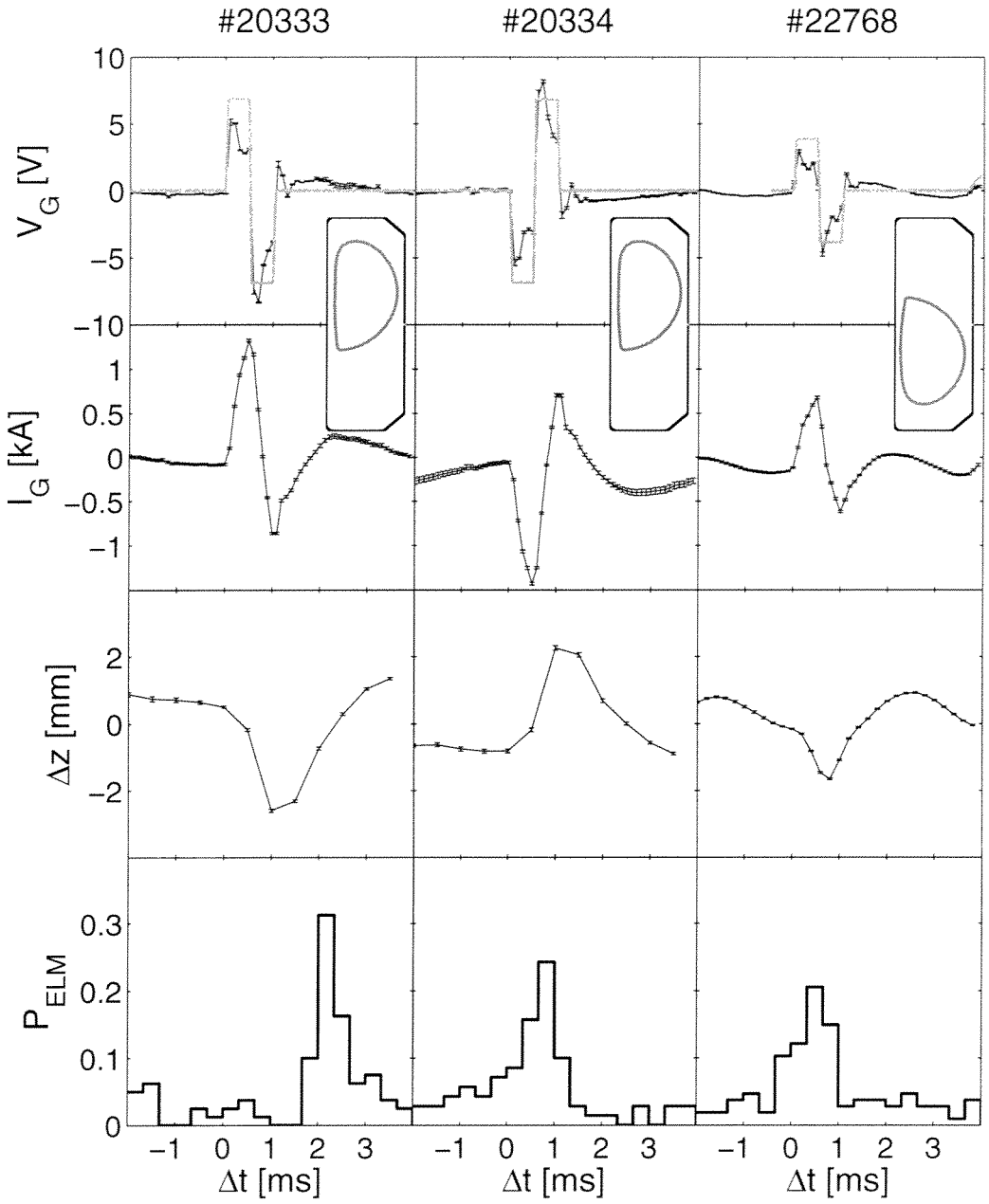

Figure 3

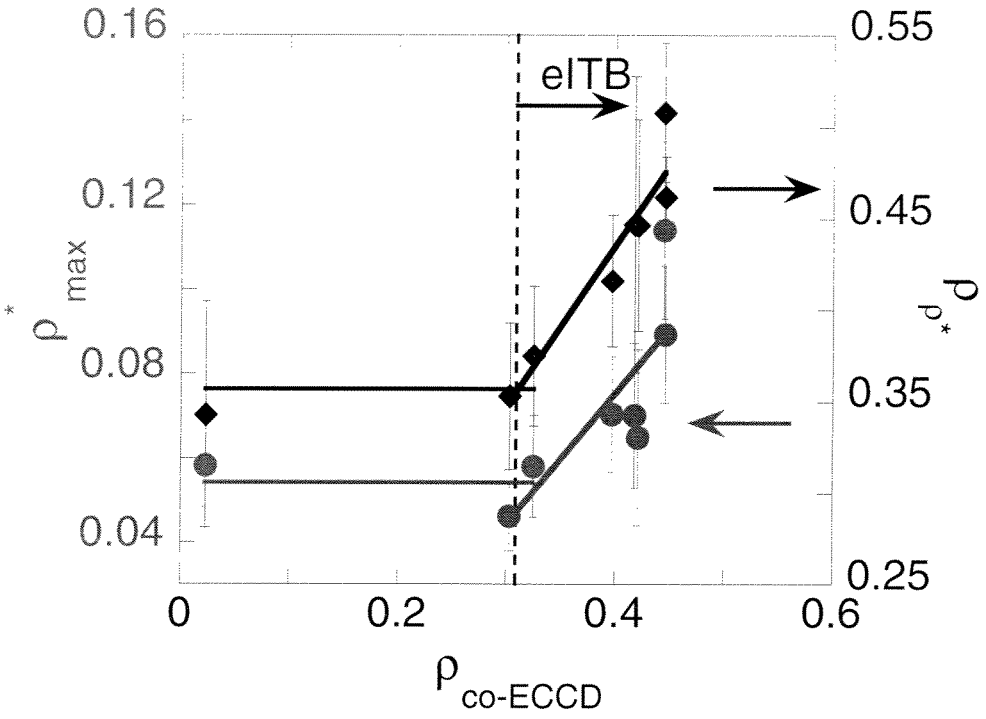
0.16
0.12
0.08
0.04
0.55
0.45
0.35
0.25
0
0.2
0.4
0.6
eITB
ρ^*_{max}
ρ^*_p
$\rho_{co\text{-}ECCD}$

Figure 4

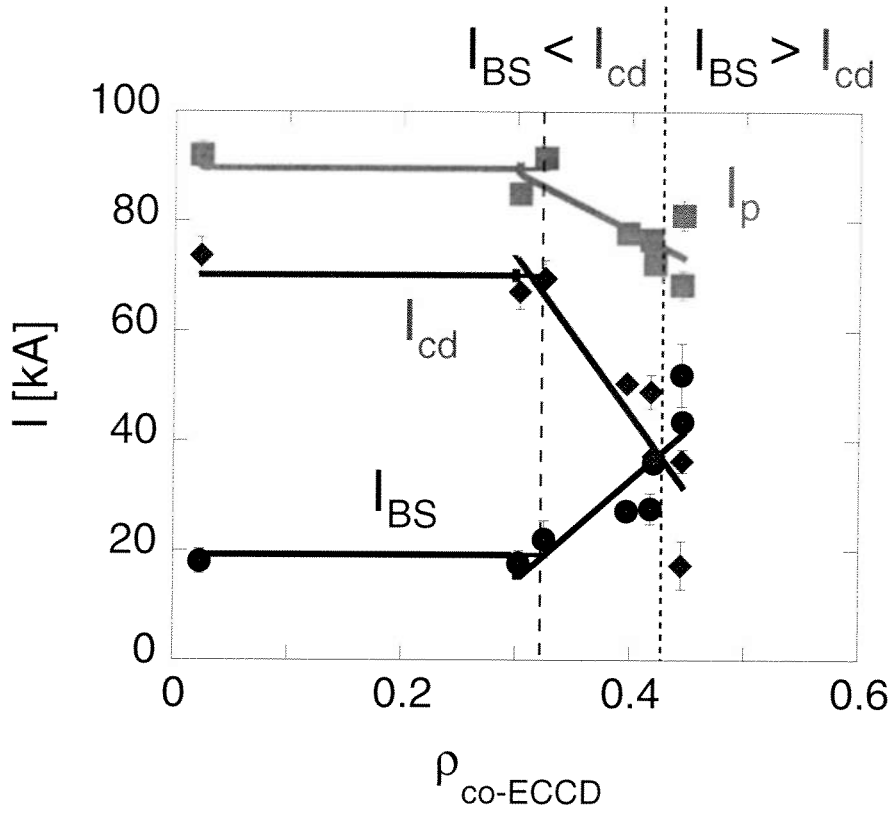
$I_{BS} < I_{cd}$
$I_{BS} > I_{cd}$
100
80
60
40
20
0
I [kA]
I_p
I_{cd}
I_{BS}
0
0.2
0.4
0.6
$\rho_{co\text{-}ECCD}$

Figure 5

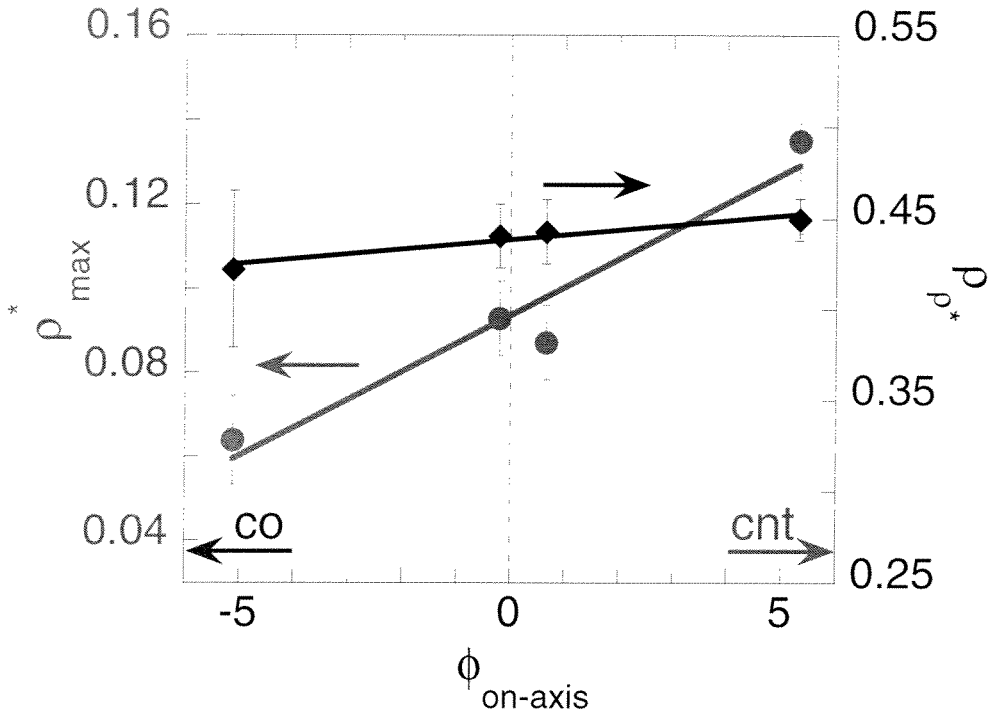
0.16
0.12
0.08
0.04
ρ^*_{max}
0.55
0.45
0.35
0.25
ρ^*_{ϕ}
co
cnt
-5
0
5
$\phi_{on\text{-}axis}$

Figure 6

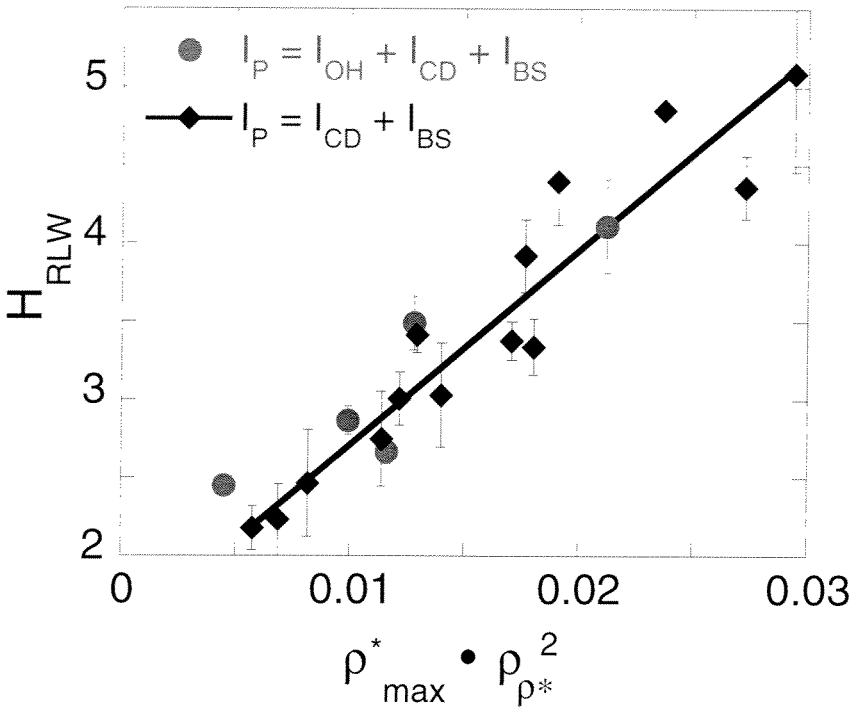
$I_P = I_{OH} + I_{CD} + I_{BS}$
$I_P = I_{CD} + I_{BS}$
H_{RLW}
5
4
3
2
0
0.01
0.02
0.03
$\rho^*_{max} \bullet \rho_{\rho*}^2$

Figure 7

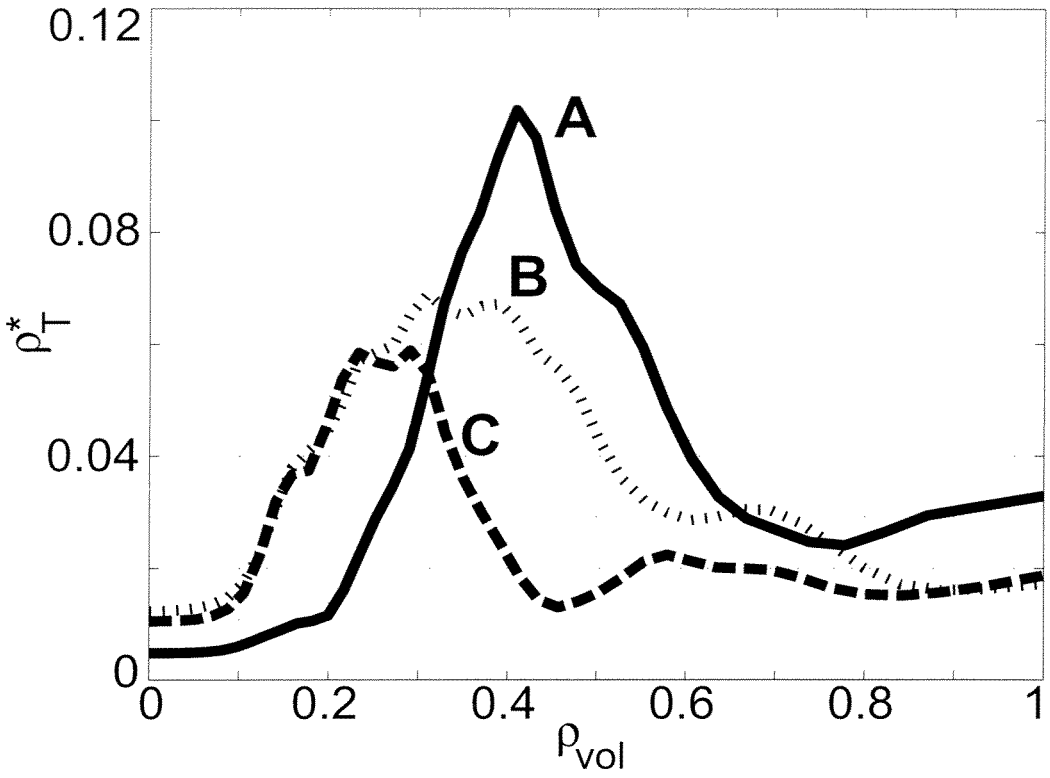

Figure 8

Formation of eITBs in EC-Heated TCV Plasmas with and without Inductively Driven Current Component

R. Behn, O. Sauter, M. Henderson, T. Goodman, G. Zhuang, Y. Camenen, A. Scarabosio, S. Coda, I. Condrea, P. Nikkola, A. Pochelon
Centre de Recherches en Physique des Plasmas,
Association EURATOM-Confédération Suisse, EPFL, Lausanne, Switzerland

The formation of internal transport barriers (ITBs) has given access to new regimes of improved energy confinement in fusion plasma devices. In the case of dominant heating by electron cyclotron (EC) waves, barriers in the electron transport channel (eITBs) will determine the confinement. Theoretical models attribute the formation of a barrier to a local reduction of anomalous transport via stabilisation of turbulence. The suggested mechanisms involve current profile shaping and q-profiles with reversed shear.
Experimental studies on TCV, supported by theoretical modelling, have been carried out to investigate different scenarios combining ECH and ECCD to obtain eITBs and improved electron energy confinement. The TCV device is well suited for these investigations, since it is equipped with a powerful EC heating system comprising 6 gyrotrons (82.7GHz, 2nd harmonic) with a maximum power of 3MW. Each source can be used either for pure EC heating or current drive (ECCD) by changing the toroidal injection angle of the beams. The special design of the launchers gives flexibility for local power deposition within the plasma cross section. Scenarios of eITB formation in TCV during a phase with constant plasma current can be divided into two categories :
I) As long as a strong inductively driven current component is maintained, the desired shaping of the current density profile is achieved by a combination of off-axis ECH followed by strong counter ECCD in the centre. Heating off-axis broadens the T_e profile and via a change in resistivity also the current density profile on a resistive time scale, as can be seen from the change of plasma inductance. Subsequent power deposition in the centre combined with counter ECCD leads to T_e profiles which clearly reveal the formation of a transport barrier. Using a description in terms of a normalised gradient scale length (ρ^*_T) [1] the evolution of the barrier in space and time can be followed. A value of $\rho^*_T > 0.06$ is taken as indicator for an eITB.
Fig.1 shows a contour plot of ρ^*_T with an eITB obtained in a plasma with the following parameters :

I_p 120kA, $n_{e,avg}$ $1.10^{19}m^{-3}$, κ 1.5.
P_{ECH} 0.9MW, P_{ECCD} 0.9MW

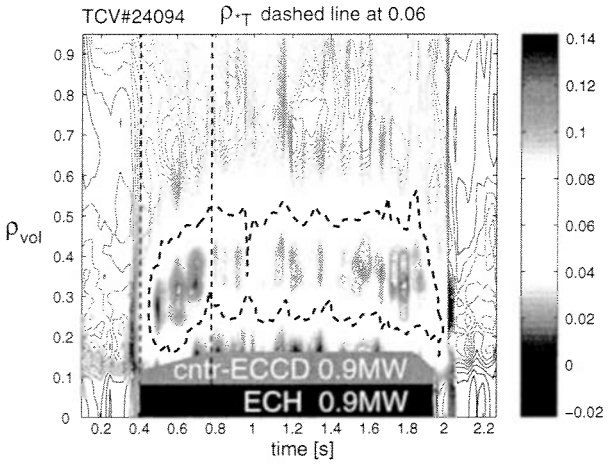

Fig. 1
Variation in space and time of the normalised gradient of T_e (ρ_s / L_T) for shot 24094 with a stable ITB near the normalised radius $\rho_{Vol} \approx 0.35$

In the particular case, we observe that the eITB slowly expands during the time interval with increasing counter ECCD deposited in the centre. During this phase the current profile still evolves due to the increasing ECCD and bootstrap current densities.

At the end of the power ramp, a stationary phase is reached with the ITB at a fixed location. The T_e profiles measured by Thomson scattering (spatial resolution of ≈4cm along a vertical axis) at various times during the shot (#24094) are shown in fig.2.

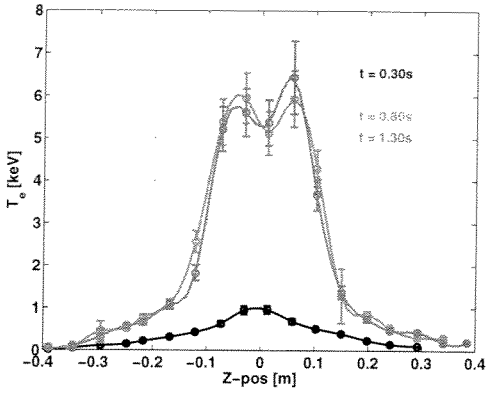

Fig. 2 (above)
T_e profiles from Thomson scattering for shot 24094 with a stationary ITB (see time markers in fig.3)

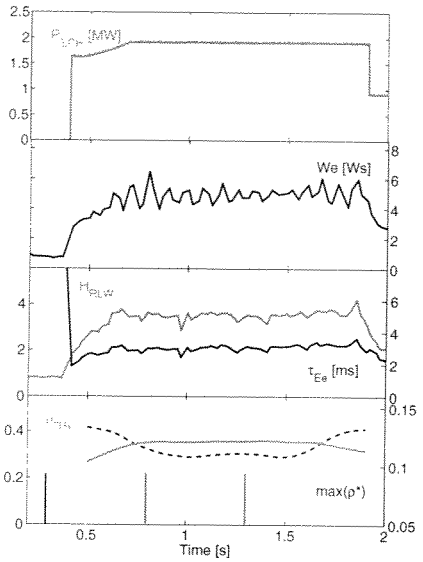

Fig. 3 (right)
Total EC-power, $T_e(0)$, global confinement and ITB parameters (location and strength) for shot 24094

As can be seen on fig.3, the energy confinement gradually improves during the power ramp and finally an H-factor (reference RLW scaling) near 4 is maintained for the full duration of the EC pulse, which correponds to > 300 $\tau_{E,e}$.
The close link between q-profile and location of the eITB can be inferred from the results of a series of similar shots at different I_p (200kA, 120kA), with all other plasma parameters all well as the heating and current drive scheme kept constant (see fig.4a,b).

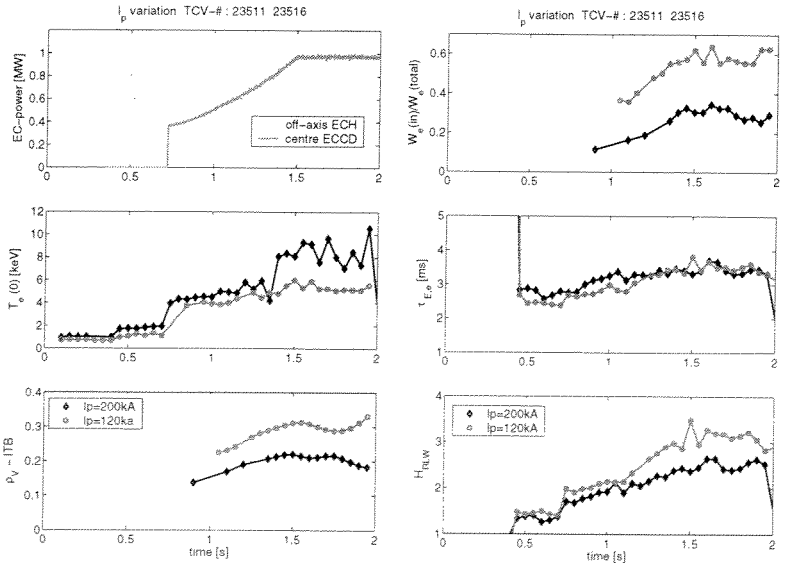

Fig. 4
Variation of I_p (200kA, 120kA)
a) EC-power
off-axis ECH
central ECCD
$T_e(0)$
location of ITB

b) electron energy
inside ITB
confinement time
H-factor (RLW)

At fixed heating power, the ITB tends to shrink at higher plasma current. As a consequence, the energy fraction inside the barrier decreases, which affects the global confinement parameters. We note that $\tau_{E,e}$ changes very little in spite of the predictions of the scaling laws.

Further investigations have been directed towards the goal of widening the zone inside the eITB even in the presence of a large ohmic current component. Starting from an established ITB at relatively low current (I_p=120kA), the plasma elongation was increased dynamically during an I_p ramp. At the same time the EC power used for counter CD in the centre was increased. During this phase a drop in l_i was observed indicating a broadening of the current density profile. Under these conditions the ITB moved further out and a large central zone with improved energy confinement was formed. The effect on the global confinement parameters is remarkable, with an H-factor > 6 and an increase in energy confinement time by >60%. So far, this performance could only be achieved during a transient phase, which was terminated by mode activity. Future experiments will have to show whether optimisation of the central power deposition permits to stay below the critical pressure and reach stable conditions.

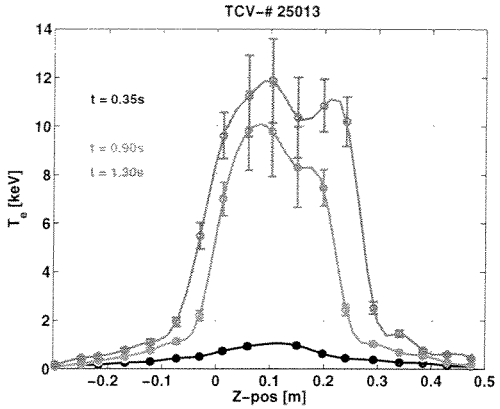

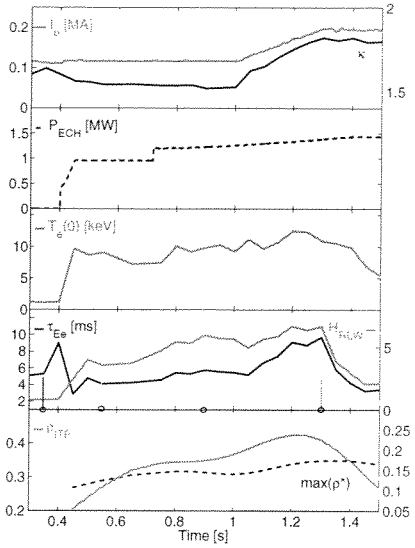

Figs 5 & 6
T_e profiles and confinement properties of TCV #25013 showing outward shift of ITB during simultaneous increase of κ and I_p

II) Scenarios with fully non-inductive current drive by ECCD offer more flexibility for controlled tailoring of the current density profile. As has been shown in the past [2,3], reversed shear is a precondition for substantial confinement improvements with H-factors > 4. Simulations using the Fokker-Planck code CQL3D have also revealed the importance of the bootstrap current. These calculations, which take into account radial diffusion of fast electrons, show that off-axis co-ECCD is not sufficient to produce a hollow j(r) profile. It is found that the bootstrap current density with an off-axis maximum will determine the final shape of the total current density profile [3]. This has important consequences on the stability of the eITB. Once it is formed at a particular radial position, which can be influenced by local co-ECCD (see below), adding more power in the centre will increase the pressure gradient, drive more bootstrap current and reinforce the barrier.

Fig.7 summarizes the results from a series of experiments with different conditions of power deposition. Changing the toroidal launching angle of the beams directed at the centre from co to counter ECCD has a pronounced effect on ρ^*_T at the barrier (see fig 7a). The strongest barrier and highest H-factor (≈4.5) are obtained with a small amount of central counter ECCD and are attributed to larger shear reversal [2]. As shown in fig.7b, the radial position of the ITB can be influenced by local off-axis co ECCD. It has been observed [4] that the barrier forms at a larger radius if the CO-ECCD beams are moved further off-axis. An influence on the strength of the barrier, expressed by the maximum value of ρ^*_T, is also present.

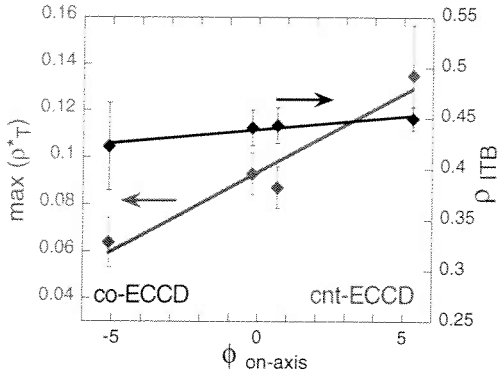

Fig 7a *Influence of central power deposition on ITB parameters*

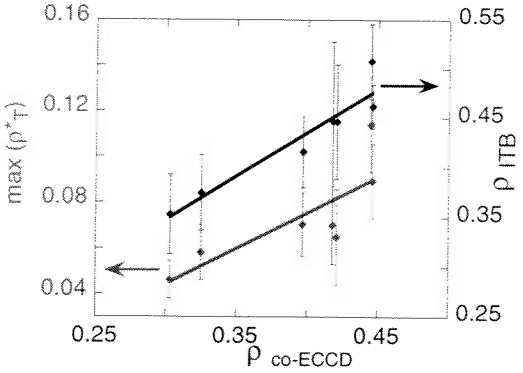

Fig 7b *Influence of off-axis ECCD on ITB parameters*

III) New insight into the direct relation between the q-profile and the eITB has been gained from recent experiments performed on TCV. Starting from a scenario with an eITB and fully non-inductive current drive, the ohmic transformer is used to provide an inductive current perturbation, which penetrates through the plasma minor radius in about 200ms. This corresponds to a loop voltage of about 0.12V and a current of ≈40kA. At the beginning of the perturbation the eITB is strong and wide (Fig. 8b), consistent with a reversed shear q-profile resulting from the 50kA off-axis bootstrap current. The ohmic current adds a strongly peaked current density component, which is determined by the profile of T_e. As a consequence, the shear reversal is lost, the eITB gets weaker and shrinks, the bootstrap current (I_{BS}) decreases and the confinement degrades. This can be regarded as the first clear demonstration of the direct dependence of confinement on the current sources, since for this perturbation the additional power input is negligible.

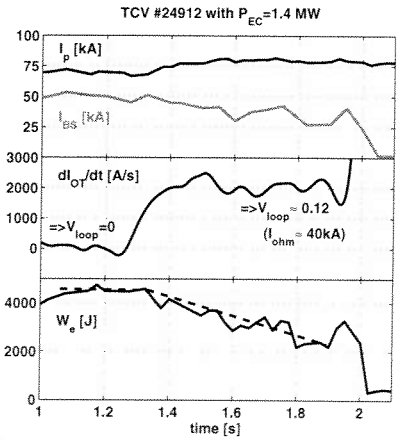

Fig. 8a
Inductive current perturbation causes confinement degradation

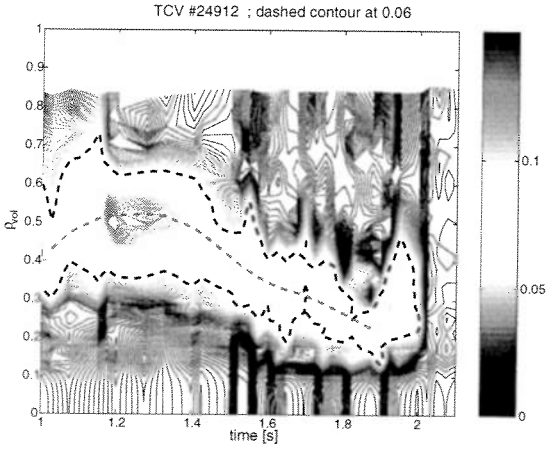

Fig. 8b
Contour plot of ρ^*_T showing degradation of the ITB

[1] G. Tresset et al. Nucl.Fusion, 42, 520 (2002)
[2] O. Sauter et al. Proc. 29th EPS Conf. on Plasma Physics and Contr. Fusion, Montreux, 2002, P2.087
[3] P. Nikkola et al. Nucl.Fusion, submitted for publication (2003)
[4] M.Henderson et al. Phys. Plasmas, 10(5), 1796 (2002)

This work was partly supported by the Swiss National Science Foundation

Dynamical Studies of Suprathermal Electron Relaxation by Modulated ECCD

S. Coda, S. Alberti, P. Blanchard[1], I. Klimanov, J.-M. Moret, P. Weber

Centre de Recherches en Physique des Plasmas
Association EURATOM-Confédération Suisse
Ecole Polytechnique Fédérale de Lausanne, CRPP - EPFL, CH-1015 Lausanne, Switzerland

1. Introduction

The relaxation phenomena governing the behaviour of suprathermal electrons largely determine the physics of electron cyclotron current drive (ECCD). Experimental and modeling work performed on TCV in recent years [1,2] has shown that both rf and collisional diffusion in velocity space and cross-field transport in physical space operate on comparable time scales, and that the latter in particular plays a key role in regulating the current profile and, at the high power levels of TCV, the current drive efficiency as well. Recent perturbative studies of the response of high field side (HFS) electron cyclotron emission (ECE) to short, low duty cycle, periodic, localised ECCD pulses have yielded promising initial quantitative results on the relaxation dynamics, which are discussed in this paper.

The TCV tokamak (R=0.88 cm, a=0.25 cm, I_p<1 MA, B_T<1.54 T) is equipped with a 4.5 MW, second and third harmonic EC heating system that includes 7 separate launchers, whose injection angles are adjustable in real time [3]. A second harmonic X-mode ECE radiometer, operating in the 78-114 GHz range with 24 channels of 0.75 GHz bandwidth [4], was employed in this study on either of two horizontal viewlines on the HFS [1].

2. Methodology

The ECCD pulses are applied with one or two 0.45 MW sources (with identical aiming) and are defined by a 0.2 ms ramp-up, a 0.25 ms flat top and a 0.1 ms ramp-down, with a periodicity of 8 to 10 ms. The pulse length has been empirically adjusted to be well below the time for quasilinear saturation and to permit observation of the spatial propagation of the pulse after turn-off. Coherent averaging of the ECE signals is performed throughout the steady-state phase of the discharge, comprising up to 200 pulses. This permits the pulse to be detected with good signal-to-noise ratio on all channels in spite of a modest average power (< 40 kW). The sensitivity of the measurement during the decay phase is primarily limited by the residual sawtooth oscillations, statistically attenuated by averaging. The suprathermal origin of the signal is confirmed by a direct comparison with the signal detected by a new 65-100 GHz radiometer placed symmetrically on the low field side (LFS): the two are in excellent agreement before the pulse, whereas the HFS radiative temperature increase during the pulse is over 5 times larger than its LFS counterpart at all locations.

---

1. Current address: DRFC, CEA/Cadarache, 13108 Saint Paul-lez-Durance Cédex, France

To quantify the suprathermal population, we postulate a bi-Maxwellian energy distribution, with a characteristic temperature T_s and density n_s. We further assume, for this initial analysis, that T_s is independent of position. The suprathermal emission is relativistically downshifted by $\delta f/f \sim -7/4\ T_s/(m_e c^2)$ [5]. This downshift can be estimated in many cases by associating the frequency of the symmetry point in the signal distribution with the point of smallest minor radius along the chord. The characteristic energy can also be independently estimated by equating the pulse decay time with the collisional slowing-down time. The two calculations are found to be in good agreement. Once an approximate value for T_s is thus obtained, the optical thickness τ_s of the suprathermal component can be derived from the expression [4] $T_{rad}=T_{rad,b}\ \exp(-\tau_s) + T_s\ [1-\exp(-\tau_s)]$, where T_{rad} denotes the measured radiative temperature on the HFS and $T_{rad,b}$ the radiative temperature of the bulk. Finally, for a sufficiently narrow emissivity shape function, the suprathermal density can be extracted through the formula [5] $\tau_s=3.71\ n_s T_s R/B$ [10^{19} m^{-3}, keV, m, T], where R and B are the major radius and magnetic field, respectively, at the emissivity peak location. In this entire study $\tau_s<1$, i.e. the suprathermal population is found to be optically thin, a consequence of the low average applied power.

3. Results

The time history for the reference case is shown in Fig. 1. Here, the plasma was centred in the vacuum vessel and heated centrally by one source from the LFS on the midplane, with the ECE viewline also on the midplane. The outward propagation of the pulse is clearly visible. A temperature $T_s \sim 11.5$ keV is inferred from the signal distribution, consistent with decay times of the order of 0.2-0.3 ms.

A simple measure of the radial propagation of the pulse is the time to peak (calculated from the power turn-off time), which is plotted in Fig. 2 for four different shots with increasing vertical distance between the magnetic axis and the ECE chord, and the microwave beam(s) always trained on the former. The abscissa for each shot is the emission location of downshifted radiation at $T_s=11.5$ keV. The overlapping data are in satisfactory agreement, with most of the scatter attributed to density variations. The ray tracing code TORAY-GA [6] places the EC deposition in the region $\rho=0$-0.2, which is confirmed by the measurements to be a region of zero delay, within the ECE time resolution of 0.05 ms.

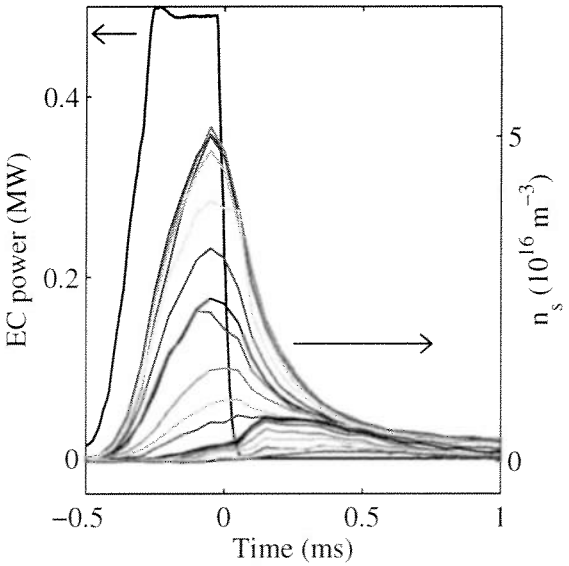

Fig. 1 Suprathermal density derived from the HFS ECE signals, in response to a short central ECCD pulse with a toroidal injection angle of 25° (ending at t=0), averaged over 114 coherent pulses (shot 25018, current I_p = 230 kA, line-averaged density $\bar{n}_e$ = 1.5x10^{19} m^{-3}, peak temperature T_b = 1.5 keV, edge elongation κ = 1.6).

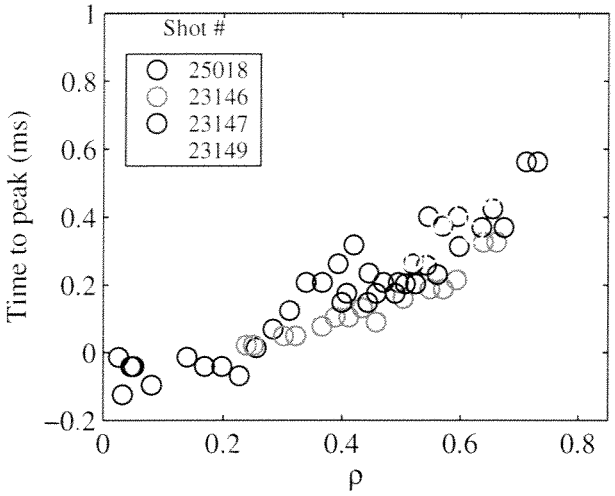

Fig. 2 Time lag from the end of a central ECCD pulse to the ECE peak, as a function of ρ *(normalised radial coordinate proportional to the square root of the plasma volume), calculated by taking into account the estimated relativistic downshift, for four different shots (I_p = 230 kA, $\bar{n}_e$ = 1.5-2.1x10^{19} m^{-3}, T_b = 1.5 keV, κ = 1.6, power = 0.45-0.9 MW)*

The effect of radial transport on the shape of the suprathermal profile is rendered readily apparent by plotting successive snapshots of the normalised n_s profile after t=0, as shown in Fig. 3 for a centrally heated and an off-axis heated case. In both discharges a substantial broadening of the profile around the deposition region is clearly observed. It is also apparent that the dynamics are rather complex and strongly space dependent, and would be difficult to describe, for instance, with a simple, purely diffusive model.

Part of the observed complexity may also be due to changes in the velocity distribution function over space and time, which even within the assumptions of our simple model could be described by a non-uniform T_s profile with resulting changes in both the calculated n_s and the emission position of each channel. Ultimately, energy and position cannot be uniquely separated in the ECE signals without relying on constraints from models. However, it is preferable to proceed initially through model-independent analysis techniques in order to generate parameters that can eventually be employed in an objective evaluation of the goodness of different models.

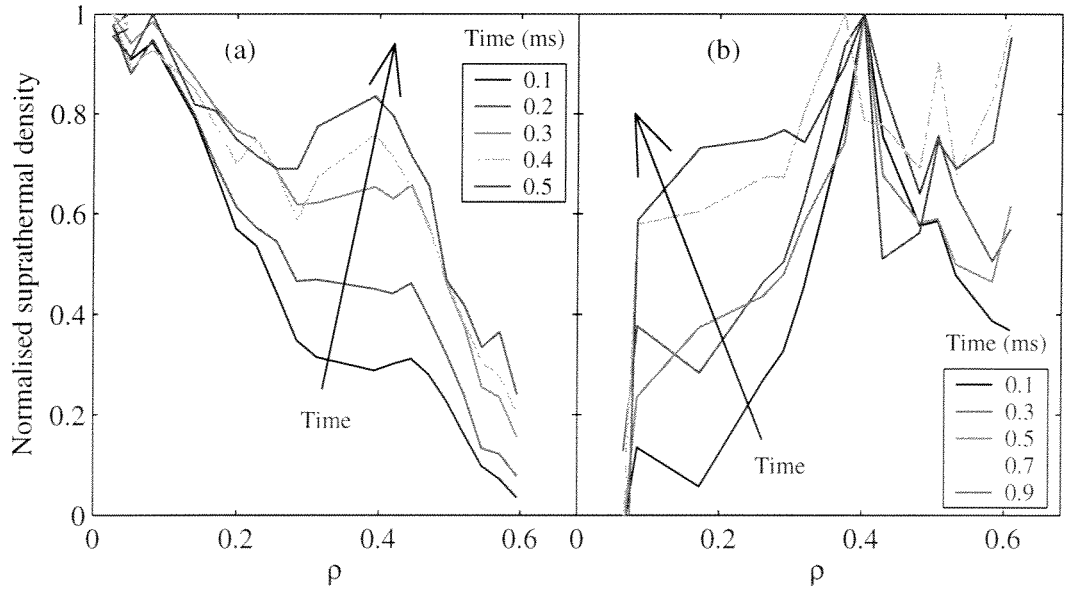

Fig. 3 Successive snapshots of normalised suprathermal density after ECCD turn-off: (a) shot 25018 (central deposition), (b) shot 23556 (deposition at ρ*~0.45). The plasma and EC parameters are similar (cf. Fig. 1).*

A particularly satisfying approach is the determination of the transfer function of the system, in an eigenmode representation, by means of a formal system identification method [7]. We have performed a preliminary analysis of the discharges in this study, which include several parameter scans outside the scope of this paper, by assuming common poles for all ECE channels. Generally, a calculation with two or three poles yields optimal results, with no further improvement in the normalised loss function beyond a maximum of three. Results for two discharges are shown in Fig. 4. The eigenmodes are normalised such that their sum (also shown) represents an estimation of the source function. Figure 4(a) refers to the reference shot 25018; the case of Fig. 4(b) is identical except for the presence of 0.45 MW cw central preheating, with a resulting estimated T_s~20 keV. In the latter discharge the source function is anomalously broad (an effect visible directly in the raw data).

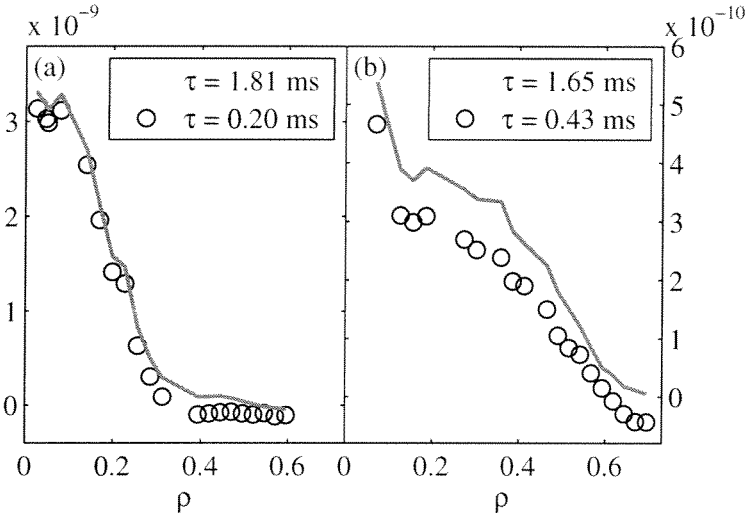

Fig. 4 Two-pole eigenmodes (circles) of the system transfer function (EC power to suprathermal density) and corresponding source functions (solid lines), for (a) shot 25018 (cf. Fig. 1), (b) shot 25032 (similar except for 0.45 MW cw central EC power, T_h~ 2 keV). The time constant τ is given for each eigenmode.

These results amply illustrate the potential of this technique in determining the suprathermal electron source function and the characteristic time constants of the relevant dynamical processes. The next stage of this analysis will be the application of specific transport models to these eigenmode sets.

Acknowledgment

This work was supported in part by the Swiss National Science Foundation.

References

[1] S. Coda et al., Proc. 19th Int. Conf. on Fusion Energy, Lyon, 2002, EX/W-5 (IAEA, to be published); S. Coda et al., submitted to Nucl. Fusion (2002).
[2] P. Nikkola et al., submitted to Nucl. Fusion (2002).
[3] T.P. Goodman et al., Proc. 19th Conf. on Fusion Energy, Lyon, 2002, OV/4.2 (IAEA, to be published).
[4] P. Blanchard et al., Plasma Phys. Control. Fusion **44** (2002) 2231.
[5] M. Bornatici et al., Nucl. Fusion **23** (1981) 1127.
[6] K. Matsuda, IEEE Trans. Plasma Sci. **17** (1989) 6.
[7] J.-M. Moret and Equipe Tore Supra, Nucl. Fusion **32** (1992) 1241.

Magnetic Triggering of ELMs in TCV

A W Degeling[1], Y R Martin[1], J B Lister[1], L Villard[1],
V N Dokouka[2], R R Khayrutdinov[2] and V E Lukash[3]

[1]*Centre de Recherches en Physique des Plasmas, Ecole Polytechnique Fédérale de Lausanne, Association EURATOM-Confédération Suisse, 1015 Lausanne, Switzerland*
[2]*TRINITI, Troitsk, Moscow Region Russia.*
[3]*RRC Kurchatov Institute, Moscow, Russia*

1. Introduction

While the beneficial properties of Edge Localised Modes (ELMs) have resulted in the adoption of the ELMy H-mode as the standard operating scenario for ITER, ELMs in ITER have the serious drawback that they will cause unacceptable heat loads to plasma facing components. Since the energy released per ELM is found to scale with the time delay between ELMs, a possible solution to this problem could be to control the ELM frequency f_{elm}, in order to avoid ELMs with large amplitudes. This paper reports attempts made on TCV to control the ELM frequency, using a magnetic trigger signal provided by sets of poloidal field coils situated either inside or outside the vacuum vessel.

2. Internal and External Coil Excitation

In these experiments, voltage perturbations are applied to either the internal or inboard side external poloidal magnetic field coils (G-coils or E-coils respectively) during single null ELMy H-mode discharges with stationary conditions. The G-coils are located at the top and bottom of TCV within the vacuum vessel and are routinely used for rapid response feedback vertical stabilisation of the plasma. The perturbation signal to the G-coils was added to the vertical stabilisation feedback loop and consisted of a series of square pulses of 1ms duration, with a variable delay between pulses. This produced spike - like pulses in the current to the G-coil (up to 2kA) that resulted in deviations in the plasma vertical position of up to 5 mm. The input signal was produced by an arbitrary waveform generator, and could be tailored to increase the coupling efficiency with the ELM dynamics. Figure 1 shows an example of G-coil excitation during a SNL ELMy H-mode in which the perturbation consisted of three 200 ms long bursts of negative top-hat pulses at 200Hz, separated by 100 ms off periods. During the first burst period, a denisty - gas control feedback oscillation prevented stationary ELMy H-mode operation, resulting in an ELM-free phase for 50 ms. With this exception, f_{elm} remains locked to the driver signal for most of the first, second and half of the third bursts. During the second burst, three breakages in synchronisation occur, and halfway through the third burst synchronisation is lost and not recovered. Inbetween the bursts, f_{elm} relaxes to a value as low as half that of drive signal.

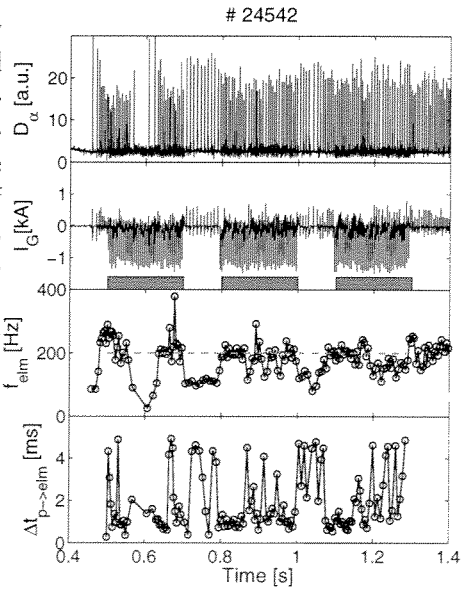

Figure 1: a) D_α signal; b) G-coil current; c) f_{elm} (blue) and f_D (red); d) Delay between each ELM and the previous pulse.

The E-coils are a linear array of eight coils located along the central column of the ohmic field transformer coil, exterior to the vacuum vessel, and are routinely

used for position and shape control. Only E-coils 5 and 6, which straddle the veritcal position of the magnetic axis in the SNL discharges used in this experiment, were used. The input pulse train signal in this case was added to the programmed reference signals for each coil. The maximum sampling rate for programmed signals in the plasma control system is 1kHz, and two samples were used for the up and down phases of each pulse. This, and the field penetration time through the vacuum vessel limited the bandwidth of perturbations that could be excited using the E-coils to less than 167 Hz. Figure 2 shows an example in which the drive frequency was scanned from 167 to 83 Hz. Again a density gas feedback control oscillation caused ELM-free phases during the early part of the discharge. As stationary conditions developed, a correlation between f_{elm} and f_D becomes visible, with f_{elm} oscillating between the fundamental and first harmonic of f_D, before settling on the harmonic after about 1 second.

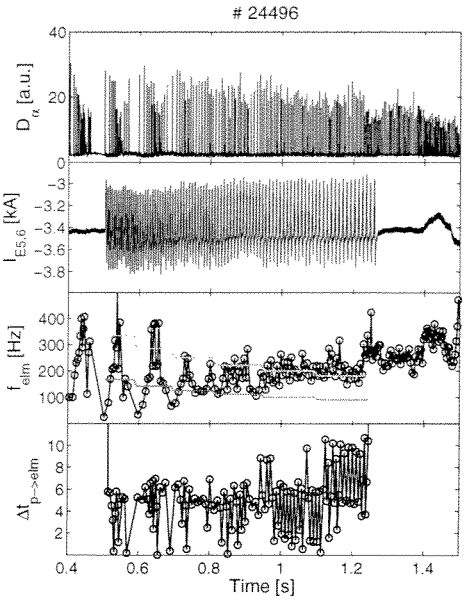

Figure 2: a) D_α signal; b) E-coil current; c) f_{elm} (blue), f_D (red) and $2f_D$ (green); d) Delay between each ELM and the previous pulse.

3. The Triggering Mechanism

The perturbations used in these experiments were designed to cause rapid deviations in the plasma vertical position which, due to the up-down asymmetry of the vacuum field for the single null configurations used, would result in purturbations of the edge current density J_{edge}. In so doing, the perturbations were aimed at activily triggering ELM events by destabilising current driven modes close to the plasma edge, which are currently thought responsible for ELMs. It may also be expected that the changing coil currents will affect J_{edge} by modulating the surface loop voltage. Figure 3 shows a comparison of the perturbed parameters and ELM occurrence probabilities for three discharges perturbed by G-coil excitations that showed significant coupling to the driver signal. Each parameter is phase coherently averaged with respect to the perturbation onset times. The ELM occurrences from -2 to +4 ms with respect to the perturbation onset times were histogrammed to estimate the probability of an ELM occurring P_{elm} during this time window. Discharges #20333 and #20334 are SNL configuration, while discharge #22768 is SNU configuration, as indicated in the figure. In each discharge, the input perturbation signal was a symmetric square pulse, with the polarity of the pulse reversed for discharge #20334. Note that for the two SNL discharges, the peak in P_{elm} corresponds to the upward movement of the plasma, whereas for the SNU discharge it corrresponds with the downward movement of the plasma, and that the peak in P_{elm} in #20333 occurs well after the input voltage pulse has passed. This figure indicates that ELMs correlated with the driver signal are most probable when the plasma moves in a direction away from the active X-point. It can be argued simply that this direction will cause a positive excursion in J_{edge}. The DINA code, a free boundary equilibrium solver that includes the trans-

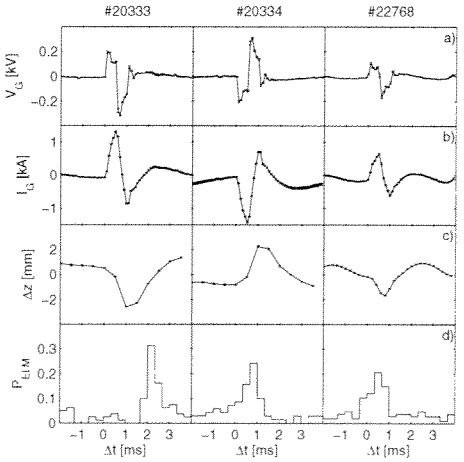

Figure 3: Boxcar averaged signals w.r.t perturbation times for 3 discharges a) Input V(t); b) G-coil current; c) Perturbed vertical position. d) Histogram of ELM occurrences.

port of poloidal flux and thermal energy under the assumption of instantaneous force balance [2], was used to estimate the size and timing of the perturbation in J_{edge}, for these three discharges. DINA was previously equiped to model the full TCV plasma control system, including all poloidal field coils, power supplies and diagnostics. A high radial resolution was used to observe the effect of an inward diffusing current perturbation in response to multiple pulses, and the results were coherently averaged to produce figure 4. This figure shows that sense of the perturbed J_{edge} is as expected, and that variations in J_{edge} in response to vertical displacements is about 10% of the unperturbed value.

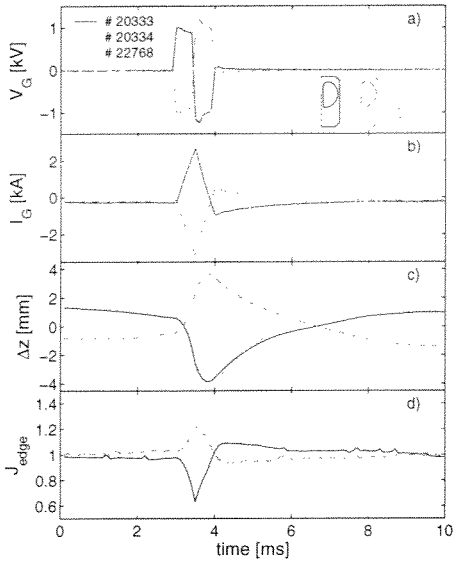

Figure 4: DINA results for 3 discharges. a) Input V(t); b) G-coil current; c) Perturbed vertical position; d) Edge current density.

4. An Illustrative Model

There are a number of interesting features of the driven dynamical system that may provide some insight to what type of dynamical models can adequately describe ELMs. One such feature is the set of three momentary losses in frequency tracking seen in figure 1, during the second 200 ms burst. Such events have been found to occur repeatedly in particular cases, for example #20333 shown in the top row of Figure 6, in which the frequency tracking was otherwise particularly strong. It is interesting to consider whether a simple model of the ELM cycle can produce such behaviour under the action of a driver. To this end we consider a simple way in which J_{edge} and pressure gradient p′at the H-mode pedestal may be dynamically linked and include an abrupt drop in p′ when a boundary in (p',J) space is exceeded. If only a small layer of fixed width Δx is considered then p′ is given by p/Δx, and the model equation for p is:

$$\frac{dp}{dt} = Q_{in}(1+\sigma\varepsilon(t)) - W(p,J)p$$

where Q_{in} represents the net power flux through at the plasma edge, the term in brackets represents fluctuations in power flux (described by ε(t)) of amplitude σ, and Wp describes the loss in p due to an ELM. W is given by:

$$W(p,J) = (J - J_{crit}(p))/\tau_{mhd}$$

for $J > J_{crit}$ and 0 otherwise, where τ_{mhd} is an ideal growth rate and J_{crit} parameterises the marginal stability boundary, which is chosen to be a parabolic function resembling that proposed by detailed MHD instability analysis [3]. The equation for J is:

$$\frac{dJ}{dt} = (J_{SS}(p) + J_{ext}(t) - J)/\tau_R$$

where J_{SS} is the steady state current (ohmic +bootstrap $\propto$ p′), J_{ext} is the externally driven current perturbation and τ_R is a resistive timescale for current redistribution. Figure 5 shows the limit cycle trajectory repre-

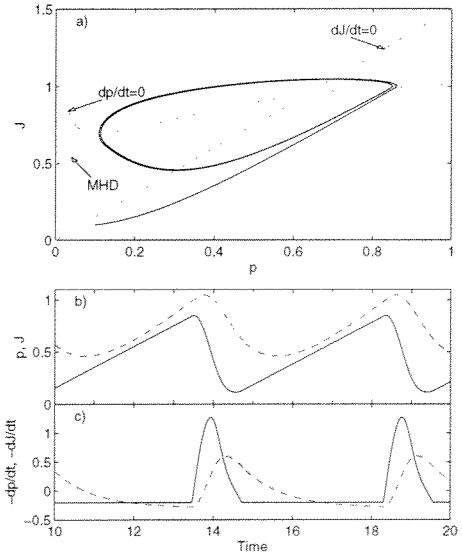

Figure 5: a) Phase space trajectory of J and P showing the model ELM limit cycle; b) Time variation of J and P; c) Time variation of -dJ dt and -dp dt (τ_R 1, τ_{mhd} 0.01, Q_{in} 0.2).

senting the unperturbed ELM cycle, the curves for J_{crit}, dp/dt = 0 and dJ/dt = 0, and also the timeseries for J, p, -dJ/dt and -dp/dt. An external sinusoidal perturbation J_{ext} was added to J, and the frequency was ramped smoothly as in discharge #20333. Rows 2 to 4 of Figure 6 show the model f_{elm} and ELM phase with respect to the driver for three cases in which the fluctuation level was increased. For $\sigma = 0$, the model f_{elm} tracks f_D everywhere except the high and low frequency ends of the f_D sweep, where regular oscillatory excursions in f_{elm} occur. This behaviour is characteristic of a phenomenon known as "periodic pulling" [4] found in dynamical systems analogous to the driven van der Pol oscillator. As σ is increased, these excursions in f_{elm} begin to resemble those seen in #20333, suggesting that periodic pulling may be the root cause of these excursions in the experiment. That said, it is known that ELM dynamics are also very often coupled to the sawtooth frequency f_{st} in TCV [5]. The top plot in Figure 7 shows that this is indeed the case in discharge #24542 (shown in Figure 1) when the driver is off, and that the driver unfortunately corresponds with roughly twice f_{st}. It is interesting that abrupt excursions in f_{elm} from f_D appear to occur as twice f_{st} drifts away from f_D. An attempt to include the coupling effect of sawtooth heat pulses arriving at the plasma edge was made by adding a sinusoidal oscillation to Q_{in}. The lower plot in figure 7 shows an example in which Q_{in} was modulated by 40%, and J was strongly driven at close to twice f_{st}. The two perturbations are offset in time to allow the effect of each one separately as well as their combination to be seen. This plot shows that perturbations in Q_{in} can cause interruptions in the synchronisation to the driver. The competitive effect of sawtooth heat pulses in ELM magnetic triggering experiments is a subject of further study in TCV.

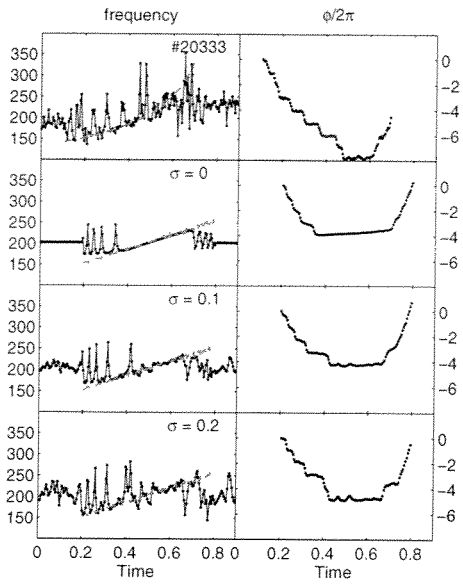

Figure 6: left: f_{elm} (blue) and f_D vs. time; right: unwrapped ELM phase w.r.t driver. a) Experiment discharge #20333; b - d) Model timeseries with increasing fluctuation level σ (τ_R 1, τ_{mhd} 0.01, Q_{in} 0.2, J_{ext} 0.2

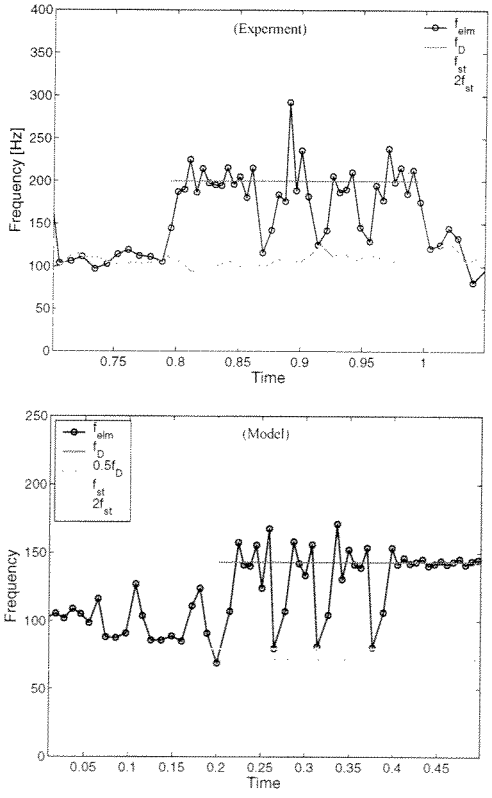

Figure 7: Top: Detail of discharge #24542 showing f_{elm}, f_D, f_{st} and $2f_{st}$. Bottom: Model result with driver and modulated Q_{in} (τ_R 1, τ_{mhd} 0.01, Q_{in} 0.2σ 0.1, J_{ext} 0.9, Q_{st} 0.4).

Bibliography

[1]A W Degeling *et al, Appearing in Plasma Phys. Contol. Fusion*

[2] R R Khayrutdinov *et al Plasma Phys. Contol. Fusion* **43** (2001), 321

[3]J W Conner *et al, Phys. Plasmas* **5** (1998) 2687

[4] T Klinger *et al, Phys. Rev. E.* **52** (1995) 4316

[5] Y R Martin *et al Plasma Phys. Contol. Fusion* **44** (2002), A373

The authors would like to thank the TCV team without whom these results would not be analysable. This work was partly supported by the fonds National Suisse de la Recherche Scientifique.

Improving Tokamak Vertical Position Control in the Presence of Power Supply Voltage Saturation

J-Y. Favez[1,2], J.B. Lister[1], Ph. Müllhaupt[2], B. Srinivasan[2], F. Villone[3]

[1]*Centre de Recherches en Physique des Plasmas, Association EURATOM-Confédération Suisse, EPFL, 1015 Lausanne, Switzerland*
[2]*Laboratoire d'Automatique, EPFL, 1015 Lausanne, Switzerland*
[3]*Associazione EURATOM/ENEA/CREATE, DAEIMI, Univ. di Cassino, Italy*

Introduction The control of the current, position and shape of a tokamak plasma is complicated by the instability of the vertical position when the plasma cross section is elongated. Linearised models of the system to be controlled all share the feature of a single unstable pole, attributable to this vertical instability, and a large number of stable or marginally stable poles (attributable to zero or positive resistances in all other circuit equations). The presence of only a single unstable pole is due to the system being stable before the vertical plasma movement is included. Due to the cost of ITER, there are relatively low voltage margins in the Poloidal Field coil power supplies, suggesting that the feedback control loop may experience actuator saturation during occasional large transients. We present a modified feedback controller which explicitly takes into consideration the saturation of the power supply voltages when generating the power supply demand signals. This novel approach has been tested on simulations using ITER and JET linearised plasma equilibrium response models.

Development of the control method Our aim is to take an existing controller design, the reference controller, and to enlarge its region of attraction **A** (the region in state space from which the closed loop system asymptotically reaches the origin [1,3]) to the null controllable region **C** (the region in state space where there exists an open loop input that can steer the system to the origin [1,3,4]). In previous work described in detail in [2] we formally considered a system with a single unstable pole and a single stable pole. We derived the region of attraction of the closed loop system with saturation of the single input and we examined the performance of the controller.

Throughout this work, we use linearised tokamak models (CREATE-L for JET [5] and ITER [6]). which describe the tokamak by ODEs in the continuous time state space format given by

$$\begin{aligned} \dot{x}_p &= A_p x_p + B_p u + E_p \dot{w} \\ y &= C_p x_p + F_p w \end{aligned} \qquad (1)$$

. The state variables x_p explicitly represent the physical active coil currents, the passive structure currents and some plasma variables when the model is created. The coil voltages are the vector u. The outputs of the system, the vertical and radial plasma positions, wall-separatrix gaps, plasma current and all the magnetic diagnostics measurements, are given by the variable y. The input $w = [\Delta\beta\ \Delta l_i]^T$ represents disturbances such as ELMs or sawteeth.

Traditionally, we talk of the vertical position as being unstable. However, when the position is unstable, the passive currents, coil currents and position also grow exponentially, although all these physical variables cannot be considered to be separately unstable. The eigenvalues of the matrix A_p in (1) determine the dynamical evolution of the physical variables x_p. One of the eigenvalues of A_p is positive when the vertical field index is curved outwards. However, A_p is not diagonal and therefore the variables x_p are not the eigenvectors of the system. We transform these equations from the variables x_p to new combinations x for

which the transformed matrix A is diagonal, generating the new equations:

$$\dot{x} = Ax + Bu + E\dot{w}; \qquad x_p = Tx; A = T^{-1}A_pT; B = T^{-1}B_p; E = T^{-1}E_p$$
$$y = Cx + Fw; \qquad C = C_pT; F = F_p \qquad (2).$$

One of the new orthogonal states is unstable and this is now the unstable state. Unfortunately, there is no intuitive combination of the physically meaningful variables x_p which describes the unstable state, even for the simplest 3-circuit model. If we can stabilise the unstable state, all other states, being stable, will decay and the closed loop system is stable. Provided there are enough diagnostic measurements, the unstable and stable states can be estimated using the pseudo-inverse of C, by $\left[\hat{x}, \hat{w}\right] = \left[C, F\right]^{+} \cdot y$, reconstructing the unstable state, the stable states, and the disturbance w. If we neglect F (the direct influence on y of $[\Delta\beta\ \Delta l_i]^T$ with respect to the nominal equilibrium) then $\hat{x}$ is simple to generate. However, coil saturation is most likely during a large perturbation and the influence of F must be included, the object of future work.

Consider system (2) with zero disturbance input. We can split this system into an anti-stable and a stable subsystem [4] $\begin{bmatrix} \dot{x}_1 \\ \dot{x}_s \end{bmatrix} = \begin{bmatrix} \lambda_1 & 0 \\ 0 & A_s \end{bmatrix} \begin{bmatrix} x_1 \\ x_s \end{bmatrix} + \begin{bmatrix} \lambda_1 \\ b_s \end{bmatrix} u$ (3). Here x_1 describes the anti-stable subsystem and $x_s = [x_2\ x_3\ \ldots\ x_n]^T$, A_s and b_s describe the stable subsystem. The null controllable region is only restricted by the unstable state (anti-stable system) while the stable states (stable subsystem) can be controlled for any arbitrary values. We assume that there exists an adequate algebraic state reconstruction available such that $\hat{x} \sim x$ (in what follows we use these interchangeably). We can therefore replace our reference input-output controller controller $v(s) = K(s)y(s)$ by a linear state feedback controller

$$v(x) = fx = f_1x_1 + f_2x_2 + f_3x_3 + \ldots + f_nx_n \qquad (4)$$

With this feedback controller the closed loop system becomes $\dot{x} = Ax + B\,sat(fx)$. By considering the linear controller (4) we can see that **A** = **C**, if and only if $f_2 = f_3 = \ldots = f_n = 0$ and if the linear stability condition $1 + f_1 < 0$ is satisfied. For all other linear controllers in which at least one of the parameters $f_2 f_3 \ldots f_n$ is nonzero, **A** $\subset$ **C**.

We have been able to enlarge the region of attraction to include the full null controllable region **A** = **C**, without loss of local performance, by introducing a continuous nonlinear function in the controller [2]. Consider the modified controller $v(x) = f_1x_1 + k(x)(f_2x_2 + f_3x_3 + \ldots + f_nx_n)$; $u = \text{sat}(v)$ (5). Assume that f has been chosen to obtain the desired performance of the closed-loop system near the origin, for small disturbances. Compared to (4), the new controller differs by the introduction of a smooth nonlinearity by choosing $k(x) = (1 - x_1^2)$ where $0 < k(x) \leq 1$ since $|x_1| < 1$ within the null controllable region. $k(x) = 0$ for $|x_1| > 1$. The idea behind this nonlinear controller is as follows. If $x_1 \approx 0$, then $k(x) \approx 1$ which implies that the controller is approximately the linear state feedback controller $v \approx fx$. In this case, the controller concentrates on local performance. On the other hand, if the unstable state approaches the boundary of the null controllable region **C**, $x_1 \approx \pm 1$ and $k(x) \approx 0$. This implies that the controller is approximately the linear state feedback $v \approx f_1x_1$, and it focuses on the stabilisation of the unstable state and global stability (**A** = **C**). Moreover, since this controller is a continous one, chattering is avoided.

Testing the method on ITER We first implemented this approach on a closed loop model of ITER. The state was not estimated, but taken directly from the equations. We compare via simulation the reference controller [7], given by $v = fx$, against the new continuous nonlinear controller (5) using phase diagrams. Since we are dealing with a high order system (50 .. 100 states) we cannot show the evolution of all states. Thus, the phase diagrams show the evolution of only two states: the unstable state x_1, and one of the most disturbed stable states,

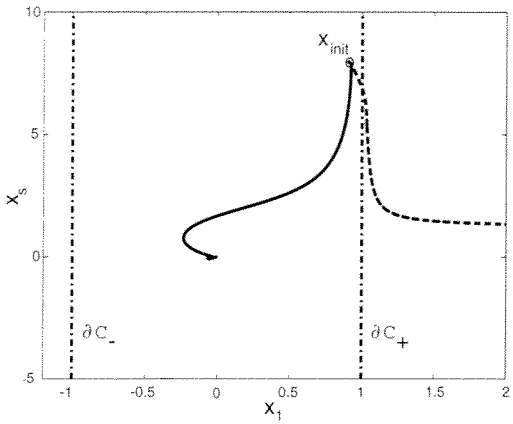

Fig.1: Case of non-zero initial conditions (x_{init}); dashed: reference controller, solid: continuous nonlinear controller.

conditions. The phase diagram (Fig.1) shows the initial conditions point x_{init}, located inside the null controllable region. Since for the nonlinear controller the initial conditions are located in the region of attraction, the trajectory converges to the origin. For the reference controller the trajectory diverges, thus confirming by simulation that $\mathbf{A}_n \subset \mathbf{C}$.

The second case shows the evolution of the trajectories for both controllers during and after a large perturbation (Fig.2). At t_2 the states of the systems with both controllers are inside **C**. Since for the nonlinear controller $\mathbf{A}_c = \mathbf{C}$, the trajectory converges to the origin. For the reference controller the trajectory diverges and thus, the state is not in $\mathbf{A}_n$.

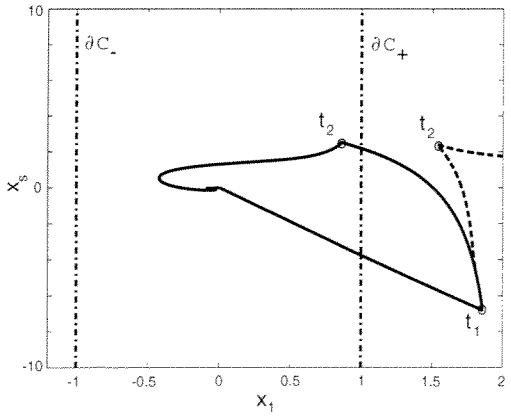

Fig.3: Case of a very large perturbation; dashed: reference controller, solid: continuous nonlinear controller.

denoted in the figures by x_s. In what follows, the region of attraction of the reference controller is denoted by $\mathbf{A}_n$ and the region of attraction of the continuous nonlinear controller is denoted by $\mathbf{A}_c$. To disturb the system away from the equilibrium we apply an ELM-like perturbation. The perturbation starts at t_0, reaches its maximum at t_1 and vanishes at t_2. Since it is difficult to know whether the state remains in the region of attraction during the perturbation, we have to wait until the perturbation vanishes at t_2 to determine if the controller was able to stabilise the system.

For the first case we do not disturb the system, but we set non-zero initial

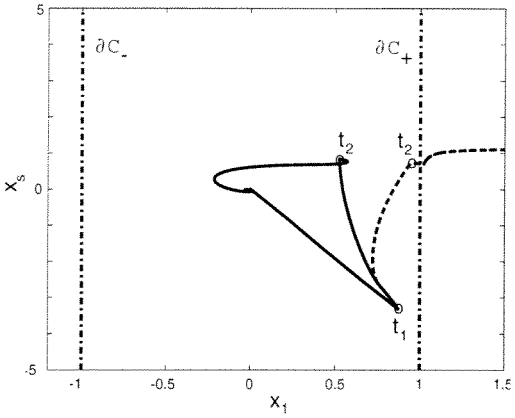

Fig.2: Case of a large perturbation; dashed: reference controller, solid: continuous nonlinear controller.

The third case shows the trajectory for a much larger perturbation amplitude (Fig.3). Both trajectories leave the null controllable region **C** and only the trajectory for the system with the nonlinear controller reenters **C**. For all these cases, the unstable state x_1 is brought back to the origin faster when the continuous nonlinear controller is used. This is the benefit of the nonlinear function $k(x)$ which helps the controller concentrate on the unstable state in the proximity of the boundaries of **C** and beyond it.

Testing the method on JET We implemented this technique on the CREATE-L model of JET, including the closed loop controller. We generated an observer of the unstable state $\hat{x}$ directly from the documented diagnostics. We increased the amplitude of the disturbance (ressembling ELMs) until the closed loop model lost control due to saturation of the FRFA supply. The simulation was repeated with the modified controller and control was no longer lost.

Fig.4 shows an example of the evolution of the vertical position z and the FRFA control voltage for a very large ELM perturbation in JET. The ELM perturbation starts at t_0, reaches its maximum at t_1 and vanishes at t_2 (vertical dashed lines). The reference controller loses stability just after t_1.

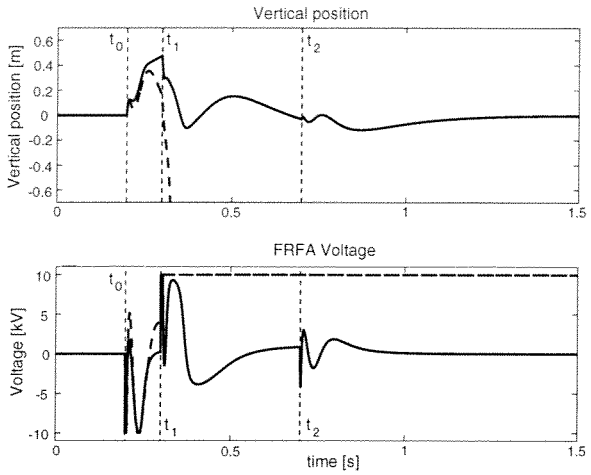

Fig4: Testing the modifed controller (solid) on a JET simulation in which the standard controller (dashed) loses control

Discussion A simple continuous nonlinear controller for the stabilisation of the ITER tokamak unstable vertical position in the presence of voltage saturation is proposed. The principle is to modify an existing linear controller by introducing a simple nonlinear term into the control law. This new controller enlarges the region of attraction to the maximal reachable region of attraction under input saturation, which is the null controllable region. Additionally, its local performance around the origin is similar to that of the existing linear controller. An additional advantage of the nonlinear controller is that the unstable state is brought back faster to the origin and thus, the rejection of the perturbation is more efficient. This is a benefit of the nonlinear function where the controller concentrates on the control of the unstable state in the proximity of the boundaries of null controllable region and beyond it.

Acknowledgements This work was partly supported by the Fonds National Suisse de la Recherche Scientifique. We thank Y. Gribov and A. Kavin for delivering the linearised closed loop model of ITER and R. Albanese, G. Calabrò, M. Mattei and A. Pironti for JET.

References

[1] J. Alvarez, R. Suarez, and J. Alvarez, Planar linear systems with single saturated feedback. System & Control Letters, 20:319-326, 1993.

[2] Favez J.-Y., Mullhaupt Ph., Srinivasan B., Lister J.B., Bonvin D "Improving the region of attraction of ITER in the presence of actuator saturation", Lausanne Report, LRP 754/03

[3] T. Hu and Z. Lin. Control Systems with Actuator Saturation: Analyses and Design. Birkhauser, Boston, 2000.

[4] T. Hu, Z. Lin, and L. Qiu. Stabilization of exponentially unstable linear systems with saturating actuators. IEEE Transactions on Automatic Control, 46(6):973-979, 2001.

[5] R. Albanese, G. Calabrò, M. Mattei, F. Villone, "Plasma response models for current, shape and position control in JET", Proc. SOFT 2002, Helsinki, accepted for publication in Fusion Engineering and Design

[6] A. Kavin, ITER-FEAT linear models description, ITER NAKA JWS,Issue 1, 10 July 2000

[7] M. Ariola, A. Pironti, A. Portone, "A Reduced-Order Controller for Plasma Position and Shape Control in the ITER-FEAT Tokamak", CDC00-REG1452, 3 May 2000

SPBSC-TERPSICHORE BOOTSTRAP CURRENT BENCHMARK FOR THE LOW COLLISIONALITY REGIME

M. Isaev [1], W. A. Cooper [2], K. Y. Watanabe [3], N. Nakajima [3]

[1] *Nuclear Fusion Institute, RRC "Kurchatov Institute", Moscow, Russia*
[2] *Centre de Recherches en Physique des Plasmas, EPFL, Lausanne, Switzerland*
[3] *National Institute for Fusion Science, Toki, Japan*

1. Introduction

The effects of the neoclassical bootstrap current have been investigated for non-axisymmetric systems with different numerical and analytical tools. Fluid moment equations by Shaing et al [1] have been used at the National Institute for Fusion Science (Japan) to explore numerically with the SPBSC code the effects of bootstrap current in Large Helical Device (LHD, NIFS, Japan) plasmas [2].

In contrast to the LHD, the Wendelstein-7X (W7X, Greifswald, FRG) advanced stellarator has been optimised towards small Pfirsh-Schlüter and small bootstrap currents [3]. The bootstrap current for the W7X has been calculated with a numerical drift kinetic solver DKES [4] and with global Monte Carlo simulation [5].

In this paper, we present the comparison between the SPBSC bootstrap current code results and new TERPSICHORE-BOOTSP routine recently developed at the CRPP (Switzerland), [6]. For the sake of simplicity, we take into account only zero radial electric field and for both ions and electrons, the same low collisionality ($1/\nu$) regime, density and temperature profiles. For the benchmarking, we have chosen 3 typical cases corresponding to a symmetrical tokamak case - JT-60 (Section 2), a heliotron/torsatron configuration - the Large Helical Device (Section 3) and an advanced stellarator - Wendelstein-7X case (Section 4) followed by a Summary.

2. Tokamak JT-60

The tokamak JT-60 [7] has major and minor radii 3.4 m and 1 m, central magnetic field 4.2 T and fixed net toroidal current 2.4 MA. The density of ions and electrons with a parabolic profile in the plasma centre was chosen in our calculations to be $0.5\times10^{20}m^{-3}$, the ion and electron temperature profiles to be $10-18s+8s^2$ with a central temperature of 10 keV, where s is a flux surface label. The average value of β equals to 0.0061. The equilibrium has been computed with the VMEC code with 61 radial points, maximal poloidal mode index $m_{pol} = 10$, maximal toroidal mode index $n_{tor} = 8$. The bootstrap current profiles versus s calculated with the SPBSC and TERPSICHORE codes are presented in Fig. 1. A consistent equilibrium solution with bootstrap and diamagnetic currents is obtained after 3 iterations of the SPBSC code, such that the rotational transform value on axis is increased from

1.2 to 2.4. The TERPSICHORE code does not compute the diamagnetic current fraction, but the bootstrap current solution of 385 kA obtained agrees with the value obtained by the SPBSC code after one iteration.

3. Heliotron-torsatron LHD

The calculation of the bootstrap current for the heliotron-torsatron LHD has been performed with the 10-period LHD plasma boundary and parameters used in Fig. 3 (low collision regime is marked with circles) of Ref. [2]. In our SPBSC-TERPSICHORE benchmarking plot - Fig. 2 - the value of β equals to 0.0057, the central temperature of ions and electrons is 8 keV, the central density of ions and electrons is $0.25 \times 10^{20} m^{-3}$. The SPBSC code converged after 5 iterations with 162 Fourier modes for the VMEC equilibrium ($m_{pol} = 10, n_{tor} = 8$) calculation and did not detect any resonance effects. The TERPSICHORE code converged after 6 iterations with 399 Fourier modes for the reconstruction of the equilibrium in Boozer coordinates and detected the small resonance effect near $s = 0.53$.

4. Advanced stellarator Wendelstein-7X

The standard configuration of the advanced stellarator W7X with major radius of 5.5 m and toroidal magnetic field 2.5 T has the rational rotational transform 1.00 near the plasma edge. To avoid the influence of the resonance 1/1 in our benchmarking, we have used a VMEC input file for W7X with a 10% decreased value of the plasma boundary mode (1,1). This leads to a decrease of the edge rotational transform from 1.03 to 0.93. The SPBSC code converged this W7X modified configuration with maximal poloidal and toroidal index $m_{pol} = 5, n_{tor} = 5$ and $m_{pol} = 6, n_{tor} = 6$. However, the SPBSC code did not converge for this modified W7X configuration with maximal poloidal and toroidal mode numbers of $m_{pol} = 7, n_{tor} = 7$ and higher because of the resonance near the rotational transform value 5/6 at $s = 0.70$.

The TERPSICHORE code has a special resonance detuning mechanism to avoid the resonance effects. An artificial positive small term DJP has been added to avoid a vanishing denominator on rational surfaces. The resonance detuning effect with 3 values of the term $DJP = 1.e-09, 1.e-04, 1.e-02$ of the TERPSICHORE-BOOTSP routine for the W7X configuration with $\beta = 0.05$ and 399 Boozer modes in the representation of the magnetic field is presented in Fig. 3. A small value of $DJP = 1.e-09$ leads to visible "jumps" in the bootstrap current profile near the surfaces with rational values of the rotational transform and causes problems in generating a consistent converged solution. The optimal value of the term $DJP = 0.02$ in TERPSICHORE yields a converged solution with 399 Boozer modes. The same result is obtained with the SPBSC code with 72 VMEC and Boozer modes ($m_{pol} = 6, n_{tor} = 6$), $\beta = 0.0095$, see Fig. 4. Slight differences in the bootstrap current profiles computed with the SPBSC and TERPSICHORE codes near $s = 0.5$ can be attributed to the resonance detuning term effects. In the calculation for the W7X configuration, we have used the same temperature and plasma density as for

the previous LHD case.

Summary

We have presented a successful benchmark with the SPBSC and TERPSICHORE-BOOTSP bootstrap current codes in the low β and low collisionality regimes. We have obtained the bootstrap current of 385 kA for the tokamak configuration JT-60, 117 kA for the heliotron/torsatron LHD and 18 kA for the advanced stellarator W7X. The resonance detuning mechanism has been used in the TERPSICHORE code for the W7X configuration with a large number of Fourier modes in the magnetic field representation.

Acknowledgements

The authors are thankful to Dr. S. P. Hirshman for providing us with the VMEC code, to Prof. J. Nührenberg and Dr. M. Mikhailov for valuable discussions. The work was supported by INTAS Grant 99-00592, by Russian - German Agreements WTZ RUS 01-581, by the Russian Foundation of Basic Research, Grant N 03-02-16768, by the Russian Federal Programme on Support of the Leading Scientific School, Grant N 00-15-96526 and by the Fonds National Suisse pour la Recherche Scientifique. A work visit to the National Institute for Fusion Science (NIFS, Japan) of M. Isaev was initiated and supported by the Director of NIFS Prof. M. Fujiwara and Prof. C. Namba (Grant-in-aid from the Ministry of Education, Science, Culture, Sports and Technology, Japan). The work is performed with the support and under the auspices of the NIFS Collaborative Research Programme. The computational results were performed on the NEC-SX5 platforms at the Centro Svizzero di Calcolo Scientifico in Manno, Switzerland and at the National Institute for Fusion Science (NIFS, Japan).

References

[1] K. Shaing, J. Callen, Phys. Fluids **26**, 3315(1983).

[2] K. Y. Watanabe, N. Nakajima et al, Nucl. Fus. **35**, 335(1995).

[3] H. Maassberg, W. Lotz, J. Nührenberg, Phys. Fluids B, **5**, 3728(1993).

[4] S. Hirshman, W.I. van Rij, Phys. Fluids B, **1**, (1989), p.563.

[5] W. Lotz, J.Nührenberg, Phys. Fluids **31**, 2984(1988).

[6] W. A. Cooper et al, Plasma Phys. and Contr. Fus., **44**, 1(2002).

[7] M. Kikuchi, M. Azumi, et al, Nucl. Fusion, **30**, 343(1990).

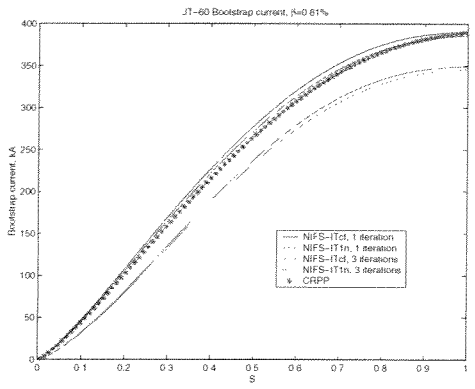

Fig. 1. JT-60 bootstrap current profiles with SPBSC (solid lines, low collision and connection formula regimes) and TERPSICHORE (stars) codes.

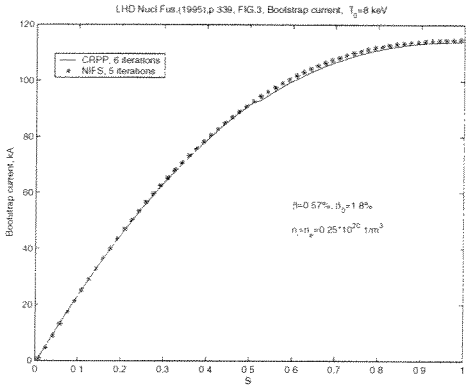

Fig. 2. LHD bootstrap current profiles with SPBSC (stars) and TERPSICHORE (solid line) codes

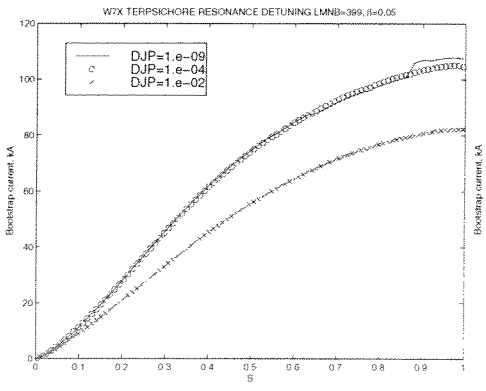

Fig. 3 W7X bootstrap current profiles with the TERPSICHORE resonance detuning. $\beta = 0.05$, 399 Boozer modes, $DJP = 1.e-09$ (solid line), $DJP = 1.e-04$ (circles), $DJP = 1.e-02$ (crosses).

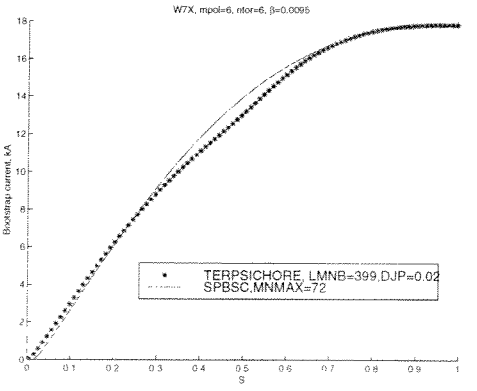

Fig. 4. W7X bootstrap current profiles with SPBSC, 72 Boozer modes (solid line) and TERPSICHORE (stars) codes, 399 Boozer modes, $\beta = 0.0095$

Observation of Suprathermal Ions in the TCV during ECH and ECCD

A.N.Karpushov, S.Coda, B.P.Duval

Centre de Recherches en Physique des Plasmas.
Association EURATOM-Confédération Suisse. EPFL, 1015 Lausanne, Switzerland

Introduction. This paper presents experimental observations of a suprathermal ion population in TCV [1,2], where the ion energy distribution was studied with a Neutral Particle Analyzer (NPA) [3]. The flexibility of the TCV ECH system permitted an investigation of the dependence of the properties of the hot ion distribution on the plasma and ECH parameters. The production of suprathermal ions during ECH and ECCD has been observed on several toroidal plasma machines: the Versator II [4], FT-1 [5], TCA [6] Tokamaks and the W7-A Stellarator [7]. This phenomenon was attributed [8] to a nonlinear three-wave coupling process.

1. Experimental setup. These experiments on the TCV Tokamak (R=0.88 m, a=0.25 m, $I_p < 1$ MA, $B_T < 1.54$ T) employed the X2 (82.7 GHz) EC system, with a total delivered power of up to 2.4 MW in X-mode, for a wide variety of plasma shapes and a broad range of heating locations. The central electron density was $1\text{-}2\times10^{19}$ m^{-3}, the electron temperature reached 7 keV at full X2 EC power, the plasma elongation was 1.15-1.6 and the triangularity –0.3-+0.3. Modulation of the EC power was used to study the dynamics of the fast particle population (Fig.1).

A 5-channel Neutral Particle Analyzer [9] with electrostatic discrimination on TCV views the plasma centre along a vertical chord. The NPA voltage sweeps the energy channels to measure neutral particle energies in the energy range of (0.6→6.5 keV), with a time resolution of 13 ms. A 14 vertical channel FIR interferometer is used to measure the electron density profile. Plasma electron temperature profiles were derived from the soft X-ray radiation spectrum measurements (XT_e-measurements). The high energy electron population created by ECCD is diagnosed primarily with a hard X-ray (HXR) pinhole camera (on loan from Tore Supra) and with a high field side electron cyclotron emission (ECE) system. The EC power deposition and current drive profiles (Fig.2) are calculated by the TORAY ray-tracing code with magnetic equilibrium reconstruction from the LIUQE code and Thomson scattering electron temperature and density profiles.

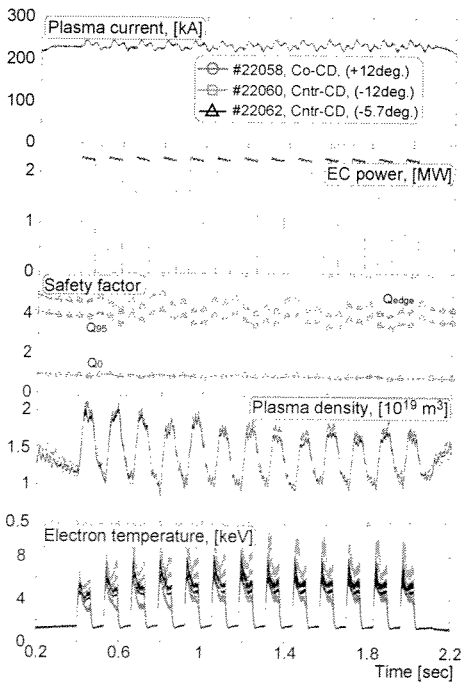

Fig.1: TCV discharges with different EC toroidal injection angles: Co-CD (+12°) – red, Cntr-CD (-12°) – green, Cntr-CD (-5.7°) – blue.

2. "CX-spectrum". The NPA charge-exchange spectra for the ON and OFF phases of the EC modulated regimes are shown in Fig.3. The measurements during EC injection reveal two ion populations, a thermal bulk (~500 eV) and a suprathermal component with an effective temperature up to 2.5 keV. The measured neutral flux indicates that the density of suprathermal ions is up to 10% of the thermal ion density, and the energy content of suprathermal ions was up to 50% of the bulk ion energy. During the ECH OFF-phase only the thermal bulk ion population was detected. The carbon impurity C^{IV} ion temperature measured by a CXRS [10] technique was about 500 eV, and its increase during the EC pulses was less than 50 eV. The suprathermal population is established in less than 10 ms after EC switch-on (Fig.4), a considerably shorter time than the Coulomb thermal electron-ion equilibration time (typically 30-150 ms). The variation of the bulk ion temperature is in good agreement with a classical model based on thermal equilibration of a multi-component plasma.

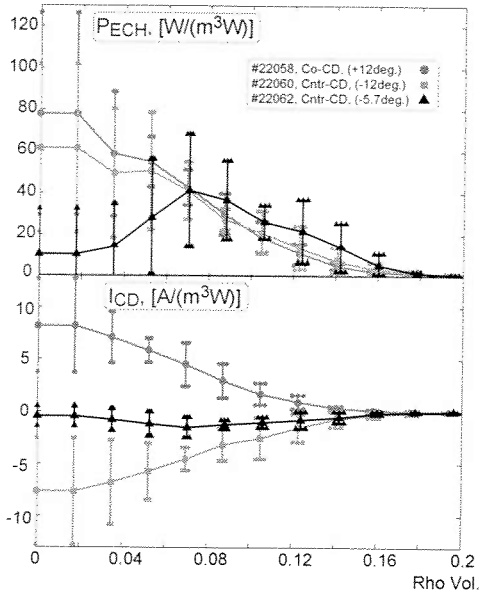

Fig.2: Co- and Cntr-CD discharges: EC power deposition density and CD profiles (TORAY calculation).

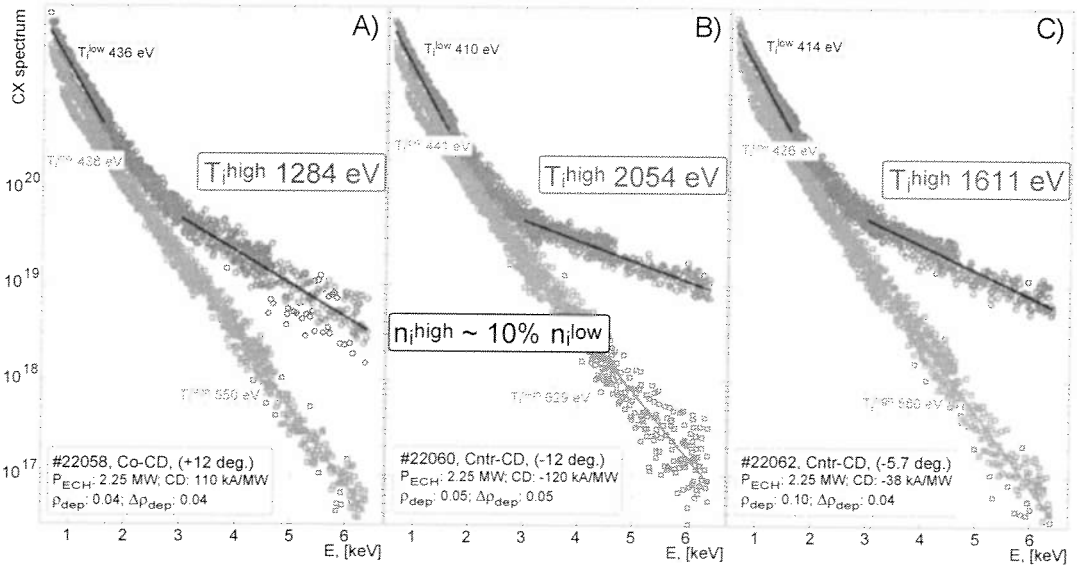

Fig.3: CX-spectrum for EC ON and OFF phases

A) Co-ECCD shot: P_{ECH}:2.25 MW, θ_{tor}:+12°, CD efficiency:110 kA/MW, $\rho_{dep.}$:0.04, $\Delta\rho_{dep.}$:0.04.

B) Cntr-ECCD shot: P_{ECH}:2.25 MW, θ_{tor}:-12°, CD efficiency:-120 kA/MW, $\rho_{dep.}$:0.05, $\Delta\rho_{dep.}$:0.05.

C) Cntr-ECCD shot: P_{ECH}:2.25 MW, , θ_{tor}:-5.7°, CD efficiency:-38 kA/MW, $\rho_{dep.}$:0.1, $\Delta\rho_{dep.}$:0.04.

3. Scans of EC deposition radius and toroidal injection angle. The suprathermal ion density and effective temperature were observed to be sensitive to the EC deposition position and toroidal injection angle. The effect is small for perpendicular injection (pure ECH) (Fig.5). For similar EC power deposition, current drive (Fig.2), electron density profiles, the population is more pronounced for CNTR-CD then for CO-CD discharges (Fig.3,5).

The hot ion feature is not observed when the deposition location is placed outside the sawtooth inversion radius (ρ~0.4) (Fig.6). For on-axis EC power deposition, the density of suprathermal ions and their effective temperature were proportional to the ECH power. A correlation between temperatures of suprathermal ions and bulk electrons was observed in the TCV experiments.

The characteristics of suprathermal ions are also sensitive to the plasma geometry. The effective temperature of fast ions decreases with plasma elongation and increases with plasma triangularity (Fig.7). Both dependencies are opposite to the temperature behaviour of bulk ions and carbon impurities.

4. Discussion and conclusions. The generation of suprathermal ions cannot be explained by the classical theory of two-body Coulomb collisions. Additional anomalous wave-ion [8] or electron-ion coupling [12] effects will have to be considered to understand this phenomenon. The mechanism of this effect is still an open question.

Our 5-ch. NPA with electrostatic analysis has significant limitations for studding the suprathermal ion dynamics: its time resolution (13 ms) is greater than the characteristic time of creation of suprathermal ion population after EC switch-on; it does not separate the neutral fluxes of the different hydrogen isotopes (H and D); and the spectrum of fast particles with energy beyond 6.5 keV cannot be detected with this NPA. A new NPA

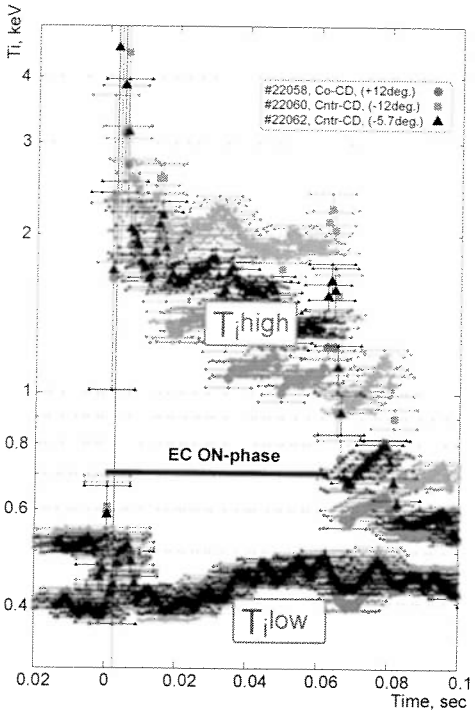

Fig.4: T_i^{high} and T_i^{low} temporal behaviour for a few periods of EC modulation, 3 toroidal injection angles.

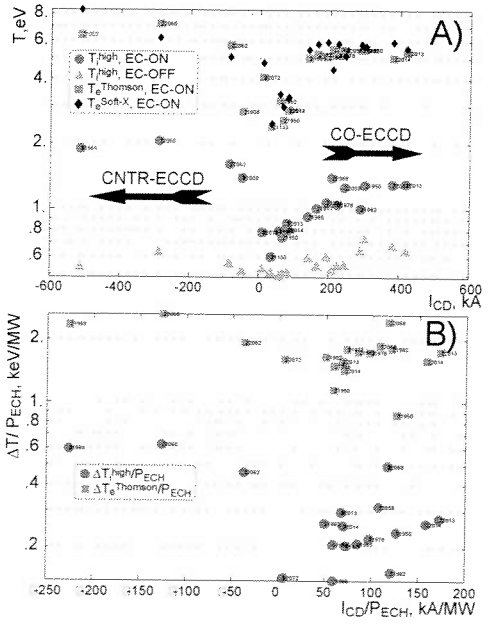

Fig.5: Toroidal EC injection angle scan:
(A) T_i^{high} vs. CD current, the T_i^{low} and T_e are shown for comparison;
(B) Efficiency of high energy ion tail production ($\Delta T_i^{high}/P_{ECH}$) and electron heating ($\Delta T_e^{Thomson}/P_{ECH}$) vs. current drive efficiency (I_{CD}/P_{ECH})

(Compact NPA [11]) soon to be installed on TCV will be employed to extend the experimental database and shed further light on the suprathermal ion dynamics in the presence of ECH and ECCD.

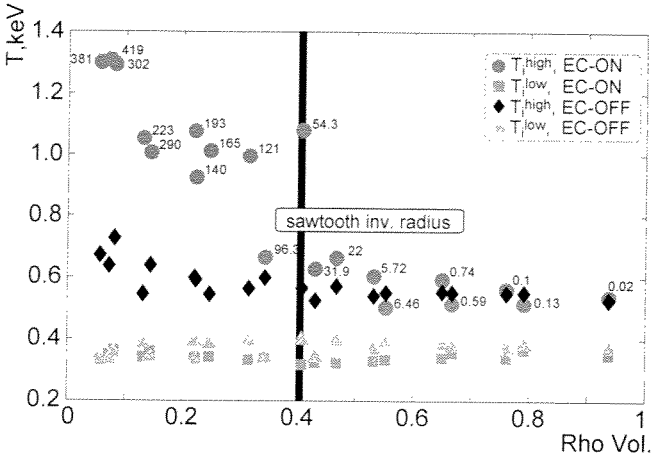

Fig.6: NPA Ion Temperatures vs. EC deposition location (labels: I_{CD}(kA)) for 2.4 MW of EC injected power.

References:

1. T.P.Goodman et al., Proc. 19th IAEA Fusion Energy Conf., Lyon, France, 2002 (IAEA, Vienna, 2002), CD-ROM file OV/4-2.
2. T.P.Goodman et al., Proc. 2nd Europhysics Topical Conf. on Radio Freq. Heating and CD of Fusion Devices, Brussels, Belgium, 1998, Europhys. Conf. Abstr. **22A**, p.245.
3. V.V.Afrosimov et al., *Sov. Phys. - Tech. Phys.* **20**(1), (1975) 33
4. F.S.McDermott, et al., *Phys. Fluids* **25**(9), pp.1488-1490, (1982)
5. D.G.Bulyginsky, et al., 11th EPS Conf. on On Controlled Fusion and Plasma Physics, Aachen, Cont. papers, part I, pp.457-460 (1984).
6. Z.A.Pietrzyk, et al., *Nuclear Fusion,* **33**(2), pp.197-209,(1993)
7. V.Erckmann, et al., Proc. X Intern. Conf., Plasma Phys. and Controlled Nuclear Fusion Research, London, 1984, Nucl. Fusion, Suppl. Vol.2 IAEA, Vienna, pp.419-29 (1985)
8. V.Erckmann and U.Gasparino, *Plasma Phys. Control. Fusion* **36**, (1994) 1896
9. A. Karpushov, P.Bosshard, B. P. Duval, J. Mlynar, 29th EPS Conference on Plasma Phys. and Contr. Fusion, Montreux, ECA 26B (2002) P-4.119.
10. P.Bosshard, B. P. Duval, A. Karpushov, J. Mlynar, 29th EPS Conference on Plasma Phys. and Contr. Fusion, Montreux, ECA Vol. 26B (2002), P-4.120.
11. F.V.Chernyshev et al., This Conference, Poster P-4.71 (see also http://www.ioffe.rssi.ru/ACPL/npd/npa05.htm)
12. B.Coppi et al., *Nucl. Fusion* **16**(2) pp.309-328 (1976)

This work was partly supported by the Swiss National Science Foundation.

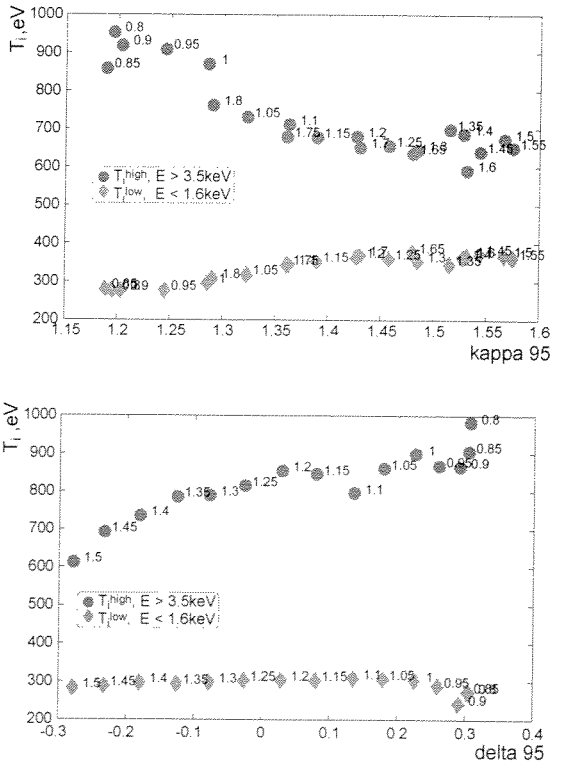

Fig.7: Plasma elongation and triangularity scan with EC power 1 MW.

An Open Architecture Version of the DINA 1.5D Simulation Code

R.R. Khayrutdinov[2], J.B. Lister[1], V.N. Dokuka[2], B.P. Duval[1], J-Y. Favez[1],
V.E. Lukash[3], D. Raju[4]

[1]*Centre de Recherches en Physique des Plasmas,*
Association EURATOM-Confédération Suisse, EPFL, 1015 Lausanne, Switzerland
[2]*TRINITI, Troitsk, Moscow Region, Russia*
[3]*Kurchatov RRC, Moscow, Russia*
[4]*IPR, Ghandinagar, India*

Introduction Considerable effort has been dedicated on several tokamaks to benchmarking the DINA 1.5D axi-symmetric, time-dependent tokamak plasma simulation code [1]. Ohmically heated TCV plasma discharges were successfully validated by a version of DINA into which the details of the tokamak, diagnostics and control system were hard coded [2,3]. These results encouraged us to extend the simulation to a full discharge evolution of shaped TCV plasmas with electron cyclotron heating. Difficulties in maintaining different versions of the code and in validating the implementation of the rather complex TCV control system forced us to look for a more open alternative. We therefore developed a new version of the DINA code, interfaced to a proprietary software package. In this paper we present the evolution of the DINA code for TCV and ITER. The simulations of TCV discharges and of the ITER modelled discharges presented in this paper using the DINA code are all part of a remote collaboration between the TCV team and the DINA code developers from the RRC Kurchatov and TRINITI institutes in Moscow.

Evolution of DINA into DINA-CH The first results on TCV [2] were generated in simulations in which the linearised plasma equilibrium response was of most interest and in which the precise implementation of the TCV control system model was less important. Some minor discrepancies between the modelling and the experiment were difficult to trace. At the same time, the complexity of the simulations was increasing all the time by including

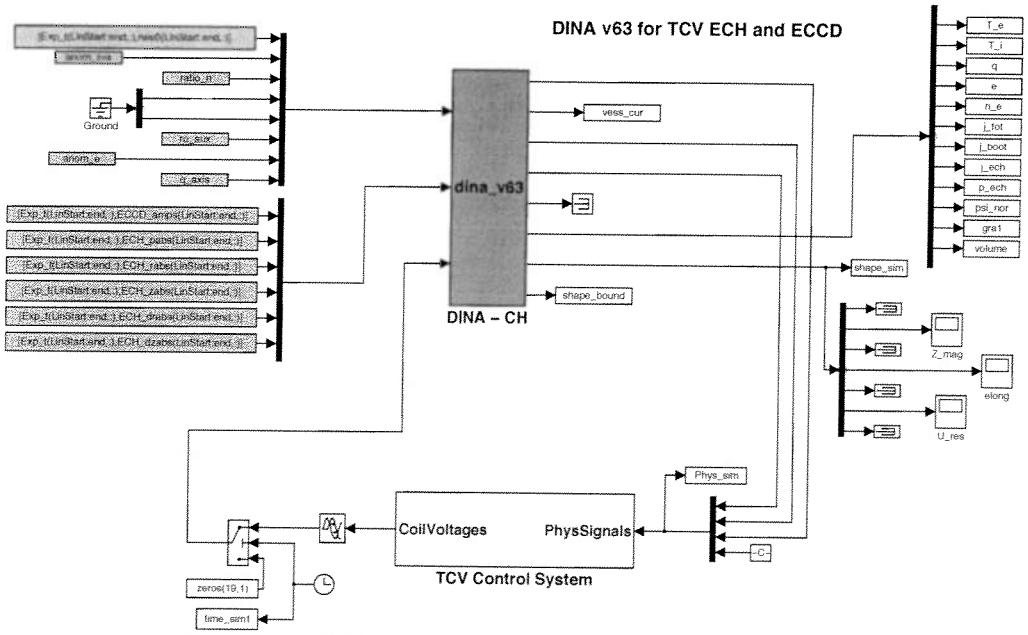

Fig.1: DINA-CH model for TCV, implemented under Matlab-Simulink, defining ECH and ECCD deposition in real space and implementing the full control system

the complex ECH/ECCD systems as well as the full description of the equilibrium control.
A collaborative effort was therefore undertaken to port the DINA simulation code, initially implemented in C/Fortran, into an open architecture. The environment chosen was the Simulink toolbox of the Matlab mathematical package [4], due to its widespread use in fusion laboratories, especially for plasma control applications. Matlab-Simulink offers transparent access to the tokamak simulation parameters, both those used as input to the simulation and to the simulation results themselves. It is well adapted to plasma control simulations due to a vast library of intrinsic functions available.
The full discharge simulation set up is created graphically, illustrated in Fig. 1. The DINA-CH code, solving the evolution equations, has specific real-time inputs on the left, including the coil voltages, the additional heating and current-drive, and transport factors. For each step of the evolution, the simulation data exit on the right hand side, including global parameters (shape, current), the last closed flux surface, the coil and passive structure currents and radial profiles as a function of poloidal flux. Since all variables are transferred within the Matlab environment, there is seamless transfer of the input data and the simulation data to direct visualisation of the results.
In a first phase of DINA-CH, the example shown in Fig.1, we removed constructional details of the TCV tokamak itself from the DINA code, leaving a generic plasma simulator, solving the free boundary equilibrium, the poloidal flux diffusion within the plasma and heat transport within the plasma. Details of the tokamak construction, including the passive structure of the vacuum vessel, Poloidal Field (PF) coils location, turns and resistances and diagnostics, are then provided as inputs to the simulation. An initialisation procedure provides the parameters for a reconstructed equilibrium, the feedback control system parameters and the feed-forward and feedback reference waveforms, which are needed to

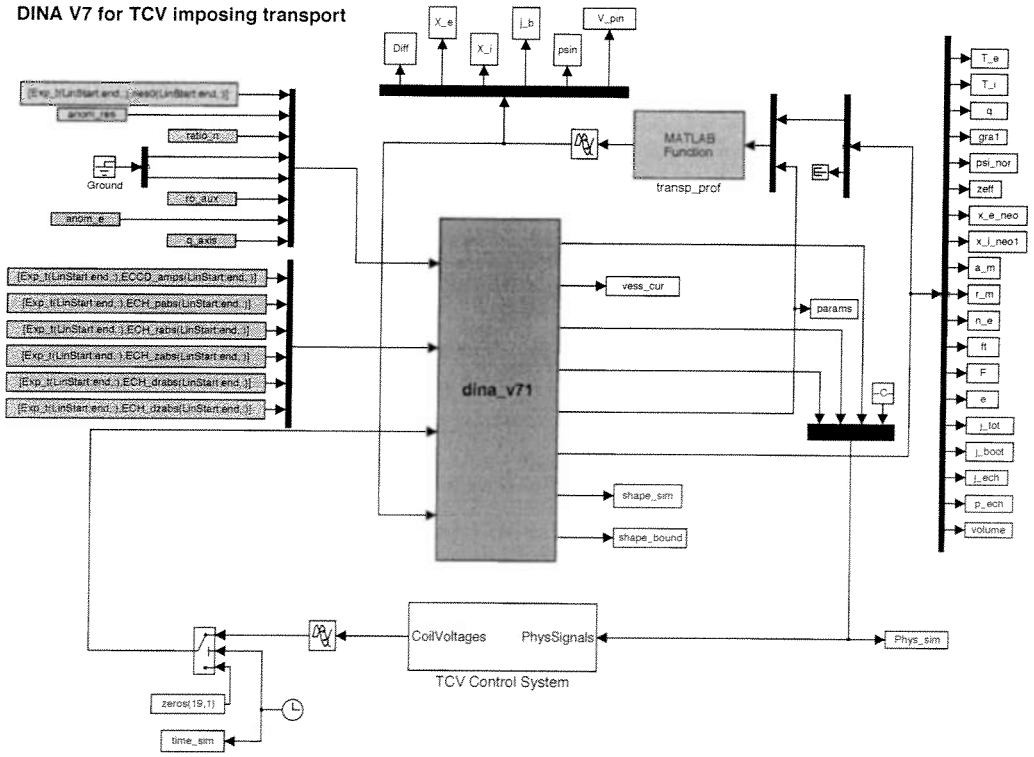

Fig.2: Second phase development for TCV, with user-specification of the transport coefficients, additional heating and plasma control

simulate the full TCV PF control system. Details of the power supplies and their saturation, together with the plasma position and shape control are explicitly represented in the Simulink environment, and are taken directly from the TCV discharge data. The additional heating and current drive on TCV are ECH/ECCD which are particular in that the additional power is defined in (R,Z) space, with refractive effects due to the equilibrium and its position. It was thought to be dishonestly inconsistent to impose the ECH/ECCD as functions of the flux coordinates, and then see if the equilibrium evolution agreed [5].
In a second phase, shown in Fig.2, the transport of heat, particles and poloidal flux has now been implemented oustide the base code, freeing DINA from a small set of pre-defined

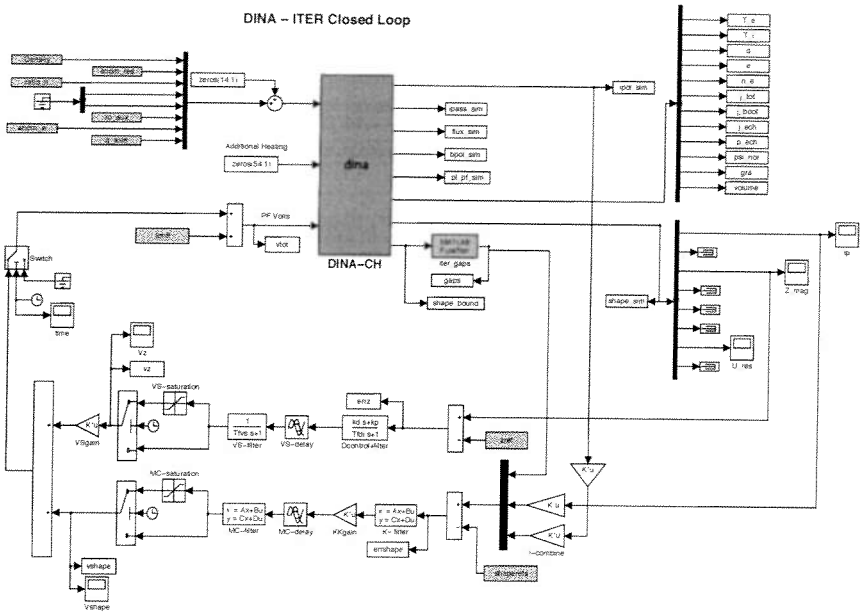

Fig.3: DINA-CH used for simulating 200 second ITER discharges, using the controller developed for the ITER

transport models, although these can be specified to be evaluated inside DINA by default. The transport module takes the complete profile data as input and derives the coefficients for the particle pinch and diffusion, electron and ion transport and the bootstrap current. This development opens DINA up for exploring different transport models in a rapid way, during complete simulations and specifically, to investigate the effects of the assumed transport on the evolution of the shape, seen in extreme off-axis ECH deposition experiments on TCV [5]. The major advantage is that there is no code modification necessary and that all information is explicitly available to the user. Development work can concentrate on refining the mathematics of the evolution, rather than on the transport. Application can concentrate on the physics, rather than on development of the code.

Implementation for ITER We have taken the ITER-CH Simulink implementation and included the nominal data for ITER. The loop was closed using the ITER reference controller [6], as shown in Fig.3. Power supply saturation was turned off for 2 seconds during the initial transient while DINA settles down to a self-consistent current profile, as was found necessary in TCV simulations [3]. Heat and particle transport was turned on, but no effort was made to adjust the coefficients.
A first long pulse test failed at 222 seconds and had a slow drift of the controlled parameters. The controller was modified to add integral gain with a 10 second time constant on all the 6 controlled gaps as well as the plasma current. This corrected the drifts and centred the gap

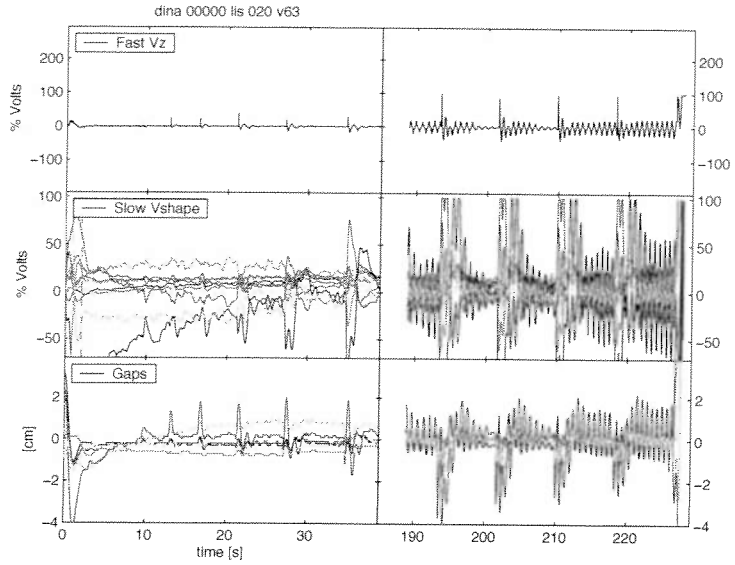

Fig.4: Evolution of the supply voltages and gaps

errors. However the simulation still terminated with a VDE, apparently due to slow evolution of the plasma equilibrium, which cannot be studied in the linearised model which was used to develop the controller. Work can now progress on designing a more robust controller for non-linear simulations.

Figure 4 shows that the power supply voltages (in % of the supply saturation) are within limits for both the fast and slow systems and that the gaps do not move by more than ±1.5cm during the sawtooth crashes, until the terminating VDE. Figure 5. shows the variation of the plasma current and Te(0) during the sawteeth as q(0) oscillates.

A 200 second simulation solving the equilibrium and transport evolution requires 4 hours on a 2.4GHz Pentium4 PC.

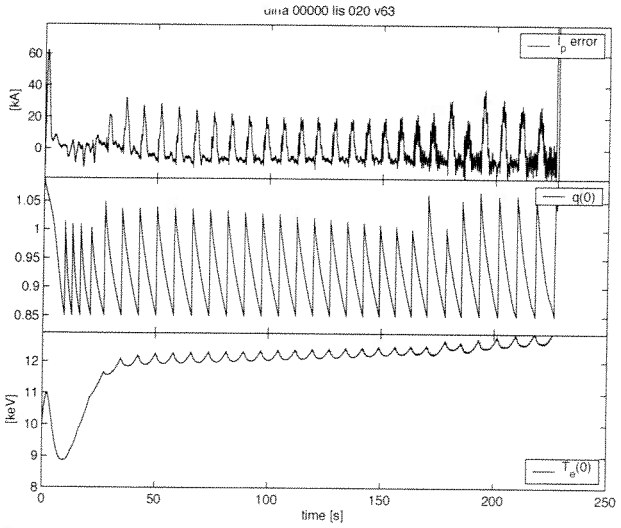

Fig.5: Control of the plasma current during sawtooth relaxations and the evolution of Te(0)

Future evolution A previous definition of auxiliary power defined in flux-surface space will be put back into DINA-CH, allowing flux-surface definitions of power loss, alpha power and heating power to be included as Matlab modules. DINA is tending towards a validated, efficient mathematical tool for solving the equilibrium and transport equations for a generic tokamak, allowing its use in a single version on a variety of tokamaks, thereby sharing the onerous validation.

Acknowledgements This work was partly supported by the Fonds National Suisse de la Recherche Scientifique. We are grateful to Y. Gribov and A. Kavin for making available the ITER reference controller for this work.

References

[1] R.R. Khayrutdinov and V.E. Lukash, J. Comp. Physics, **109** (1993) 193

[2] R.R. Khayrutdinov, J.B. Lister, V.E. Lukash and J.P. Wainwright, Plasma Physics and Controlled Fusion, **43** (2001) 321

[3] J-Y. Favez, R. R. Khayrutdinov, J. B. Lister and V. E. Lukash, Plasma Physics and Controlled Fusion, **44** (2002) 171

[4] "SIMULINK Dynamic System Simulation for Matlab", The Mathworks Inc., 2000

Simulation of TCV Equilibria Evolution using the DINA Code

V.E. Lukash[2], J.B. Lister[1], V.N. Dokuka[3], R.R. Khayrutdinov[3],
Y. Camenen[1], S. Coda[1], J-Y. Favez[1], A. Pochelon[1], O. Sauter[1]

[1]*Centre de Recherches en Physique des Plasmas,*
Association EURATOM-Confédération Suisse, EPFL, 1015 Lausanne, Switzerland
[2]*Kurchatov RRC, Moscow, Russia*
[3]*TRINITI, Troitsk, Moscow Region, Russia*

Introduction In previous work, we simulated the shape evolution of TCV equilibria during intense off-axis ECH heating using DINA-CH, a development of the DINA code [1,2]. This relatively simple experiment in fact presents a serious challenge to full tokamak discharge simulations. It requires accurate simulation of the diagnostics, power supplies and poloidal field coil plus vacuum vessel geometry. It needs a real-space (R,Z) description of the additional power deposition, taken from the TORAY ray-tracing code. It finally depends on an accurate free boundary evolution of the equilibrium to follow the control actions as well as the changes to the current and pressure profiles. Our first attempts at modelling these experiments showed reasonable agreement, but demonstrated a surprising sensitivity to the assumed model of the heat transport during the transient phase of the shape evolution. It would therefore appear that the shape evolution is implicitly capable of validating the underlying transport asumptions. Other challenges the DINA code has met recently, described in this paper, include modelling the effect of feedback on the varying evolution of these discharges, modelling high bootstrap fraction discharges and modelling the break between two gyrotrons driving the plasma current "back to back".

Off-axis plasma heating, without and with elongation feedback At low plasma current, elongating the equilibrium rapidly leads to loss of vertical control as the safety factor increases and the current channel shrinks. Intense off-axis ECH heating broadens the current profile and increases the elongation for fixed quadrupole field, allowing the exploration of ohmically inaccessible regions of k_{95}:I_p [3]. These discharges were modelled using DINA in earlier work [4].

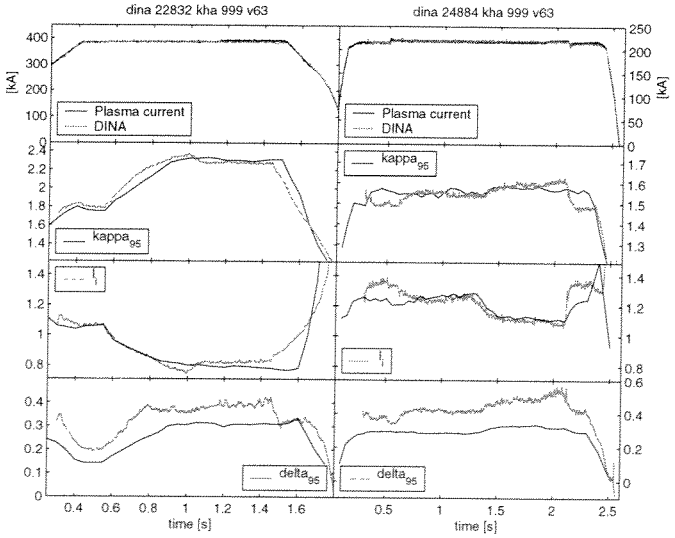

Fig.1: (left) intense off-axis ECH leading to a broadening of the current profile and an increase of the elongation; (right) change of the equilibrium compensated by "kappa-feedback" reducing the quadrupole field and minimising the change to elongation when the inductance decreases. Curves: red noisy are DINA, blue are reconstructed.

We have modelled more recent discharges, including a higher elongation, reaching k_{95}=2.3, illustrated in Fig.1 (left). Two, followed by three X2 gyrotrons delivered 0.85-1.15MW to a 400kA plasma current discharge. The agreement between the

simulation and the experiment is reasonable, when the transport model was adjusted. For this simulation the T-11 electron heat conductivity scaling [6] was used, normalised to Rebut-Lallia-Watkins global confinement which well represents TCV electron dominated confinement. Anomalous transport outside the Internal Transport Barrier (ITB) ($\rho>\rho_{ITB}=0.6$) was assumed to be a factor of 10 higher. The acceptable agreement shown in Fig.1 (left) was obtained with an improvement of the global energy confinement time by a factor of 4 and a change of the density peaking factor ($n_e(a)/n_e(0)$) in the region between 0.2 and 0.8 during the period 0.5-1.0s. At other times the peaking factor was maintained at 0.6. The beneficial influence of the density profile peaking was reported earlier on TCV [7]. The line-averaged density is not yet constrained to match the experimental value.
Work on the feedback control has compensated the increased elongation in the discharge shown in Fig.1 (right) in which the variation of k_{95} was minimal. 4 gyrotron beams delivered 1.4-1.6MW to a 200kA plasma. This discharge is also well modelled by DINA. In both conditions of Fig.1, the variation of δ_{95} was less accurately reproduced in the simulation.
In the previous simulations [2], it had been noticed that varying the electron transport led to differing evolution of the elongation. The discharge shown in Fig.1 (left) is remodelled in Fig.2 with two different transport assumptions. The only parameter varied was the density peaking factor, which has an effect on the T-11 transport model used in these particular simulations. This is not an artefact of this particular scaling, and assuming different transport models which affect the electron transport differently will show the same disparity between simulations.

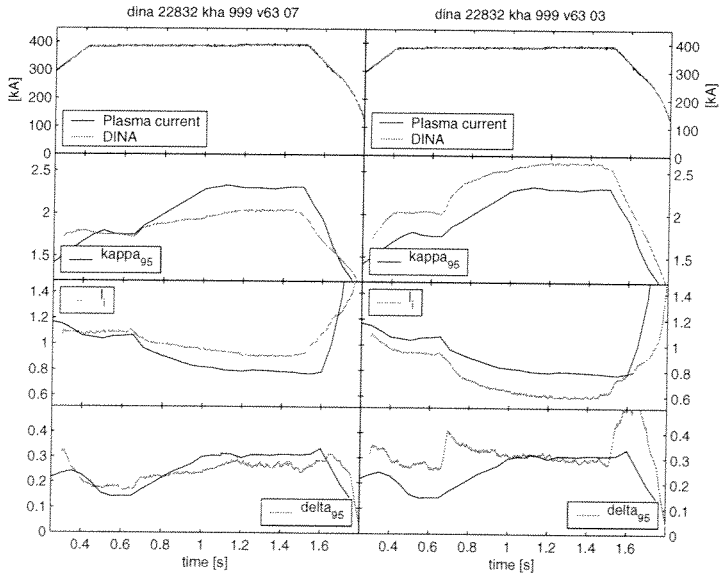

Fig.2: (left) the same discharge as Fig.1 (left) but with the density peaking decreased by an edge/axis ratio increasing from 0.6 to 0.7; (right) the same discharge simulated with an edge/axis ratio of 0.3, providing a much more peaked density profile. The edge density is held constant.

In Fig.1 (left) the ratio between the boundary and axis density was chosen to be 0.6. Broadening the density profile to a ratio of 0.7 yielded the simulation in Fig.2 (left) whereas a narrower density profile with a ratio of 0.3 produced the simulation in Fig.2 (right).
Comparing the quality of the agreement between the simulated and measured elongation, the sensitivity to the assumed transport is evident. Firstly, the maximum elongation is either too high or too low, implying that the current profile is inadequately described by the two outlying transport models. Secondly, the triangularity is similarly wrong, being either too weak or too strong. Thirdly, the time-evolution of the elongation is very slow in the case of Fig.2 (left) and too rapid in the case of Fig.2 (right). It is noticeable that the elongation and triangularity are not well reproduced in the ohmic phase of the discharge, before the additional heating is applied.

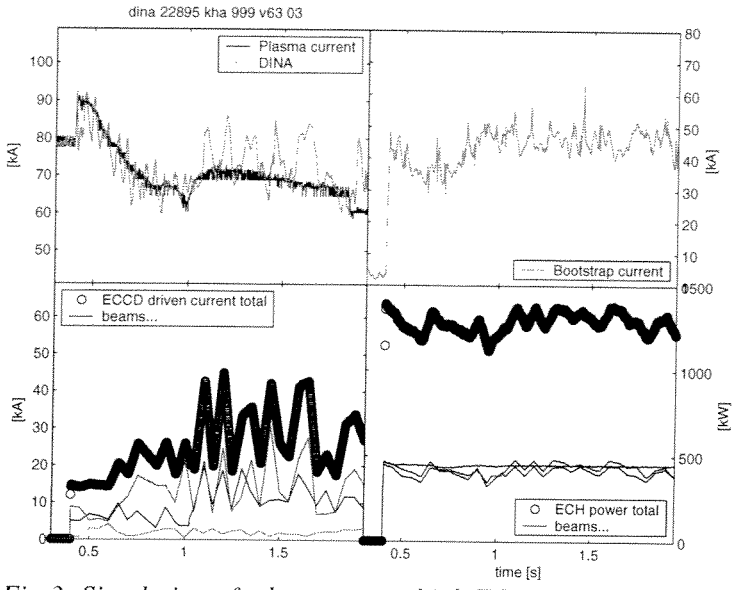

Fig.3: Simulation of a low current, high ECH power discharge with 42% driven current and 58% bootstrap current.

The time dependence of the absorbed power is input into DINA in a "box" in real space. The evolution of the equilibrium surfaces moves the deposited power as a function of flux surface. Although this is not strictly consistent, since the evolution of the equilibrium should also move the deposition zone vertically due to time-varying refraction by the moving density profile, it is more consistent than assuming a given deposition on a flux surface which is moving in real space.

High bootstrap fraction simulation Recently, a combination of ECH and ECCD has been optimised to produce high bootstrap current fractions on TCV, using an internal transport barrier.These discharges make use of low total plasma current and high power. A typical case, with ~60% bootstrap fraction, estimated using PRETOR has now been modelled using DINA. Figure 3 illustrates one such simulation. The total plasma current stabilises for nearly one second at about 70kA. The power absorbed from 3 gyrotron beams averages 1.3MW. The beams also generate plasma current, estimated using the CQL3D code on the basis of the delivered power, cold plasma ray tracing and the reconstructed equilibrium and density profiles. Figure 3 shows that for relatively steady ECH power, the variation in the driven current time-trace is very large, around ±50%. As in the previous case, the driven current is defined in a "box" in real space, to be more self-consistent. The variation of the driven current is not self-consistent with the deposited power, but reflects the difficulties of estimating the driven current from the reconstructed profiles.
Notwithstanding these imprecisions, the DINA simulation of the total current evolution is accurate and the bootstrap current agrees with the non-evolutionary code estimates.

Modelling the interruption of current drive An issue when driving current non-inductively is to know what the requirements are on matching the power and deposition profile with a reserve gyrotron if one source should drop out. A set of discharges was run on TCV to investigate this and one of these was chosen for a DINA simulation. Figure 4 illustrates some of the results for a discharge in which the inductive current drive has been forced to zero by feedback control of the transformer current change. This is therefore an example of a 100% non-inductively driven discharge. The interruption in the external current drive is expanded in the right-hand column.
The driven current is adjusted to be in good agreement with the experiment during the whole ECCD pulse.

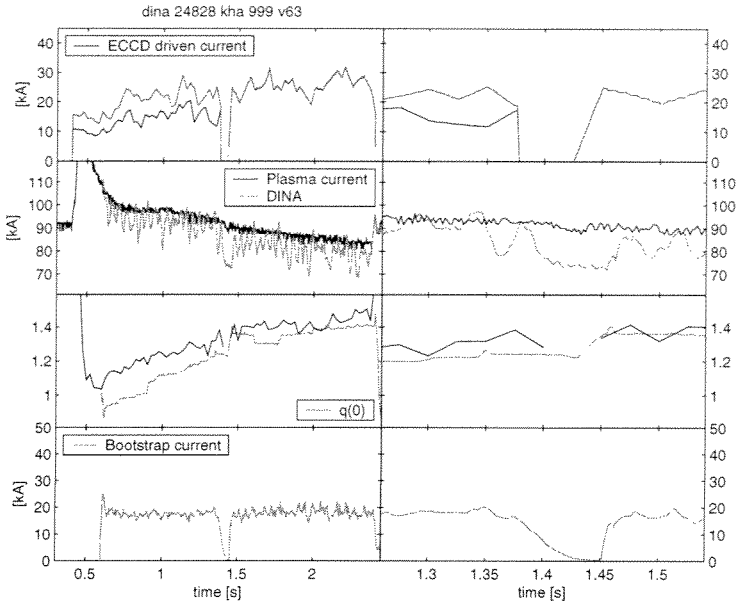

Fig.4: A discharge in which the driven current is provided by two different pairs of sources, with a brief interval between them (expanded in the right-hand column)

The most significant difference between the experiment and the simulation during the interruption in the current drive is the sharp drop in the plasma current in the gap, attributable to the drop in the bootstrap current at the same time. This suggests that the bootstrap current is being underestimated during the gap due to a drop in the pressure profile which the experiment does not experience. This pressure drop appears to be an artefact of the simulation and will be the object of future investigation.

Discussion The validation of the DINA code, in its version DINA-CH, has gone through the purely inductive plasma equilibrium response tests, through to the VDE evolution in the spatially varying vacuum field of TCV. We have modelled the effect of localised deposition of ECH power and ECCD, prescribed from LORAY calculations which are at present too onerous to include in the real-time simulation. The effect of this local deposition on the evolution of the equilibrium and its control can only be studied in a code with free boundary evolution and control modelling, such as DINA. The effect of different transport models can be studied in the new version with externally imposed definition of the functional dependence of transport on the profiles [1]. We have now validated the bootstrap current modelling in DINA-CH. At present, only the modelling of a brief interruption of the current drive shows unexplained features.

Acknowledgements This work was partly supported by the Fonds National Suisse de la Recherche Scientifique.

References

[1] R.R. Khayrutdinov, J.B. Lister, V. Dokuka, B.P. Duval, J-Y. Favez, V.E. Lukash, D. Raju « An Open Architecture Version of the DINA 1.5D Simulation Code», this conference.
[2] R.R. Khayrutdinov and V.E. Lukash, J. Comp. Physics, **109** (1993) 193
[3] A. Pochelon et al., Nuclear Fusion 41 (2001) 1663
[4] V.E. Lukash, D. Raju, V.N. Dokuka, J-Y. Favez, R.R. Khayrutdinov, J.B. Lister, SOFT Conference 2002, accepted for publication in Fusion Engineering and Design, 2003
[6] V.M. Leonov et al., In: PPCNFR/Confer. Proc., Brussels, 1980. Vienna: IAEA, 1981
[7] A. Pochelon, Y. Camenen, F. Hofmann et al., IAEA Fusion Energy Conference, Lyon 2002, EX/P5-14.

Tokamak Equilibria with Negative Core Current Density

A.A.Martynov[1], S.Yu.Medvedev[1], L.Villard[2]

[1] *Keldysh Institute, Russian Academy of Sciences, Moscow, Russia*
[2] *CRPP, Association Euratom-Confédération Suisse, EPFL, Lausanne, Switzerland*

Experimental observations of nearly zero toroidal current in the central region of tokamaks (the "current hole") raises the question of the existence of toroidal equilibria with very low or reversed current in the core. Toroidal axisymmetric equilibria with zero current density in a finite region in the plasma core were analytically [1] and numerically [2] investigated. However, a reversed current density in the core, accompanied with poloidal field reversal, prevents the existence of equilibrium solutions with nested flux surfaces, except for one-dimensional cases (e.g. a circular cylinder). More precisely, a closed magnetic flux surface with identically vanishing poloidal magnetic field can only exist if the current density is zero everywhere inside that surface [3]. On the other hand, more general axisymmetric equilibria with reversed current density and poloidal field do exist. These equilibria are characterized by the presence of axisymmetric magnetic islands.

Eigenfunctions of Grad-Shafranov operator Simple examples are readily given by the solutions of the eigenvalue problem

$$-R^2\nabla\cdot(R^{-2}\nabla\psi)=\lambda\psi, \quad \psi=0 \text{ at the boundary,}$$

which define force-free equilibrium configurations with a toroidal current density $j_\phi = \lambda\psi/R$. An equilibrium solution with nested flux surfaces $\psi = const$ corresponds to the lowest eigenvalue and an eigenfunction without nulls inside the domain. Plenty of other eigenfunctions provide a range of equilibria with a different topology of the magnetic surfaces. In the limit of infinite aspect ratio and circular cross-section (circular cylinder) the exact solutions of the eigenvalue problem are

$$\lambda = z_{m,k}^2, \quad \psi = J_m(\sqrt{\lambda}\rho)e^{im\theta}, \quad m,k=0,1,2,\ldots$$

where (ρ,θ) are polar coordinates, J_m and $z_{m,k}$ are Bessel functions and their zeros. Toroidicity and cross-section shaping lead to the coupling of poloidal harmonics and splitting of multiple eigenvalues. In 2D cases numerical solutions of the eigenvalue problem were found on a standard fixed grid by the inverse iteration method using the same difference scheme as in the CAXE code [4]. In finite aspect ratio tori, 2D-modified $m=0$, $k>0$ eigenfunctions were found in the spectrum (together with the 2D-modified $m>0$ multipole eigenfunctions). The eigenfunctions exhibit poloidal field reversal and magnetic island formation with the x-points inside the plasma domain (in contrast to the multipoles with x-points at the boundary) [5].

Formulation of equilibrium problem Two flux functions $p(\psi)$ and $f(\psi)$ should be prescribed to define the equilibrium toroidal current density

$$j_\phi = Rp' + ff'/R, \quad \text{where } p' = dp/d\psi,\ f' = df/d\psi.$$

Only force-free equilibria with zero pressure gradient $p'=0$ are considered here.

The first difficulty in posing a correct equilibrium problem with current density reversal is the different specification of the flux functions in the negative current density region in the core and the positive current density region outside it. This can be done if the two regions are delimited by some closed magnetic surface. Then the simplest choice is to use constant ff' both inside, $ff'=h_{in}<0$, and outside that surface, $ff'=h_{out}>0$. In the cylindrical limit a 1D solution with nested flux surfaces exists for any prescribed coordinate $\rho=\rho_d$ of the circular delimiting magnetic surface and for any pair of constants, h_{in} and h_{out}, in the current density definition. In general 2D cases, the position and shape of the delimiting surface should be calculated along with the solution of the equilibrium problem. Our method is to prescribe the diameter (horizontal size) of the delimiting surface $2a_d$ (in units of the plasma minor radius) and the current ratio I_{in}/I_{out}. Calculations show that this formulation can provide equilibrium solutions for a wide range of parameters.

On the basis of the CAXE code [4] the following numerical procedure has been developed. First, an approximation of the delimiting surface is obtained by tracing the flux surface through some reference node of the computational grid using current values of the function ψ. The corresponding index line of the polar grid is adapted to the delimiting surface and a usual Picard iteration is performed. To provide the required shift of the adaptive grid, a feedback procedure connected with the change of the delimiting surface position between the iterations is implemented (in non up-down symmetric cases not only a horizontal, but also a vertical shift feedback is needed).

Fig.1 demonstrates that, for a prescribed delimiting surface diameter, its shape and the shape of the islands change according to the value I_{in}/I_{out}.

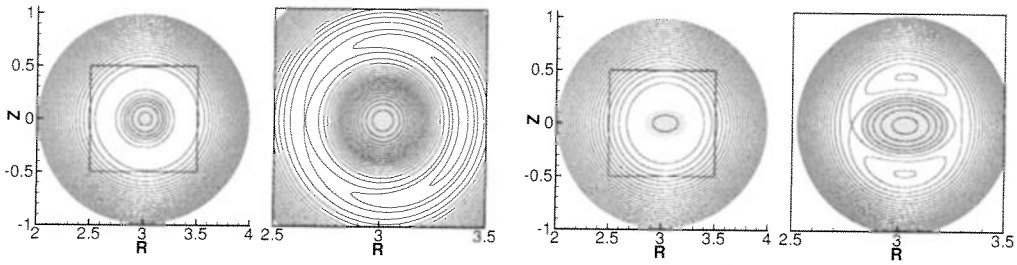

Fig.1 Magnetic surfaces for two values of I_{in}/I_{out}: -0.1 (left) and -0.03 (right). Aspect ratio $A = 3$, circular cross-section. The shaded regions correspond to the delimiting surface with $a_d = 0.2$ and $j_\phi < 0$ inside. Expanded central regions are also shown.

In Fig.2 the elongation of the delimiting surface and the ratio of the current densities are shown versus I_{in}/I_{out} for a fixed value of a_d. For negative values of I_{in}/I_{out} approaching zero the elongation of the delimiting surface decreases (becoming oblate) and the x-points approach the delimiting surface. This could possibly explain the limited range of the admissible negative values of I_{in}/I_{out}: no equilibrium solution was found in the series with fixed delimiting surface diameter for $I_{in}/I_{out}/a_d^2 \gtrsim -0.5$. The current density ratio h_{in}/h_{out} is non-monotonic versus I_{in}/I_{out} and two different equilibrium solutions exist with the same h_{in}/h_{out} and different I_{in}/I_{out} values. For the normalized current ratio $I_{in}/I_{out}/a_d^2$ all functions shown in Fig.2 depend weakly on the boundary aspect ratio and the delimiting surface diameter. However, the current density limit significantly varies with the boundary elongation.

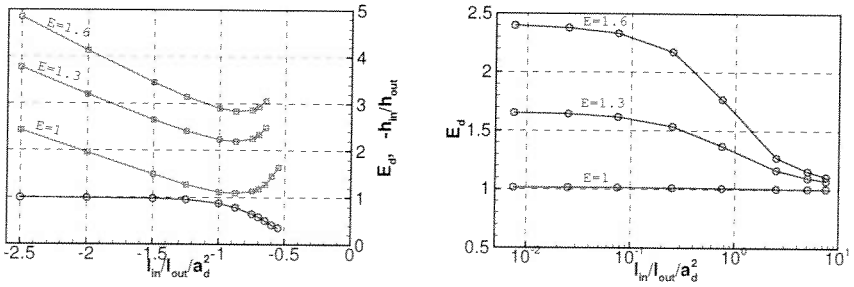

Fig.2 Delimiting surface elongation E_d (red circles) versus $I_{in}/I_{out}/a_d^2$ for negative (left) and positive (right) core currents. $A = 3$, $a_d = 0.2$. The current density ratio h_{in}/h_{out} is given for boundary elongations $E = 1$, $E = 1.3$ and $E = 1.6$ (left, green squares).

The same equilibrium formulation can be used with positive values of $I_{in}/I_{out} > 0$ to get nested flux surface configurations with a current hole equilibrium in the limit $I_{in}/I_{out} \to +0$. The delimiting surface elongation depends quite strongly on the current ratio in the range $0.1a_d^2 < I_{in}/I_{out} < a_d^2$, when the current profile becomes hollow (the value $I_{in}/I_{out}/a_d^2$ corresponds to the current density ratio h_{in}/h_{out} for a delimiting surface similar to the plasma boundary) with the elongation limit always higher than that of the plasma boundary (Fig.2,right).

Big negative current In general, prescribing the horizontal size $2a_d$ and the current ratio $I_{in}/I_{out} < 0$ does not guarantee the uniqueness of the equilibrium solution. Several solutions can exist for sufficiently negative $I_{in}/I_{out} < 0$ (Fig.3). However, for a given value of $I_{in}/I_{out} < 0$ there is at most only one solution with internal x-points and nested flux surfaces near the boundary. All other solutions (multipole type) exhibit x-points at the surface and therefore cannot be embedded into an external nested flux surface configuration without breaking the poloidal magnetic field continuity.

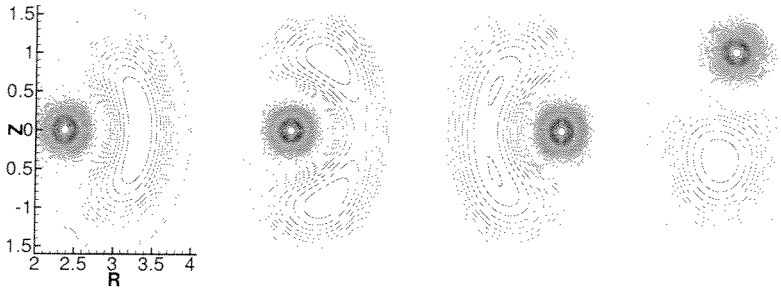

Fig.3 Several equilibrium solutions with the same values of $a_d = 0.2$ and current ratio $I_{in}/I_{out} = -0.5$. $A = 3, E = 1.5$.

The value $I_{in}/I_{out} = -1$ corresponds to the equilibrium with total plasma current $I = 0$, in which case the normal derivative of ψ at the boundary must change sign (it is zero in average and can be identically zero only in the 1D case), which corresponds to the existence of an x-point at the plasma boundary, where $d\psi/dn = 0$. For sufficiently negative $I_{in}/I_{out} < -1$ the poloidal field eventually reverses in the whole plasma volume and a configuration with nested flux surfaces is restored (Fig.4). The kind of solution with nested flux surfaces (corresponding to reverse current density near the edge rather than in the core as long as $|I_{in}| > |I_{out}|$) exists for any delimiting surface diameter. However, for a_d close to 1 there is only one solution branch of type presented in Fig.4 (negative current at low field size) in contrast to multiple solutions for small a_d values. The equilibrium sequence from Fig.4 leading to total current reversal shows that plasma equilibria can subsist during the AC operation of tokamaks, as was demonstrated experimentally [6].

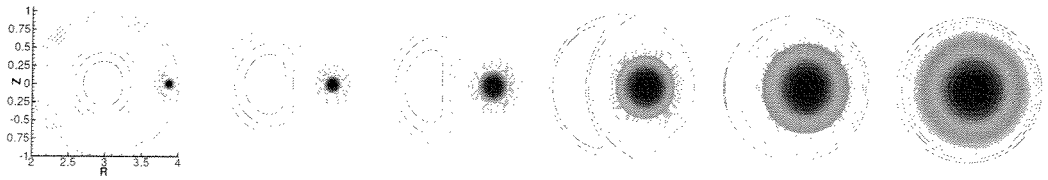

Fig.4 Series of equilibria with increasing negative current, both in size and value: $a_d(I_{in}/I_{out}) = 0.05(-0.2), 0.1(-0.4), 0.2(-0.6), 0.4(-1.0), 0.6(-1.5), 0.8(-2.0)$. $A = 3$.

JET equilibrium "reconstruction" In a recent paper [7] a quite detailed reconstruction of a JET equilibrium with extreme shear reversal was reported. The equilibrium formulation described above provides a possibility of finding similar equilibria with different magnetic field structures in the current hole. To model the hollow current density outside the current hole the following parameterization was used: $ff' = (1 - f_1)a^{e_1}(1 - a)^{e_2}/c + f_1(1 - a)$, $e_1 = e_2 a_*/(1 - a_*)$, $c = a_*^{e_1}(1 - a_*)^{e_2}$, where the exponent $e_2 = 2$ and the parameter $a_* = 0.1$ are prescribed. The flux surface label a outside the delimiting flux surface with $\psi = \psi_{del}$ is defined as $a = (\psi - \psi_{del})/(\psi_{bou} - \psi_{del})$, where ψ_{bou} is the value at the plasma boundary. A constant $ff' = f_1 = 0.01$ was specified inside the delimiting surface ("current hole") with $a_d = 0.3$. This gives the equilibrium with nested flux surfaces shown in Fig.7(left) with the current inside the current hole about 0.3% of the total current (the value of the rotational transform in the plasma center is $1/q \sim 1/200$). For the second equilibrium (Fig.7, right) one more delimiting

surface was introduced with $a_d^- = 0.1$ and constant negative current density $h_{in} = -0.037$ inside it and $h_{out} = 0.01$ outside. The resulting elongation of the negative current region is $E_d^- = 0.65$ which is close to the limiting value. In both cases the elongation of the current hole $E_d = 2.1$ is higher than the boundary elongation $E = 1.7$. The ideal MHD stability of the equilibrium with nested flux surfaces was calculated using the KINX code [8]. Due to a sufficiently high global shear ($q_{95} = 5.75$, $q_{min} = 3.25$) the equilibrium is stable against external kink modes.

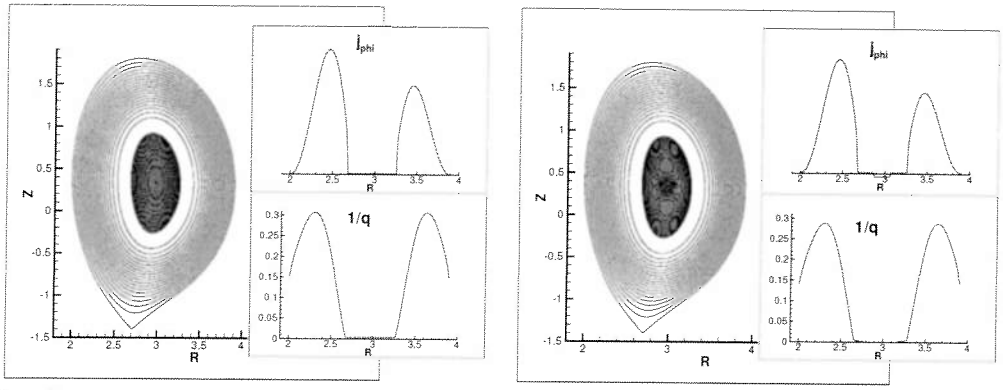

Fig.7 Magnetic surfaces for the current hole equilibria with JET geometry. The shaded regions correspond to the delimiting surfaces. The level lines of ψ are given for equal steps in ψ inside and outside the current hole. In the inserts the toroidal current density and the rotational transform profiles in the plasma equatorial plane are shown.

Conclusions The proposed equilibrium problem formulation allowed us to compute a wide range of equilibria with negative current in the plasma core. In plasmas with finite aspect ratio or elongation, the current density reversal leads to the formation of axisymmetric magnetic islands and these have been computed self-consistently. The question of the relevance of the proposed equilibrium solutions to experiments is open. While the approach presented here is applicable to more general plasma profiles and finite β, force-free configurations seem to be a suitable model for the current hole investigation because of the very flat pressure profile inside it. The MHD stability of 2D equilibria with negative central current should be investigated. In particular, it would be a natural extension of current hole stability and evolution studies [9, 7, 2]. In the context of the possible AC operation of tokamaks, we have shown that a wide range of equilibria can exist during total current reversal, including cases with a large dipole current, in agreement with experiments [6].

Acknowledgements Authors thank Drs V.V. Drozdov and J.B. Lister for very useful discussions and comments. The work was supported in part by the Swiss National Science Foundation.

References

[1] M.S. Chu, P.B. Parks, Phys. Plasmas **9,** 5036 (2002)
[2] B.C. Stratton *et al.*, PPPL-3756, October (2002)
[3] G.W. Hammett, S.C. Jardin, B.C. Stratton, PPPL-3788, February (2003), submitted to Phys. Plasmas
[4] S. Medvedev *et al.*, 20th EPS Conf. Lisbon, Proc. Contrib. Papers vol.IV, 1279 (1993)
[5] A.A. Martynov, S.Yu. Medvedev, L.Villard, CRPP-LPR 755/03, March (2003), submitted to Phys. Rev. Letters
[6] J. Huang *et al.*, Nucl. Fusion **40,** 2023 (2000)
[7] B.C. Stratton *et al.*, Plasma Phys. Control. Fusion **44,** 1127 (2002)
[8] L. Degtyarev *et al.*, Comput. Phys. Commun. **103,** 10 (1997)
[9] G.T.A. Huysmans, *et al.*, Phys. Rev. Lett. **87,** 245002 (2001)

Edge Kink/Ballooning Mode Stability in TCV

S.Yu.Medvedev[1], A.Degeling[2], Y.Martin[2], O.Sauter[2], L.Villard[2]

[1]*Keldysh Institute, Russian Academy of Sciences, Moscow, Russia*
[2]*CRPP, Association Euratom-Confédération Suisse, EPFL, Lausanne, Switzerland*

High-n ideal modes are thought to play a significant role in edge localized mode (ELM) relaxation dynamics. The key element in the existing ELM models is the MHD stability boundary in plasma edge current density and pressure pedestal parameter space [1]. Robust stability boundaries against ideal MHD modes can be computed taking into account a magnetic field separatrix at the plasma boundary.

1 Edge mode stability with separatrix A conventional way of edge instability interpretation is based on analytical considerations taking into account the coupling of localized peeling and high-n ballooning modes. The presence of a magnetic field separatrix at the plasma boundary leads to the stabilization of ideal localized peeling modes which require the presence of a rational magnetic surface just outside the plasma surface. While peeling mode instability is possible in limiter plasma, there are more robust modes which establish stability boundaries in the space of edge current density and pressure gradient parameters. A simple way to decouple from the peeling mode in limiter plasmas is to keep rational surfaces in vacuum far from the plasma edge so that the corresponding value of $m - nq \sim 1$ at the plasma boundary. Taking into account the separatrix naturally decouples peeling modes and gives kink/ballooning mode stability limits which do not depend on small variations of the edge safety factor [2]. Both purely current driven external kink modes and coupled kink/ballooning modes can set stability limits for the current density and pressure gradient values near the plasma boundary.

Localized peeling mode criterion application to divertor plasmas is problematic [3] due infinite safety factor at the separatrix. This is an essential difficulty also for numerical modelling of the separatrix plasma. However in finite elements codes there is a possibility to model the separatrix stabilizing influence without excessive resolution near the plasma boundary. It is based on the ideal stability formulation using $\xi \cdot \nabla\psi$ as one of the projections of the plasma displacement ξ and taking into account that the equilibrium poloidal flux gradient $\nabla\psi$ vanishes at the x-point [4]. Setting $\xi \cdot \nabla\psi = 0$ at one of the points at the boundary stabilizes the peeling modes in limiter plasma also, leaving global external kink modes virtually unaffected. The recent version of the KINX stability code uses a new variant of ballooning factor extraction applicable to equilibria with separatrix. Setting plasma displacement to zero inside a prescribed magnetic surface and solving only for displacements in the rest of plasma provides a possibility to increase the radial resolution near the plasma edge and treat modes with toroidal wave numbers up to $n \approx 60$ at resolution 1024×384 in radial and poloidal directions respectively.

2 Stability diagrams for TCV The reconstructed TCV equilibrium (shot #20333) with separatrix at the boundary is a starting point for the stability analysis. The following procedure was proposed for the stability diagram calculation:

- change independently the edge current density and pressure gradient profiles by adding the following functions to the original reconstructed ones (Fig.1):

  $$h\left(1 - \tanh^2\left(\frac{x_0 - s}{w}\right)\right),$$ where s is the square root of normalized poloidal flux.

- compute the stability boundaries for different chosen mode numbers n varying either current density $h = J$ or pressure $h = P'$ pedestal heights.

The width of the pedestal w and the location of the pedestal x_0 (leading to different current density values at the separatrix) are independent parameters in the study.

The first series of the computations with $x_0 = 1$ corresponds to maximum of P' located at the separatrix and a current density at the edge equal to the height of the pedestal. The obtained results are summarized in Fig.2a. Here the stability boundaries are given for three values of the pedestal width w and different toroidal wave numbers n. Marginally stable value of edge current density is almost constant with increasing edge

pressure gradient up to the ballooning limit and then decreases with increasing P'. There are no signs of second stability access with increasing n up to 60: the stability region in the (P', J) plane just shrinks slightly with increasing toroidal wave number. One can also notice that stability boundaries for different pedestal width w and different n but with the same product $w \times n$ are close to each other.

The situation changes if pedestals are inside the plasma ($x_0 < 1$) and J_{edge} is lower than its maximal value near x_0. There is a second stability access for the modes with $n \gtrsim 20$ in this case (Fig.2b).

The $w \times n$ scaling applies also to the wave numbers of the most unstable modes for a fixed value of $J_{edge}/J_{max} < 1$. Series of equilibria with self-consistent bootstrap current were used to demonstrate that. In the table below the marginal values of edge pressure gradient P' (in units of pressure gradient at magnetic axis) are presented for different values of n for $P'_{edge}/P' = 0.42$ and two width parameters w. Let us note that the marginal values of P' in the series with bootstrap current calculations are somewhat higher than that derived from the $J_{bootstrap}(P')$ curve in the Fig.2. This is connected with the slight decrease of bootstrap current density at the separatrix compared to the maximal values of $J_{bootstrap}$ near the boundary (compare Fig.1b and Fig.1c).

n	$P' : x_0 = 0.98, w = 0.02$	n	$P' : x_0 = 0.99, w = 0.01$
10	1.9304	20	1.9333
15	1.8974	30	1.8984
20	1.9336	40	1.9381

The next table corresponds to $P'_{edge}/P' = 0.18$ and shows that the range of most unstable modes shifts to lower values of n with pedestal moving deeper into plasma (in other words the second stability access takes place for lower values of n).

n	$P' : x_0 = 0.97, w = 0.02$	n	$P' : x_0 = 0.985, w = 0.01$
8	2.3955	16	2.4144
9	2.3923	18	2.4119
10	2.4025	20	2.4210

The mode structures of current driven and kink/ballooning modes with different n are given in Fig.3.

3 ELM models We propose the following semi-empirical model of ELM dynamics based on the triggering of the above current-driven ideal MHD instabilities. Let P', J and W be the edge pressure gradient and current density pedestals and W a mode amplitude. We write $dP'/dt = Q_{in} - WP'$, $dJ/dt = -(J - J_{bs}(P') - J_{OH} - J_{CD})/\tau_J$, $dW/dt = \gamma(P', J)W$; Q_{in} represents the average power flux into the edge layer. The growth rate is $\gamma(P', J) = (J - J_{crit}(P'))/\tau_{ideal}$ if $J > J_{crit}$ and $(J - J_{crit}(P'))/\tau_{decay}$ if $J < J_{crit}$. The current relaxation time τ_J and the mode decay time τ_{decay} are parameters of the model. The function $J_{crit}(P')$ parametrises the marginal stability boundary obtained from the stability calculations. Fig.4 shows trajectory in (P', J) plane and the time behaviour of P', J and W with typical relaxation oscillations. The ELM frequency is found to increase with increasing input power Q_{in}, typical of type-I ELMs. In contrast to the model used in [5] the ELM cycles are reproduced without requirement that $J_{crit}(P')$ is increasing function of P'. Moreover no ELM-type solution exist if the stability boundary is similar to the localized peeling mode stability boundary shown in Fig.2a.

4 Discussion Robust edge current driven and kink/ballooning mode ideal stability limits were found when separatrix at the plasma boundary is taken into account. The stability boundaries scales well with the product of the pedestal width by the toroidal wave number. Second stability access for higher n modes due to off-edge pedestal location was

discovered. The proposed semi-empirical model was shown to reproduce the ELM-type behaviour with the input marginal stability boundary typical to plasmas with separatrix.

Acknowledgements The CRPP authors are supported in part by the Swiss National Science Foundation.

References

[1] P.B.Snyder *et al.*, *Phys. Plasmas* **9**(2002)2037
[2] S.Yu.Medvedev *et al.*, 29th EPS Conf. Montreux, ECA Vol. 26B, P-1.116 (2002)
[3] J.W.Connor *et al.*, *Phys. Plasmas* **5**(1998)2687
[4] L.Degtyarev *et al.*, *Comput. Phys. Comm.* **103**(1997)10
[5] A.W. Degeling *et al.*, LRP 753/03 March 2003. Accepted for publication in Plasma Phys. Controlled Fusion

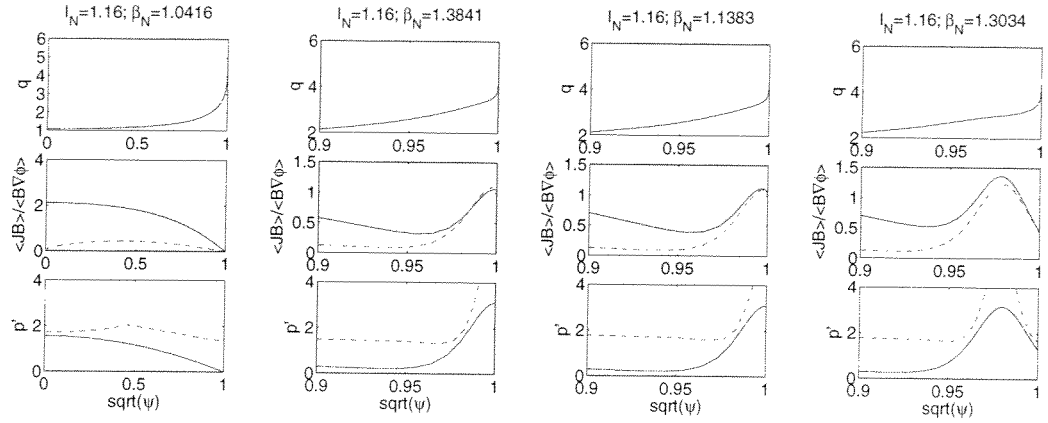

Fig.1 Profiles of the TCV shot #20333 reconstructed equilibria (a) and zoomed region near the boundary with different pedestal profiles corresponding to prescribed (b) ($P' = 2, J = 0.5$) and self-consistent bootstrap (c, d) ($P' = 2$) current density. The bootstrap current and marginal ballooning pressure gradient are shown by dashed lines

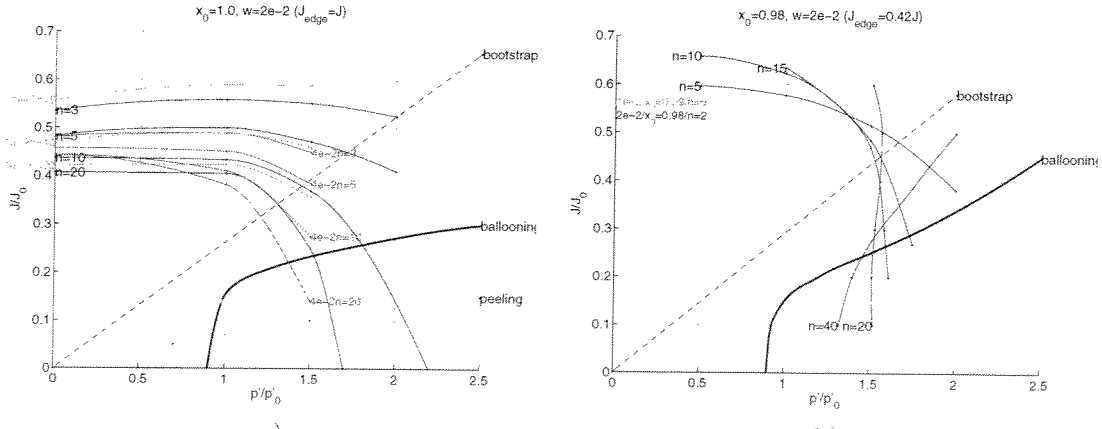

Fig.2 Stability diagrams for the case with pedestal at the separatrix (a) and inside the plasma (b). Examples of the corresponding profiles are given in Fig.1b and Fig.1d respectively. Colors of the curves correspond to different pedestal widths w: 0.01 (green), 0.02 (blue), and 0.04 (red). The thick line shows $n = \infty$ ballooning mode stability boundaries. Dashed line – bootstrap current density, dotted line – localized peeling mode stability boundary

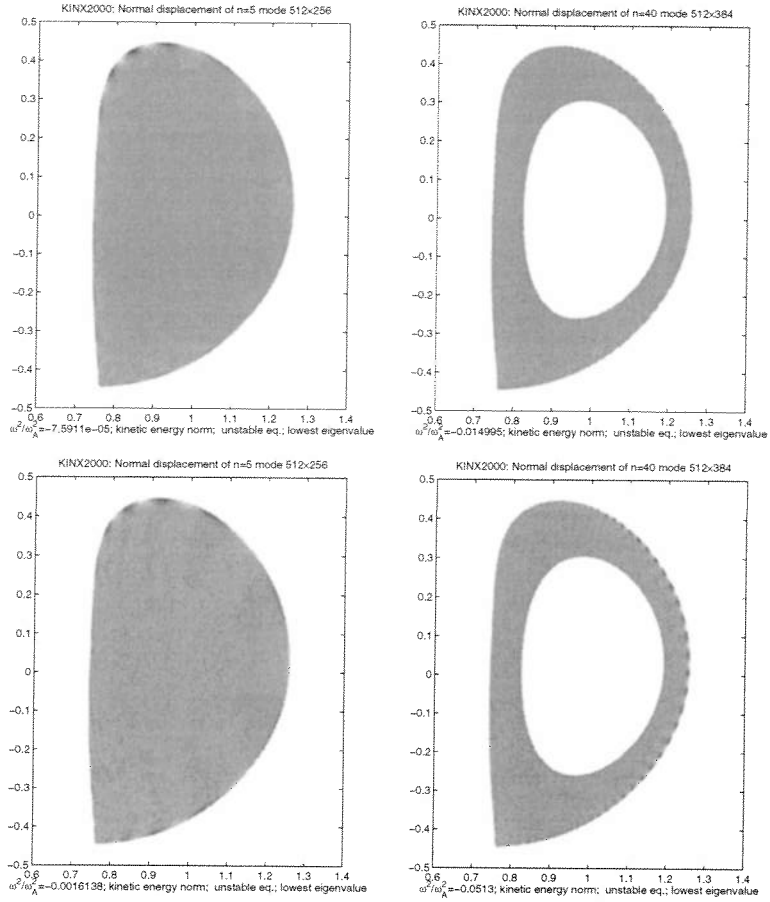

Fig.3 Filled contour plot (lighter color corresponds to maximal values) of normal displacement for the equilibria with current density pedestal at the edge (current driven modes, $J = 0.5$, upper row) and both current density and pressure gradient pedestals (kink/ballooning modes, $P' = 2, J = 0.5$, lower row). Pedestals at the separatrix ($x_0 = 1$). Toroidal wave numbers: $n = 5$ (left column) and $n = 40$ (right column)

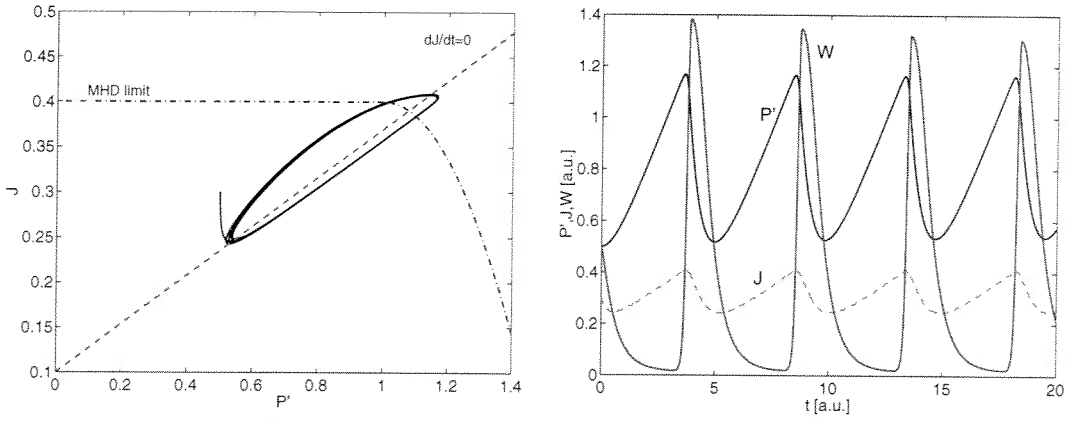

a) b)

Fig.4 Trajectory in (P', J) space (a) and time behaviour of the pressure and current pedestals together with the mode amplitude W (b) for a typical marginal stability boundary $J_{crit}(P')$ from Fig.2 shown by the dash-dotted line.

A Comparison of Weakly and Fully Relativistic Electron Cyclotron Wave Damping in the Presence of High Energy Electrons

E. Nelson-Melby, S. Alberti, T. Goodman, M. Henderson, and P. Nikkola

Centre de Recherches en Physique des Plasmas (CRPP), Association EURATOM-Confédération Suisse, EPFL, 1015 Lausanne, Switzerland

Introduction

In order to properly describe the physics of electron cyclotron resonance heating (ECRH) and current drive (ECCD), it is essential to include relativistic effects, especially when the wave propagation is nearly perpendicular to the magnetic field. Trubnikov [1] solved the fully relativistic, linearized, Fourier-transformed Vlasov-Maxwell system of equations which allowed him to express the dielectric tensor elements in two forms, the second of which has been the basis of a widely used approximation [2; 3]. This formulation (referred to in this paper as weakly relativistic) relies on an expansion in several small parameters, two of which are the electron temperature normalized to the electron rest mass (i.e. large $\mu = m_e c^2/T_e$), and the electron Larmor radius normalized to the wavelength (i.e. small $\lambda = (n_\perp \omega/\Omega_{ce})^2/\mu$). Thus for a given $n_\perp$, the approximation becomes worse for larger frequencies (higher harmonics) and higher temperature.

Recent papers by Swanson [4] and Melrose [5] have cast doubt on the accuracy of the weakly relativistic dielectric tensor. There was a fairly simple fully relativistic formulation derived in 1985 by Weiss [6] which seems to have been overlooked since then in the literature. His solution of the Vlasov-Maxwell equations resulted in a double integral but with no infinite sums over harmonics (all orders λ are also automatically included). Recently, Swanson [4], starting from Trubnikov's first form and using the Newberger sum rule to eliminate the infinite sums arrived at a form exactly equivalent to Weiss'. In Ref. [4], Swanson also introduces an expression for the dielectric tensor elements that he calls "moderately relativistic". However, these are in fact identical to the weakly relativistic expressions mentioned above [2; 3].

The results in this paper are based on a code developed using Weiss' dielectric tensor elements (correcting the sign error in the off-axis tensor elements $\sigma_{+\parallel}$ and $\sigma_{-\parallel}$), and his suggested numerical integration method (Gauss-Legendre and Gauss-Laguerre quadrature). The dispersion relation is solved for complex $n_\perp$ given real $n_\parallel$ and ω, using Muller's algorithm for finding complex roots of an analytic function.

X3 absorption on X2 pre-heated plasmas

The TCV tokamak at the CRPP has two sets of gyrotrons for auxilliary heating. One set at 82.7 GHz, which for a typical toroidal field of 1.45 T heats electrons at the 2nd harmonic X-mode (X2) near the center of the plasma. The other set is at a frequency of 118 GHz, which for the same field heats electrons at the 3rd harmonic (X3) near the center. A series of experiments was carried out on TCV for studying X3 absorption in the presence of X2

ECH/ECCD [7–9]. Normally, the X3 launched from the low-field side has a low absorption coefficient, but in the presence of X2 with an optimal co-ECCD launch angle the X3 absorption was measured to be 100% [7]. This is much higher than that expected from a single pass on a simple Maxwellian distribution function based on the measured density and temperature profiles (from Thomson scattering), which is approximately 34–46%. Studies of multiple pass absorption show that this mechanism could account for at most 5–10% of plasma heating. In Refs. [7–9] the interpretation is that there exists a high energy electron component driven by the X2 ECCD on which a large part of the X3 power is absorbed. This is also supported by evidence from high-field side ECE measurements [9] and hard X-ray measurements [8].
Recently, these type of X2+X3 heated plasmas have been modeled using a bounce-averaged Fokker-Planck code (CQL3D) [10]. The result is usually a distribution function which looks somewhat like a superposition of two Maxwellians, one representing most of the electron density in a 2–4 keV bulk, and the other a high energy superthermal tail (typically 10 to 20 keV). However, it is also anisotropic in the perpendicular and parallel (to the magnetic field) directions, and the parallel "temperature" is not the same in the co- and counter-current directions. The results from a simulation of a plasma discharge in which there was 100% measured X3 absorption (TCV shot 19285), is shown in Fig. 1, along with an approximate fit to the distribution function using a bi-Maxwellian (with bulk temperature T_b and density n_b, superthermal temperature T_s and density n_s). The 2-D distribution function is integrated in the parallel direction

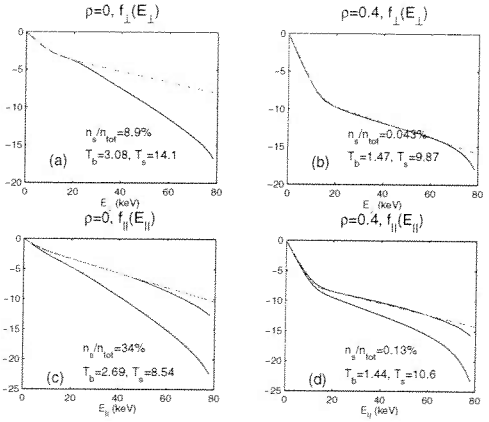

Figure 1: CQL3D results (solid lines) and fits (dashed) to bi-Maxwellian distribution functions (quantity plotted is $\ln f/f(0)$). The parallel distribution functions have two solid lines representing the larger co-current side ($p_{||} < 0$) and the smaller counter-current side.

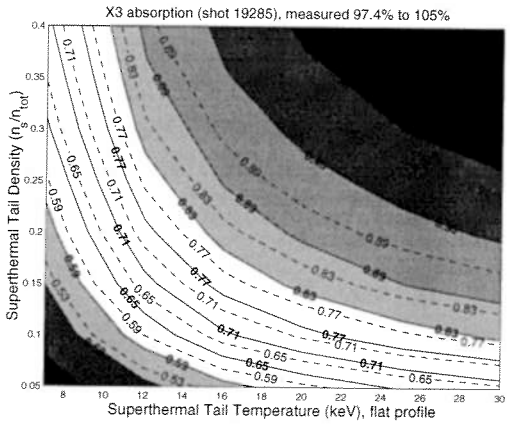

Figure 2: X3 power absorption as a function of superthermal tail and density. Solid lines are from fully relativistic calculation, dashed from weakly relativistic.

to obtain $f_\perp(p_\perp)$ and in the perpendicular direction to obtain $f_\parallel(p_\parallel)$, and these are plotted as a function of perpendicular or parallel energy at two different locations in the plasma, the center of the plasma ($\rho = 0$) in Fig. 1(a) and (c), and just outside the region where there is a significant superthermal component ($\rho = 0.4$) in Fig. 1(b) and (d). The predicted absorption from CQL3D (using a radial diffusion coefficient of 0.25 m^2/s) is approximately 60%, but numerical convergence issues remain, which could result in higher absorption using a finer mesh [11]. Using an isotropic bi-Maxwellian modeled on the co-current parallel temperature and density (or the perpendicular temperature and density) for the superthermal electrons, Im $n_\perp$ (X-mode) is calculated using the fully relativistic dispersion relation. The power absorption is then calculated by integrating the imaginary part across the plasma: $P(x)_{abs}/P_0 = 1 - \exp(-\int^x 2k_{im}\, ds)$. The resulting absorption of 51% using the perpendicular temperature or 69% using the parallel temperature brackets the CQL3D result. (The corresponding weakly relativistic results are 50% and 67%). A possible explanation for the failure to predict the measured 100% absorption is that the superthermal tail density and/or temperature are actually higher than that predicted by CQL3D. In order to see what sort of superthermal population would be necessary to have 100% X3 absorption, the absorption coefficient was calculated with a variety of superthermal density fractions (kept at a constant fraction of the total measured electron density) and temperatures (assumed constant throughout the plasma). A contour plot of the X3 power absorption fraction is shown in Fig. 2, where the solid lines are the fully relativistic result, and the dashed lines are the result of using the weakly relativistic dielectric tensor elements from Ref. [3], retaining terms up to 8th order in the finite Larmor radius expansion. It can be seen that to approach the lower bound of the experimentally measured absorption of 97%, the superthermal tail density and temperature must be on the order of 25–35% of the total density and 16–30 keV. The CQL3D simulations presented in Ref. [11] were limited to a single harmonic of interaction for each frequency of interest (only the 3rd harmonic for 118 GHz and only the 2nd harmonic for 82.7 GHz). However, when there is a significant high energy electron component, there can be a fair amount of wave damping before reaching the desired harmonic due to the relativistically down-shifted next higher harmonic. An example of how the X2 ECCD is affected for three different superthermal tail components is shown in Fig. 3. Note that for the largest tail presented, about 70% of the power is absorbed before even reaching the Doppler-shifted 2nd harmonic resonance (the weakly relativistic calculation only predicts 60%). This low-field side power absorption on the down-shifted 3rd harmonic of 82.7 GHz actually produces counter current drive, thus driving down the overall ECCD efficiency. Also, superthermal tail electrons in this region can affect the X3 (118 GHz) power absorption. Figure 4 shows the particular case of a superthermal component that is 20% of the total density and 25 keV (flat temperature profile). Nearly 30% of the power is absorbed on the down-shifted 4th harmonic resonance (of 118 GHz) before reaching the 3rd harmonic. The combination of 3 separate TORAY-GA (a cold plasma ray-tracing code with fully relativistic damping calculations) is in quite close agreement with the full solution of the dispersion relation.

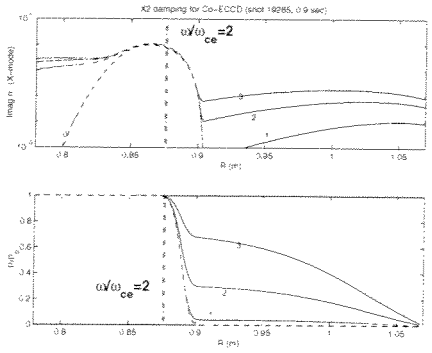

Figure 3: X2 ECCD ($n_{\parallel} = -0.26$ at $\omega = 2\omega_{ce}$) in the presence of a superthermal electron tail. Solid lines are for fully relativistic calculation, dashed for weakly relativistic. Tail density and temperature: 0) no tail 1) 10% and 15 keV 2) 15% and 22.5 keV 3) 20% and 30 keV

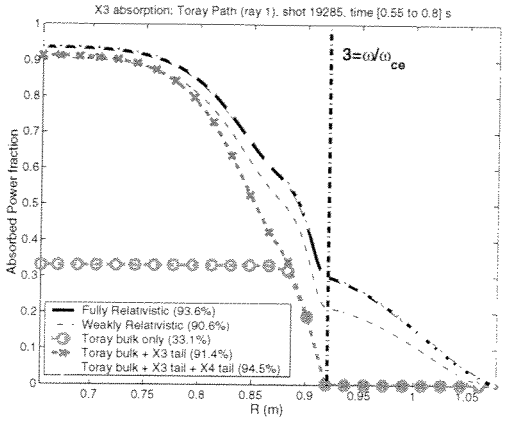

Figure 4: X3 power absorption as a function of major radius for a beam entering from the low-field side. The solid line is from the fully relativistic calculation, the thin dot-dash line is from the weakly relativistic calculation, and the symbols are from multiple TORAY-GA runs.

Conclusions When high energy electrons (> 10 keV) are present in the plasma, it is important to use the fully relativistic formulation for damping, and to include all relevant harmonics.

Acknowledgements This work supported in part by the Swiss National Science Foundation.

References

[1] B. A. Trubnikov, *Plasma Physics and the Problem of Controlled Thermonuclear Reactions*, volume III, Pergamon, London, 1959.

[2] I. Shkarofsky, J. Plasma Physics **35**, 319 (1986).

[3] V. Krivenski and A. Orefice, J. Plasma Physics **30**, 125 (1983).

[4] D. G. Swanson, Plasma Phys. Control. Fusion **44**, 1329 (2002).

[5] D. B. Melrose, J. Plasma Physics **57**, 479 (1997).

[6] I. Weiss, J. Comput. Phys. **61**, 403 (1985).

[7] A. Manini, J.-M. Moret, S. Alberti, T. Goodman, and M. Henderson, Plasma Phys. Control. Fusion (2001).

[8] S. Alberti et al., Nucl. Fusion **42**, 42 (2002).

[9] P. Blanchard et al., Plasma Phys. Control. Fusion **44**, 2231 (2002).

[10] R. W. Harvey and M. G. McCoy, The CQL3D Fokker-Planck code, in *Proc. IAEA TCM/Advances in Simulation and Modeling in Thermonuclear Plasmas*, Montreal, 1992.

[11] P. Nikkola et al., Fokker-Planck simulations of X3 EC wave absorption experiments in the TCV tokamak (paper C-54), in *15th Topical Conference Radio Frequency Power in Plasmas*, 2003.

Retarding Field Analyser Measurements in the JET Plasma Boundary

R. A. Pitts, I. Duran[1], S. K. Erents[2], J. Horacek, G. F. Matthews[2] and the JET-EFDA contributors[3)]

Centre de Recherches en Physique des Plasmas
Association EURATOM - Confédération Suisse
École Polytechnique Fédérale de Lausanne, CH-1015 Lausanne, Switzerland
[1]*Institute of Plasma Physics, Association EURATOM/IPP.CR, Praha 182 21, Czech Republic*
[2]*Euratom/UKAEA Fusion Association, Culham Science Centre, OX14 3DB Abingdon, UK*
[3)]*See annex to J. Pamela, Fus. Energy 2002 (Proc. 19th Int. Conf. Lyon, 2002), IAEA, Vienna*

INTRODUCTION

Ion temperatures, T_i, and velocity distributions, f(v), in the plasma edge of fusion devices are notoriously difficult to measure and thus rarely available but yet are important plasma boundary quantities. Though requiring the insertion of a material probe into the scrape-off layer (SOL), the Retarding Field Analyser (RFA) is one experimental approach that can access the plasma ion or electron velocity distribution directly. By designing a "bi-directional" probe, ie. one which can intercept particles on both sides of a plane oriented perpendicular to the total field line direction at a particular location in the SOL, the device may also be used to simultaneously characterise any net flow that may be present there. In fact, according to recent theoretical work [1], it turns out that the presence of an external flow field should have a strong influence on the parallel field ion velocity distributions (and hence on the derived ion temperatures) at the upstream and downstream locations of any surfaces inserted into the flow. This contribution will offer the first experimental evidence for this effect, describing recent results obtained with an RFA in the JET plasma boundary.

RFA PRINCIPLE AND THE JET RFA

Figure 1a) illustrates the well known [2,3] basic principle of RFA operation. Charged particles are transmitted through a small aperture (width ~ λ_D, the Debye Length) and are analysed by retardation in the electric field established through bias potentials applied to a number of grids. Since the electron velocity distribution (and hence the electron temperature, T_e) can to some extent be measured by the simple single Langmuir probe, the primary focus of RFA application is often the ion velocity distribution. An appropriate electrode bias configuration for ion analysis is included in Fig. 1a), illustrating how the slit plate is normally negatively biased to repel all but the highest energy electrons. A positive voltage sweep, V_1, is applied to Grid 1 and a constant negative bias on Grid 2 at a value lower than that applied to the slit eliminates any remaining electrons. The collector at zero volts

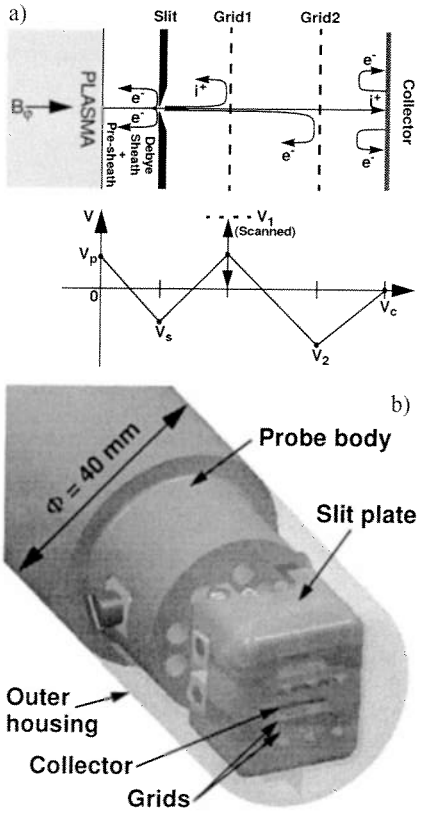

Figure 1: a) Illustrating the RFA principle and bias potential arrangement for ion analysis and b) showing the engineering and assembly of the JET RFA probe head.

suppresses any ion induced secondary electrons. In tokamaks, the current-voltage characteristic thus obtained is often experimentally found to be closely consistent with that which would arise if the parallel ion velocity distribution were a Maxwellian shifted in velocity space by an amount equal to that gained by acceleration in the sheath and pre-sheath electric fields [2,3]. In this case, for values of V_l exceeding the voltage required to back-off this energy shift, the I-V characteristic can be written in the form: $I_c = I_i \exp(-Z_i V_l / T_i)$ where $I_i = AZ_i T_i e^2/m_i$, Z_i is the ion charge and T_i (in eV) is the ion temperature of the distribution.

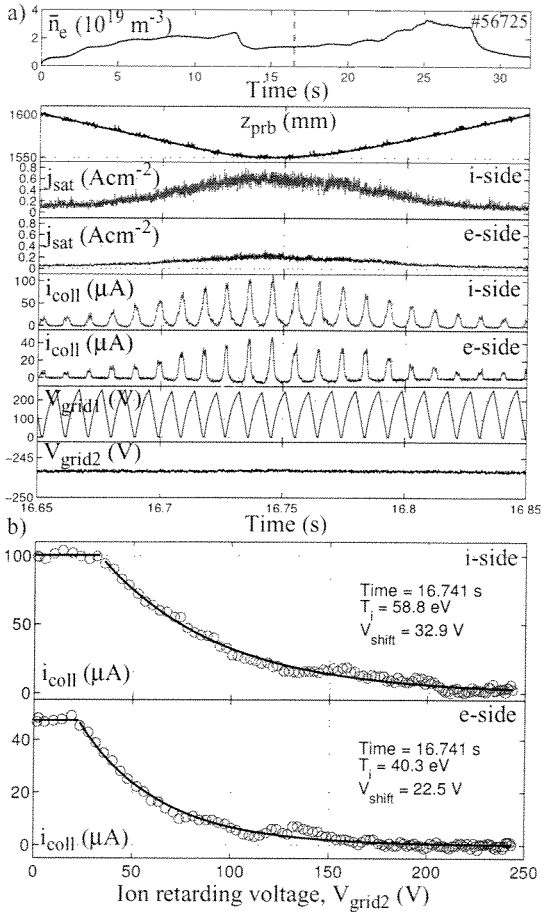

***Figure 2**: a) Time sequence of RFA data for a single reciprocation into a low density, ohmic discharge. b) example RFA characteristics and their fits for a single time in a). Red: ion-side, blue: electron-side*

A new RFA has recently been designed and successfully operated at JET using the fast reciprocating drive systems to insert the probe head several times into the edge plasma, whilst simultaneously employing a second probe to measure radial profiles of particle flux and T_e for comparison with data from the RFA. The new probe head is illustrated in the form of a false colour solid model illustration in Figure 1b). An extensive report on the technical design, construction and performance has recently been completed [4].

RESULTS - SOL FLOW AND T_i

An example of the kind of data produced by the diagnostic is given in Fig. 2, from the ohmic phase of a low density, single null lower diverted equilibrium with I_p = 2.0 MA and B_φ = 2.4 T, both in the forward, or clockwise direction. In what follows, only data from this single JET discharge, #56796, will be considered. The probe is inserted at a point on the upper, low-field-side of the poloidal cross-section and is designed such that the aperture slits (40 μm wide, 3.0 mm length) are aligned closely perpendicular to the total magnetic field direction at this point. For forward I_p, B_φ, the slit facing the ion drift direction (the ion, or i-side) intersects field lines spiralling upwards from the outer divertor whilst the electron, or e-side, slit faces the inner divertor. Figure 2b) demonstrates that under certain conditions the RFA ion characteristics are clearly consistent with a shifted Maxwellian velocity distribution, though the magnitude of the shift in this case is not that of the true sheath potential fall since bias potentials and currents are measured with respect to the torus potential and not the local slit floating potential, V_f. The shift, V_{shift}, can be appropriately corrected by floating the RFA slits and directly measuring V_f, but at the price of losing the simultaneous measurement of j_{sat} (Fig. 2a)), the ion saturation current density to the plates (by applying a large negative bias, typically -150 V).

It is already clear in Fig. 2a) that the i-side/e-side j_{sat} ratio considerably exceeds unity and thus that the RFA is immersed in a flowing SOL plasma. Such strong flow is regularly observed on JET for forward B_φ [5] and is usually estimated by employing a fit to the fluid model of Hutchinson [1,6]: $M = 0.4 \ln(j^u_{sat}/j^d_{sat})$ where M is the flow Mach No. (normalised to the isothermal sound speed , $c_s = (e(T_e + Z_i T_i)/m_i)^{1/2}$ (T_i, T_e in eV) and the superscripts u, d denote "upstream" and "downstream" with respect to the flow. The latter is defined as positive if it is directed towards the probe so that the i-side in Fig. 2a) is the upstream side and the flow is directed along the total field from outer to inner divertor targets. The example RFA characteristics in Fig. 2b) already show that in addition to the j_{sat} asymmetry, ratio $T^i_i/T^e_i > 1$, where the superscripts i, e, now denote i-side and e-side.

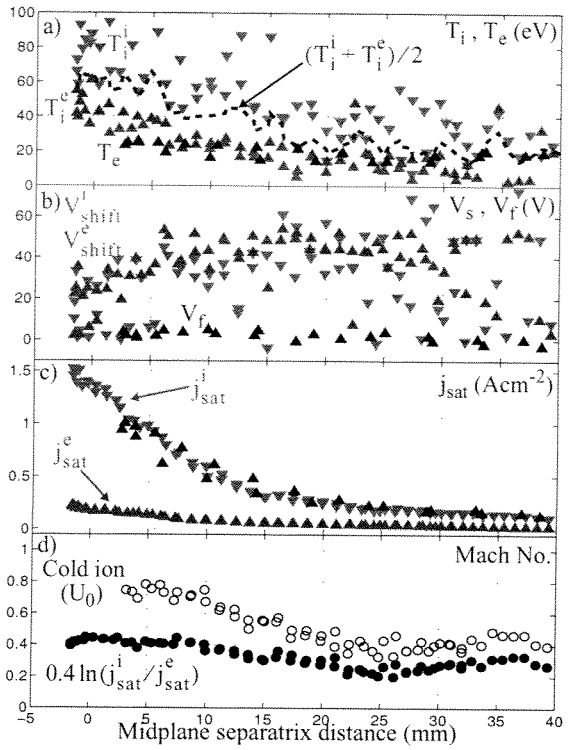

***Figure 3**: Analysis of data in Fig. 2: a) T_i, T_e and mean value of i,e-sides, b) RFA char. voltage shifts, c) slit current densities and d) measured flow Mach No. with cold ion correction: $U_0 = M(1 + \tau)^{1/2}$ (JET discharge #56725)*

A complete analysis of M, T^i_i, T^e_i for the probe reciprocation of Fig. 2 is compiled in Fig. 3, along with data (black triangles) from a second reciprocating probe head which was inserted at approximately the same time in the discharge at the same poloidal location (but at a different toroidal position) and from which a scanned Langmuir probe provides data for j_{sat}, T_e and V_f on the upstream side only. Unfortunately, there is a good deal of uncertainty with regard to absolute probe positions with respect to the separatrix, due both to errors in knowledge of the absolute probe location in space and in the equilibrium reconstruction. In Fig. 3, separatrix distances have been estimated by first using electron pressure balance between outer divertor target Langmuir probe measurements (whose positions are known rather accurately) and those obtained upstream and then by radially shifting the RFA i-side j_{sat} profile (Fig. 3b)) until the profile shapes are in reasonable agreement. The use of pressure balance in this case is particularly appropriate in view of the low density, ohmic conditions which provide a reasonably simple SOL with weak parallel temperature gradients and a low recycling divertor. At the strike points, $T_e \sim 20$ eV, $n_e \sim 3 \times 10^{19} m^{-3}$ at both the inner and outer divertors and both divertor plasmas are well attached. A further multiplicative factor of ~2 is also generally required on the RFA j_{sat} to match absolute magnitudes. The origin of this is not understood, but may be due to reduction in current when ions are lost to the side walls of the chamfered edges in the probe end cap bordering the entrance aperture plates.

Although the RFA data are rather scattered, Fig. 3 illustrates that $T^i_i > T^e_i$, $(T^i_i + T^e_i)/2 > T_e$ and $M > 0$ throughout most of the profile (the smoothed, mean ion/electron-side T_i is plotted as the dashed line in Fig. 3a)). Error bars have been omitted for clarity, but are generally of order 5% when RFA collector currents are high, becoming more significant at lower currents (and hence further out in the SOL in the case of Fig. 3a)). Concerning the general observation that $T_i > T_e$, this is qualitatively expected in the low density SOL in which these measurements have been obtained. The SOL collisionality parameter, $\nu^*_{SOL} = L_e/\lambda_{ii} \approx 10^{-16} n_e L_c/T^2_i \sim 1$

(L_c is the probe to target connection length of ~ 40 m) on a flux surface at the point of closest approach to the separatrix in Fig. 3 and so the temperature equilibration time is very much longer than the effective SOL energy confinement time.

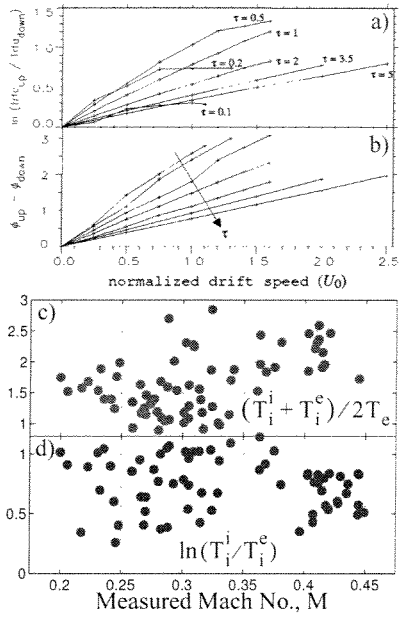

***Figure 4**: a,b) Extracted from ref. [1], Fig. 7 c) observed variation of τ with M and b) measured $ln(T_i^i/T_i^e)$ vs. M*

Regarding the strong i-side, e-side T_i asymmetry, the data would appear to be the first qualitative experimental demonstration of the recent theoretical assertion [1] that such an effect should be observed by an RFA immersed in a strong plasma flow. This is due to the perturbing effect of the probe itself which depletes ions preferentially on the downstream side, generating strong electric fields and modifying the ion velocity distribution. According to this theory, the real T_i in the plasma cannot be measured by a single-sided RFA in a flowing plasma, but is given rather accurately by the mean value of i-side to e-side values provided the drift is not too strong. Figure 4a), extracted from ref. [1], plots the expected ratio of $\ln(T_i^i/T_i^e)$ as a function of normalised, cold ion plasma drift speed, U_0, for varying $\tau = T_i/T_e$. As shown in Fig. 3d), U_0 is related to the measured M by the multiplying factor $\sqrt{1+\tau}$. In the theory, for values of t relevant to the tokamak edge (ie $\tau > 1$), the ratio T_i^i/T_i^e increases with U_0 and decreases with τ. In Fig. 4d), the measured quantity $\ln(T_i^i/T_i^e)$ is plotted against the measured flow speed, whilst Fig. 4c) gives the measured τ for reference. At the flow maximum (corresponding to the position of maximum insertion for this discharge), $\tau \sim 2.5$, $M \sim 4$, $U_0 \sim 0.8$ and the RFA yields $\ln(T_i^i/T_i^e) \sim 0.5$-$0.8$. This should be compared with the expected value, read crudely from the curve in Fig. 4a) of $\ln(T_i^i/T_i^e) \sim 0.4$. Experimentally, deeper in the SOL, where U_0 decreases, τ also decreases and the T_i ratio is approximately constant, though the data are very scattered. Such behaviour is also qualitatively consistent with the theory, though absolute magnitudes do not agree. The theory also predicts a reasonably strong variation of the expected upstream-downstream pre-sheath potential difference (Fig. 4b)). This is more difficult to assess experimentally from the noisy RFA data, which itself must be corrected for the (unmeasured) local value of V_f. For the measured values of M and τ near the separatrix in Fig. 3, the expected theoretical difference would be $\sim T_e$ volts favouring the upstream (i-side) and as such should be observable. This does not appear to be the case for the V_{shift} data in Fig. 3b).

ACKNOWLEDGMENTS

This work was performed under the European Fusion Development Agreement and was supported in part by the Swiss National Science Foundation, EURATOM and the UK Department of Trade and Industry.

REFERENCES

[1] F. Valsaque, G. Manfredi, J. P. Gunn and E. Gauthier, Phys. Plasmas **9** (2002) 1806
[2] G. F. Matthews, J. Phys. D: Appl. Phys. **17** (1984) 2243
[3] R. A. Pitts, Phys. Fluids **B3**, (1991) 2873
[4] R. A. Pitts et al., submitted to Rev. Sci. Instrum. (June 2003)
[5] S. K. Erents et al., Plasma Phys. Control. Fusion **42** (2000) 905
[6] K-S. Chung and I. H. Hutchinson, Phys. Rev. A **38** (1988) 4721

First experimental results from the new toroidal device TORPEX

M.Podestà, A.Fasoli, B.Labit, M.McGrath, S.Mueller, F.M.Poli And the CRPP team

CRPP-EPFL, Association EURATOM-Confédération Suisse, Lausanne, Switzerland

1. Introduction

A new TORoidal Plasma Experiment (TORPEX) has been built at CRPP, mainly dedicated to the study of turbulence and anomalous transport in toroidal plasmas. Low densities and temperatures make it possible to measure and possibly control plasma parameters and wave fields with high resolution locally throughout the plasma. The first experimental campaign is aimed at establishing the relationship between the gradients and the fluctuation spectra, measured by electrostatic probes. Both coherent modes and broad spectral features are observed in the different plasma configurations, depending on plasma profiles.

2. Experimental set-up

TORPEX is a toroidal device with major and minor radius R=1m and a=0.2m (Fig.1). A set of 28 coils provides a toroidal magnetic field up to 0.1T. Six poloidal coils can be used to add a small vertical component $B_v \leq 50$mT for the optimisation of the plasma production scheme, or to produce a magnetic cusp configuration, relevant for studies of magnetic reconnection phenomena. In addition, an ohmic transformer will induce a plasma current closing the magnetic surfaces and creating a rotational transform.

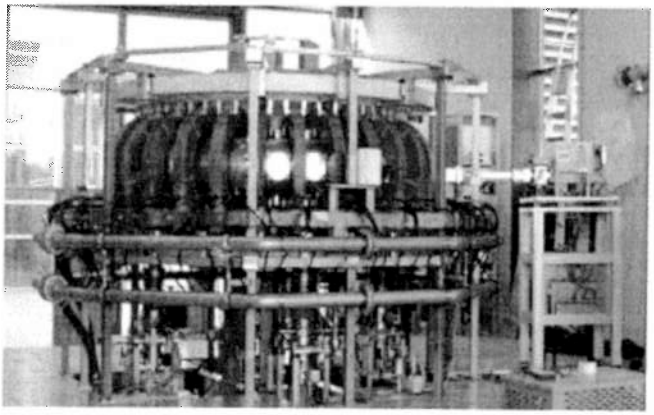

Fig.1 – The TORPEX device

Well reproducible plasmas of Argon and other noble gases, for pressures $p_{gas} \sim 10^{-4}$-10^{-5}mbar, are produced by means of waves in the electron cyclotron (EC) range of frequencies; plasma density and electron temperature are in the range $n_e \sim 10^{16}$-10^{17}m^{-3} and $T_e \sim$5-10eV, with up to 50kW of microwave power at f=2.45GHz injected during 100ms from the low-field side. Parameters as the neutral gas pressure, the location of the EC resonance and the amount of injected power can be varied to control density and electron temperature profiles.

A reconstruction of the profiles of the main plasma parameters over the poloidal section is obtained using movable electrical probes and analysers. The fluctuation spectra are measured

using 33 pairs of capacitively coupled fixed Langmuir probes [1] (1.3mm between tips, 8mm between pairs) installed at the same toroidal location and measuring the fluctuating component of the ion saturation current I^{+}_{sat}; they provide frequency spectra in the range 100Hz-125kHz, and a determination of perpendicular wave numbers $k_{\perp}$ up to 24cm^{-1}. The acquisition system includes 64 channels sampled at 1kHz, 96 at 250kHz and 16 at 10MHz.

3. Mechanism of plasma production by EC waves

TORPEX plasmas are produced by waves injected in O-mode polarisation using a

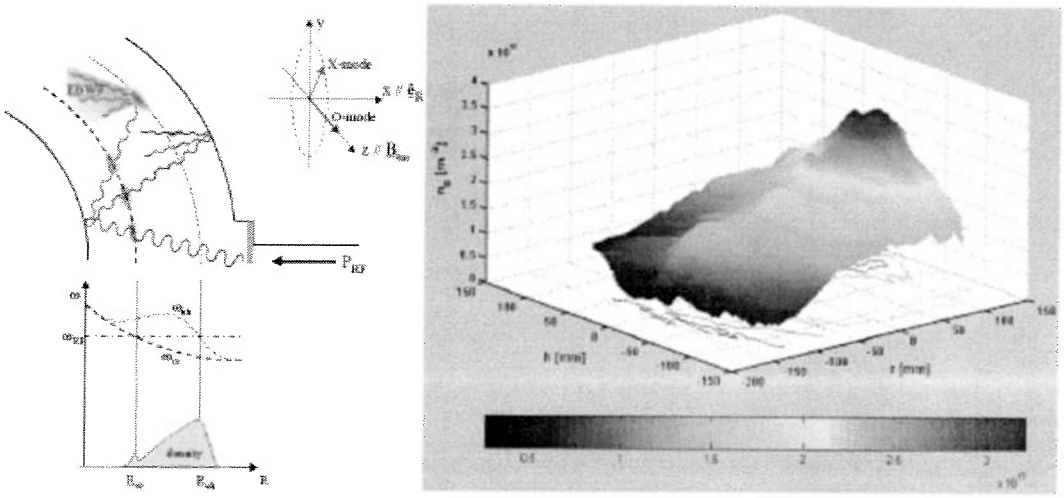

Fig.2 – Left: schematic of the propagation and absorption mechanisms. Right: a measured density profile for Argon with $p_{gas}=2{\cdot}10^{-5}$mbar, B_v=3mT, P_{RF}=10kW. Coordinates (r,h) are centered on the magnetic axis.

magnetron source at f=2.45GHz and a truncated wave guide as antenna. The EC frequency is matched at R_{ec} where B=0.0875T. Primary electrons are accelerated at R_{ec} by resonant interactions, then ionize the neutral gas by collisions. Once a plasma is created, the waves are absorbed at the upper-hybrid resonance location R_{uh} on the low-field side of R_{ec} (Fig.2), where the density profile peaks [2]. Electron temperatures of the order of 5eV are measured over the whole plasma column. For low power values ($P_{RF}\leq$10kW), the lack of dependence of T_e on the absorbed power, estimated as the difference between injected and reflected power, measured using a bidirectional coupler, suggests that T_e is determined mainly by the ionization process.

The profiles of n_e, T_e and plasma potential depend on externally controlled parameters like the vertical field B_v, p_{gas}, R_{ec} and the injected power. The influence on T_e and n_e profiles, and the relative gradient lengths L_n, L_{Te} is illustrated in Fig.3.

The vertical magnetic field is expected to reduce the particle losses by partially short-

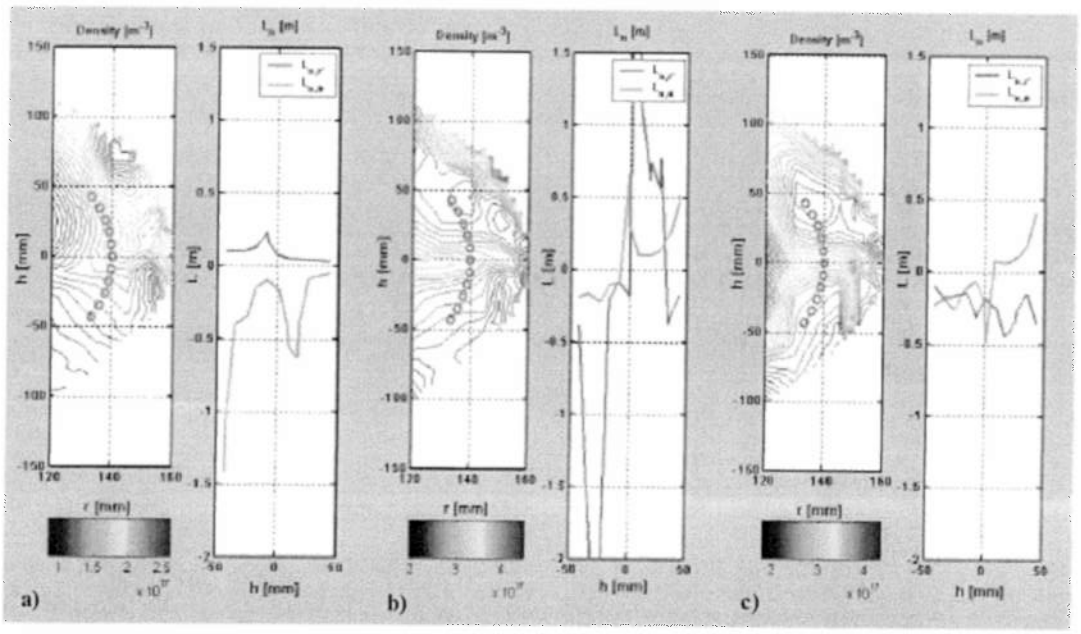

Fig.3 – Dependence of the density profile on B_v and absorbed power. Gas: Argon, $p_{gas}=2\cdot10^{-5}$ mbar. a) $B_v=0$, b) $B_v=3$mT, c) $B_v=3$mT and the absorbed power is increased. Red circles indicate the position where the gradient lengths are evaluated. r' and θ are the minor radius and poloidal angle coordinates.

circuiting the electric field generated by particle drifts [3]. The existence of an optimal value for B_v, suggested by theoretical considerations that include a balance of different loss channels, is confirmed experimentally.

4. First characterization of instabilities and turbulent phenomena

The relationship between L_n, L_{Te} and the development of instabilities and turbulent phenomena is a key issue for anomalous transport in toroidal plasmas. In the first measurement campaign both coherent modes and broad spectral features are observed in the different plasma configurations, depending on plasma profiles, although a direct link between the observed fluctuations and the profile parameters still needs to be established.

Coherent modes with $k_\perp$ values up to ~1cm^{-1} and $k_\parallel$ of the order of 0.1cm^{-1} are observed for frequencies below 60kHz. In the range 1-60kHz the phase velocity is $v_{ph}\sim10^2$-10^3m/s, in the direction of electron drift, consistent with a numerical estimation of v_{ph} for drift waves with the measured values of $k_\perp$ and $k_\parallel$. At higher frequencies (10-110kHz) the spectrum is dominated by broad-band activity with bandwidths in the 10-20kHz range, in which v_{ph} cannot be determined and $k_\perp\leq2$cm^{-1}.

Due to the asymmetry in the plasma profiles, only 'local' analyses for each probe array are meaningful, as illustrated in Fig.4, where the fluctuations of the ion saturation currents from three probe arrays show very different features.

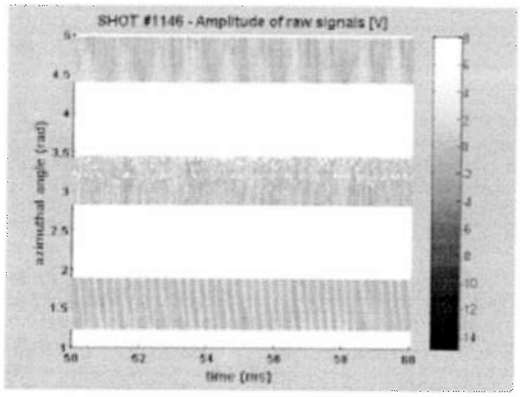

Fig.4 – Normalized fluctuations of ion saturation current from the 3 high-frequency arrays.

The statistical properties of turbulence are analysed through the study of the self-affinity parameter H (Hurst exponent) and the probability density functions (PDFs) of the raw signals [3]. PDFs measured in different plasma conditions show a strong distortion from a Gaussian shape with well pronounced tails, especially in the case of B_v=0. These tails are associated with intermittent transport phenomena that influence particle and energy losses. As an example, Fig.5 shows the PDFs from six probe tips for two discharges with and without B_v, with significantly different turbulence properties.

5. Conclusions

The new toroidal device TORPEX for basic plasma physics studies is operating routinely. Its flexibility in magnetic configuration and plasma parameters makes it possible to study with high temporal and spatial resolution turbulence and transport in toroidal plasmas. In the first experimental campaign both coherent and broad-band phenomena have been observed and characterised.

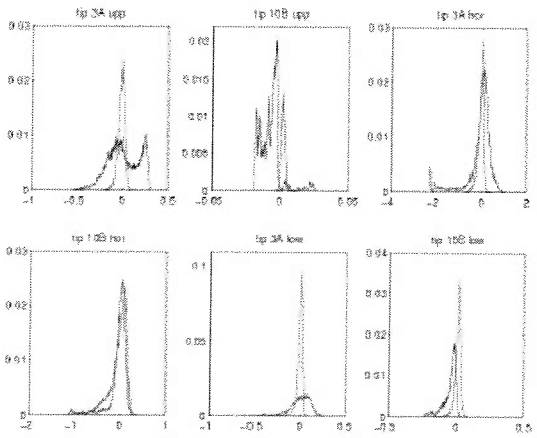

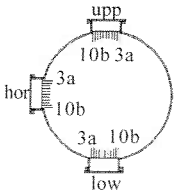

Fig.5 – PDFs for two different shots, with (green) or without (blue) vertical magnetic field

References

[1] J.M.Beall et al., J. Appl. Phys **53**, 6 (1982)
[2] K.Rypdal et al., Phys. Plasmas **4**, 5 (1997)
[3] S.Nakao et al., Phys. Lett. **96A**, 8 (1983)
[4] J.A.Krommes, Phys. Rep. **360**,1 (2002)

OPTIMIZED POLOIDAL PSEUDOSYMMETRY FOR TOROIDAL SYSTEMS

V.D. Shafranov[1], W.A. Cooper[2], M.Yu. Isaev[1], M.I. Mikhailov[1], J. Nührenberg[3], M.A. Samitov[1], A.A. Skovoroda[1], A.A. Subbotin[1], R. Zille[3]

[1] Russian Research Centre "Kurchatov Institute", Moscow, Russia

[2] Centre de Recherches en Physique des Plasmas, Association Euratom-Confédération Suisse, Ecole Polytechnique Fédérale de Lausanne, Switzerland

[3] Max-Planck-Institut für Plasmaphysik, IPP-EURATOM Association, Germany

Abstract

The numerical optimization of stellarator systems from the viewpoint of plasma equilibrium, stability and particle confinement has shown that rather good properties can be achieved in configurations having most of the B contours closed around a magnetic axis of helical form. Note that the optimized stellarator W7-X (see, e.g., Ref.[1]) belongs just to this type. The possibility to fulfill the quasi-isodynamicity condition in such type of stellarators with poloidal closed mod-B contours was analyzed in Ref. [2] for deeply to moderately trapped particles. In Ref. [3] it was shown for moderate number of periods $N = 6$, and aspect ratio per period $A_p = R/Na \sim 2$ (R, a are the major and averaged minor radii of toroidal system), that this condition can be extended to all reflected particles. It is worth to emphasize that the configurations considered have no symmetric analogue even for a large number of periods and high aspect ratio. Thus, the confinement properties of such kind of stellarators for large number of periods should be investigated step by step. In the present report, some results are presented for a nine-period system.

Introduction

In the present paper, the stellarator configurations with mod-B = constant lines in the poloidal direction on the magnetic surfaces are considered. For such type of magnetic configurations, the improvement of the reflected particle confinement can be achieved by optimization of the contours of the second adiabatic invariant, $\mathcal{J} = \int v_{\|} dl = \mathcal{J}(s)$, to be constant on magnetic surfaces through the poloidal closure of these contours (s is normalized toroidal flux; s=1 on the boundary). In Ref. [2], where this condition was named quasi-isodynamicity, the possibility was shown to satisfy it for deeply to moderately deeply trapped particles. In Ref. [3] it was demonstrated by numerical optimization that this condition can be satisfied for all reflected particles. A six-period configuration found with finite $\beta \approx 5\%$ possesses good collisionless fast-particle confinement. In addition, it was shown that the requirement of good particle confinement is well compatible with local interchange-mode stability conditions.

In the configurations of the type considered, the bumpy component of the magnetic field strength is necessary to create mod-B = constant lines in the poloidal direction on the magnetic surfaces. To avoid the appearance of islands in the B = constant lines on the magnetic surfaces, the longitudinal variation of B should be larger then the poloidal variation of B connected with the curvature of the magnetic axis. In the cross-sections with magnetic field strength extrema, the toroidal variation of B is zero and cannot compensate finite poloidal variation. Thus in these cross-sections the magnetic axis curvature should be zero. Nevertheless, significant curvature of the magnetic axis is needed in most parts of the system for the creation of a vacuum magnetic well. Note

that the magnetic well can be realized in systems with poloidal closed B contours due to the helical-type structure of the magnetic axis. Thus, it is interesting to investigate the confinement properties of such kind of stellarators for large number of periods. As a step in this direction, a nine-period system is considered in the present paper. As one can expect, the secondary currents are smaller in the nine-period configuration in comparison with the previously optimized six-period system. Because of this, it becomes possible to find a configuration with an increased value of plasma pressure, $< \beta >= 10\%$.

Results of numerical optimization

The numerical optimization was performed on the supercomputers Himiko (Germany) and Prometeo (Switzerland) by using the equilibrium code VMEC [4], the code JMC [5] for transition to magnetic (Boozer) coordinates and the codes for calculation of different target functions. The direct particle drift orbit calculation was performed with the MCT code [6].

Starting configuration and choice of the target functions

The boundary magnetic surface of the earlier six-period configuration [3] with $< \beta >= 5\%$ was adapted to nine periods with a corresponding change of the aspect ratio from 12 to about 22. The transformed configuration had very small secondary currents and almost zero or even inward magnetic axis shift both for zero and high enough β, and possesses a vacuum magnetic well (except in the near-boundary region). This configuration was optimized at $< \beta >= 10\%$ by using the conditions of pseudosymmetry [7], closure of the second adiabatic invariant contours [8] and Mercier and resistive mode stability criteria.

The structure of the surfaces B = constant and particle confinement

Fig. 1 shows a 3D view of the boundary magnetic surface of the optimized $N = 9$ configuration. The color here marks the value of the magnetic field strength on the boundary. It is seen that the the lines B = constant go around the magnetic axis (see, also, Fig. 2). The structure of the surfaces B = constant is shown in Fig. 3 along with two magnetic surfaces. The reflected particles are trapped between the corresponding surfaces B = constant, i.e. inside the system period. Fig. 4 shows the contours of the second adiabatic invariants in polar representation $\sqrt{s}, \theta_B$ for a set of increasing values of $B_{reflect}$.

Fig. 1. 3D view of optimized nine-period configuration. The color defines the value of the magnetic field strength.

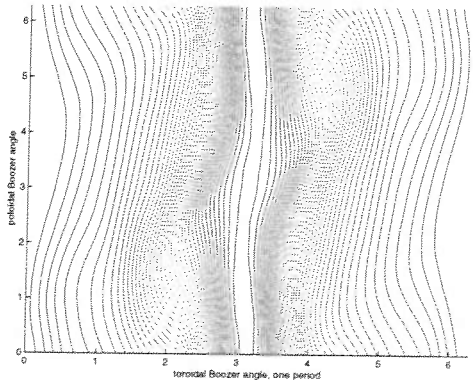

Fig. 2. Contours of B on the magnetic surface with $s = 0.25$ (one half of minor plasma radius) for the optimized configuration.

Fig. 3. The magnetic surfaces are intersected by surfaces B = constant. One system period is shown.

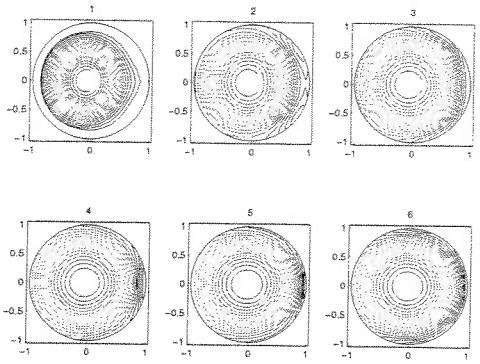

Fig. 4. Contours of the second adiabatic invariant in polar representation (normalized plasma radius $\sqrt{s}$, poloidal angle θ_B) for increased set of $B_{reflect}$

An example of projection of the trapped α-particle drift trajectory along the magnetic field lines on the surface ζ_B = constant is shown in Fig. 5. Here the color marks the value of the parallel velocity. The quality of the fast α-particle confinement was checked by direct calculation of the collisionless guiding centre orbits of 1000 particles during 1 sec and the results of these calculations are shown in Fig. 6. The following power plant-size normalization was used: $B_0 = 5$T and a plasma volume of 1000 m^3. It is seen that there is almost zero loss for particles started at 1/2 of the plasma minor radius, while about 10% of particles started at 2/3 of the plasma radius escaped from the plasma, despite the closure of most of the $\mathcal{J}$ contours.

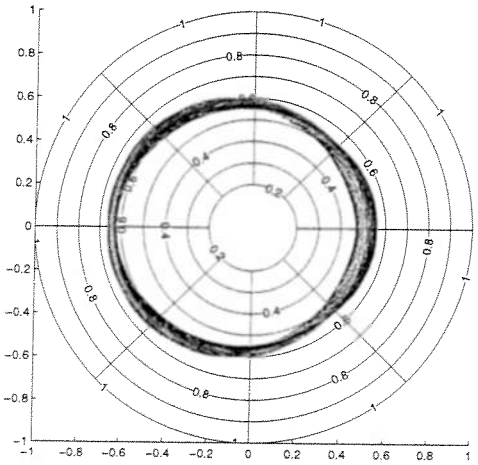

Fig. 5. The projection of α-particle collisionless guiding centre trajectory on the cross-section ζ_B = constant. The colours define the sign and the value of the parallel velocity (red corresponds to positive direction, blue means negative direction).

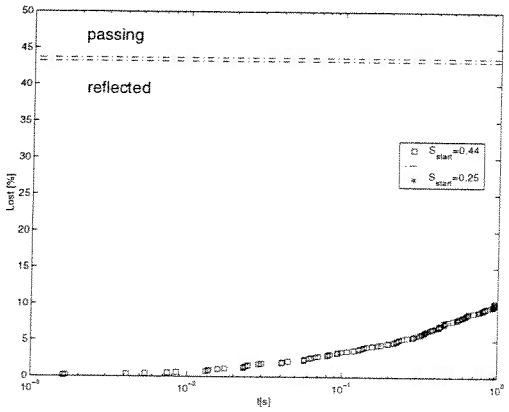

Fig. 6. Collisionless α-particle confinement in the optimized configuration as a function of the time of flight. Particles are started at s_{start} = 0.25 (red, 1/2 of the plasma radius) and at s_{start} = 0.44 (blue, 2/3 of the plasma radius); the dashed lines show the fractions of the reflected particles.

Equilibrium and stability properties of the optimized configuration

Fig. 7 shows the cross-sections of the optimized configuration in the beginning, one quarter and one half of a period and radial profiles of the rotational transform, magnetic well and plasma pressure for almost zero β (top) and $< \beta >= 10\%$ (bottom).

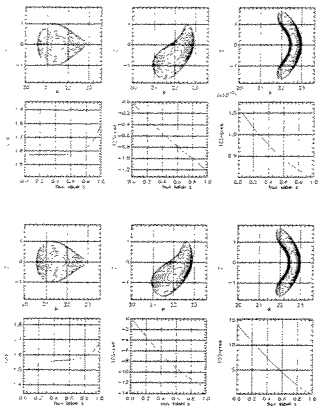

Fig. 7. Cross-sections of optimized configurations for $< \beta >= 0$ and $< \beta >= 10\%$.

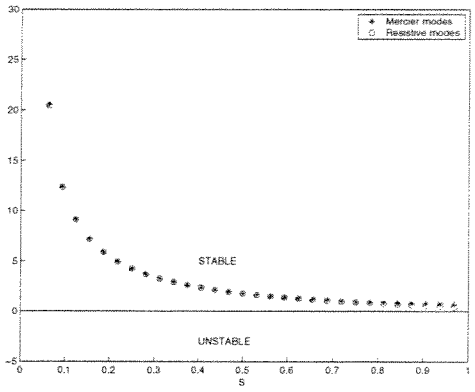

Fig. 8. Mercier and resistive mode stability of optimized configurations.

It is seen that the vacuum configuration has a magnetic well of the order of 1%. The transition from zero β to $< \beta >= 10\%$ increases the shift of the magnetic surfaces only slightly, the rotational transform profile is not changed very much, too. Fig. 8 demonstrates that Mercier and resistive modes are stable in this optimized configuration.

Conclusion. It is shown by numerical optimization for configurations with mod-B = constant lines in the poloidal direction on the magnetic surfaces that increasing the number of plasma periods and aspect ratio permits to realize good collisionless particle confinement properties and to satisfy the local interchange-mode stability criteria for a sufficiently high $< \beta >$ value. In spite of the small toroidal curvature of the magnetic axis, a vacuum magnetic well can be created due to the non-planar behavior of the magnetic axis.

Acknowledgments This work was supported by INTAS Grant No 99-00592; Russian-Germany agreement WTZ-RUS-01/581; Russian Federal program on support of leading scientific school researches, Grant No 2024.2003.2; Russian Fund for Basic Research, Grant No 03-02-16768; Fonds National Suisse de la Recherche Scientifique, Euratom; Department of atomic science and technology, Minatom RF. One of the authors (M.I.M) would like to thank Prof. K. Yamazaki for helpful discussions during his stay in NIFS, Japan.

References

[1] W.Lotz, J.Nührenberg, C.Schwab, 1991 Proc. 13th Int. Conf. on Plasma Phys. and Contr. Nucl. Fus. Res. 1990 (Washington, 1990) vol 2 (Vienna: IAEA) 603.

[2] S.Gori, W.Lotz, J.Nührenberg, Theory of Fusion Plasmas (International School of Plasma Physics), Bologna: SIF (1996) 335.

[3] M.I.Mikhailov, V.D.Shafranov, A.A.Subbotin et.al., Nuclear Fusion **42** (2002) L23.

[4] S.P.Hirshman and O.Betancourt, J. of Comput. Physics **96** (1991) 99.

[5] J.Nührenberg, R.Zille, Theory of Fusion Plasmas (Varenna 1987), Editrice Compositori, Bologna (1988) 3.

[6] R.H.Fowler, J.A.Rome, J.F.Lyon, Phys. Fluids **28** (1985) 338.

[7] M.I.Mikhailov, W.A.Cooper, M.Yu.Isaev et. al. Theory of Fusion Plasmas (International School of Plasma Physics), Bologna: SIF (1998) 185.

[8] A.A.Subbotin, M.I.Mikhailov, J.Nührenberg et.al. 28th EPS Conf. on Controlled Fusion and Plasma Physics, Funchal, Portugal, 2001 (http://www.cfn.ist.utl.pt/EPS2001/fin).

ELIMINATION OF THE BOOTSTRAP CURRENT FACTOR IN STELLARATORS WITH POLOIDALLY CLOSED CONTOURS OF THE MAGNETIC FIELD STRENGTH

A.A. Subbotin [1], W.A. Cooper [2], M.I. Mikhailov [1], J. Nührenberg [3], M.A. Samitov [1], V.D. Shafranov [1], R. Zille [3]

[1] Russian Research Centre "Kurchatov Institute", Moscow, Russia

[2] Centre de Recherches en Physique des Plasmas, Association Euratom-Confédération Suisse, Ecole Polytechnique Fédérale de Lausanne, Switzerland

[3] Max-Plank-Institut für Plasmaphysik, IPP-EURATOM Association, Germany

Abstract The value of bootstrap current in stellarator configurations depends strongly on the type of configuration. For stellarators with mod-B contours closed in the poloidal direction, one expects that bootstrap current value can be made nearly vanishing as, e.g. in W7-X. In the present paper, the effect of the behaviour of the contours of B on the magnetic surfaces on the value of the structural factor describing the bootstrap current in the long mean free path (*lmfp*) is analyzed numerically by using analytical expressions. The effect of such parameters as the number of periods and the value of $< beta >$ on the structural factor is studied. It is found that in the type of stellarators considered, it is possible to make the *lmfp* bootstrap current negligible without violation of good neoclassical confinement properties.

Introduction

The value of bootstrap current in stellarator configurations depends strongly on the topography of the surfaces B = constant. For stellarators with axial quasisymmetry, $B = B(s, \theta_B)$, where s, θ_B, ζ_B are magnetic flux coordinates, this current causes the rotational transform to increase [1]. In quasihelically symmetric stellarators [2], when $B = B(s, \theta_B - N\zeta_B)$, the bootstrap current increases the rotational transform counted relative to the direction of quasisymmetry, $\theta_B = N\zeta_B$, thus, it diminishes the tokamak-like rotational transform and can impede plasma equilibrium. For the third type of stellarators, in which the contours of B on magnetic surfaces close poloidally [3], the direction of the bootstrap current cannot be predicted a priory (see Fig. 1).

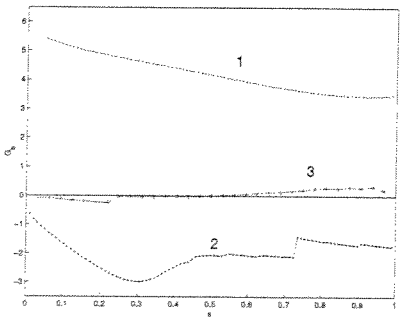

Fig. 1. Structural factor of bootstrap current for examples of tokamak (1), quasi-helically symmetric (2) and quasi-isodynamic (3) stellarator configurations.

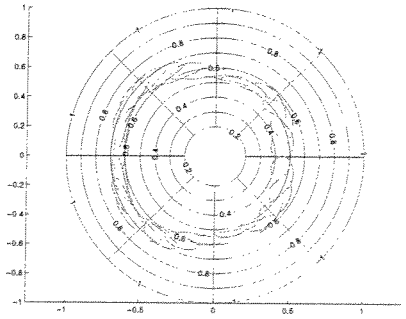

Fig. 2. Particle drift trajectory in near quasi-isodynamic configuration with B=constant lines on the magnetic surfaces in the poloidal direction.

The characteristic feature of the particle drift trajectories in near quasi-isodynamic configurations with B=constant lines in the poloidal direction on the magnetic surfaces [3] is seen from Fig. 2, where the projection of drift motion of one guiding centre on the plasma cross-section is shown. The red (blue) color corresponds to positive (negative) parallel velocity. One can conjecture that the same particle during its drift motion should contribute to the bootstrap current

with different signs on the inward and outward parts of the trajectory. Thus, by appropriate choice of the positions of points with zero banana size one can make the bootstrap current vanishing. This argument can be illustrated also by the example of a mirror type configuration with mirror symmetry, when all magnetic field lines are closed and the rotational transform is equal to zero [4]. In this case, it is forbidden to have non-zero current in cross-sections of mirror symmetry, so that the bootstrap current should be equal to zero exactly in order to conserve the mirror symmetry.

In addition, it is known that the value of bootstrap current is nearly vanishing in the optimized stellarator W7-X which is close to being quasi-isodynamic. It was shown also [5] that for a six-period stellarator optimized with respect to quasi-isodynamicity [6], the bootstrap current changes the rotational transform only slightly. In the present paper, the possibility to nullify the structural (geometric) factor G_B of the bootstrap current is analyzed numerically by using the optimization procedure based on codes for calculation of equilibrium (VMEC code [7]), transition to magnetic (Boozer) coordinates (JMC code [8]) and on calculations of the G_B-factor from analytical expressions. Some N=6 and N=9 configurations optimized with respect to quasi-isodynamicity are studied for different values of $< \beta >$. The calculations were performed on the supercomputers Himiko (Germany) and Prometeo (Switzerland).

Results of the optimization

The bootstrap current model in $1/\nu$ regime that has been used in this paper has been very compactly described in [9]. The formulas presented there have evolved from previous research on the subject [10]. The specific equations have the form:

$$< \mathbf{jB} >= G_b(L_1 \frac{dp}{d\Phi} + L_2 \frac{dT}{d\Phi}),$$

where the structural factor G_B can be expressed as:

$$G_b(s) = \frac{1}{f_t}[< g_2 > - \frac{3 < B^2 >}{4B_{max}^2} \int_0^1 d\lambda\lambda \frac{< g_4 >}{< g_1 >}],$$

$$g_1 = \sqrt{(1 - \lambda B/B_{max})}$$

$$\mathbf{B} \cdot \nabla(g_2/B^2) = \mathbf{B} \times \nabla\Phi \cdot \nabla B^{-2},$$

$$\mathbf{B} \cdot \nabla(g_4/g_1) = \mathbf{B} \times \nabla\Phi \cdot \nabla g_1^{-1},$$

$$g_2(B_{max}) = g_4(B_{max}) = 0.$$

To calculate G_B in magnetic coordinates (which are used in the optimization), one needs to know only the flux functions and the magnetic field strength B. In the present paper, the structural factor was calculated for net current free configurations, so that the effect of bootstrap current itself on the geometric factor was not taken into account. Configurations with numbers of periods $N = 6$ and $N = 9$ and $< \beta >= 10\%$ are optimized with respect to vanishing bootstrap current structural factor. The configurations obtained were investigated then for different values of $< \beta >$. It is worth to note that during the optimization only the requirement of elimination of the bootstrap current was imposed. In spite of this, the main favourable properties (collisionless particle confinement and local interchange-mode stability) were conserved.

N=6 configuration. The 3D view of the $N = 6$ configuration [6] is shown in Fig. 3. Fig. 4 shows the cross-sections of the optimized configuration and some flux functions. The history of the optimization procedure is shown in Fig. 5 (compare the scales of G_B in Fig. 1 and Fig. 5). Fig. 6 shows that the quality of closure of contours of the second adiabatic invariant $\mathcal{J} = \int V_{||} dl$ is not violated seriously during the optimization.

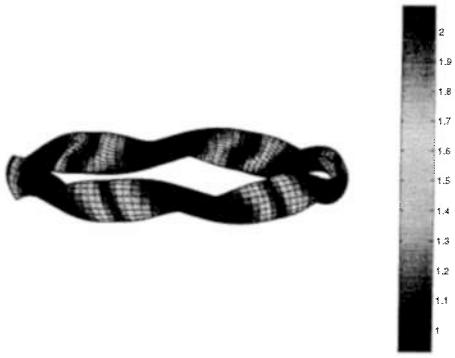

Fig. 3. $3D$ view of the $N = 6$ configuration.

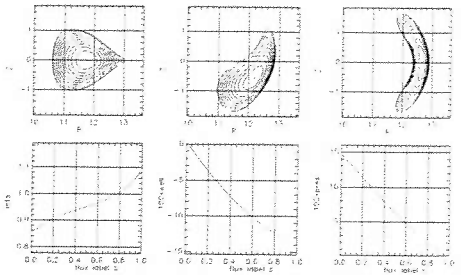

Fig. 4. Cross-sections of the $N = 6$ configuration.

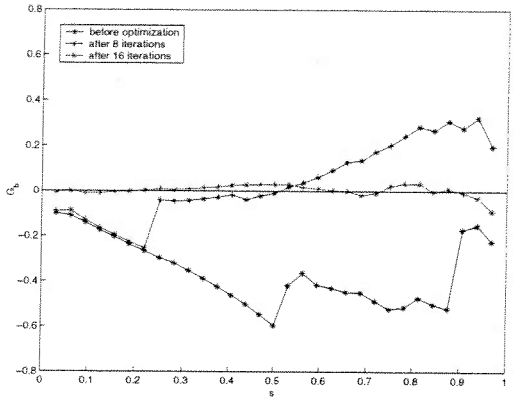

Fig. 5. Minimization of the geometric factor of the bootstrap current for the $N = 6$ configuration.

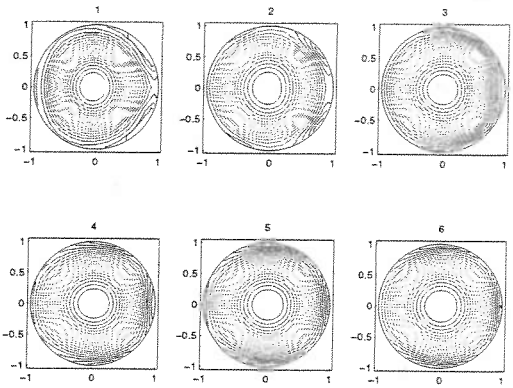

Fig. 6. Contours of the second adiabatic invariant.

N=9 configuration [11]. Fig. 7 shows the cross-sections and flux functions for the $N = 9$ configuration. The characteristic differences in comparison with the $N = 6$ system are the increased rotational transform and the negligibly small Shafranov shift for the large value of plasma pressure considered, $< \beta >= 10\%$. The value of the structural factor here is larger than that the for the $N = 6$ configuration (see Fig. 8).

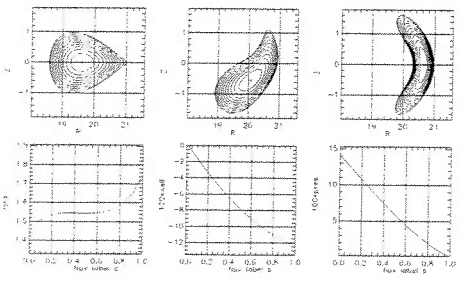

Fig. 7. Cross-sections of the optimized $N = 9$ configuration.

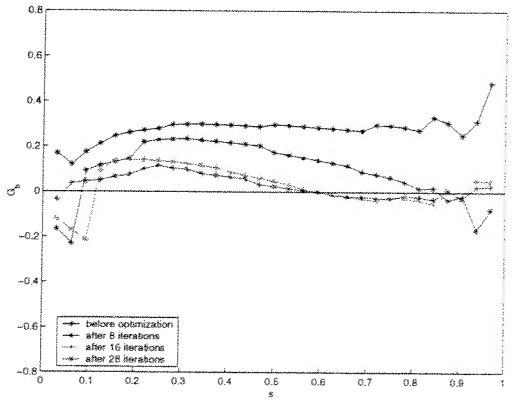

Fig. 8. Minimization of the geometric factor of the bootstrap current for the $N = 9$ configuration.

Fig. 9 shows the Mercier and resistive mode stability properties of the configurations found. Finally, in Fig. 10, the dependencies of maximum $|G_B|$ on $< \beta >$ for boundaries optimized at $< \beta >= 10\%$ are shown.

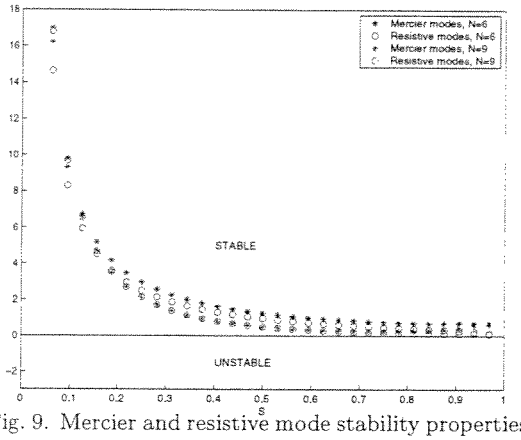

Fig. 9. Mercier and resistive mode stability properties for the configurations considered.

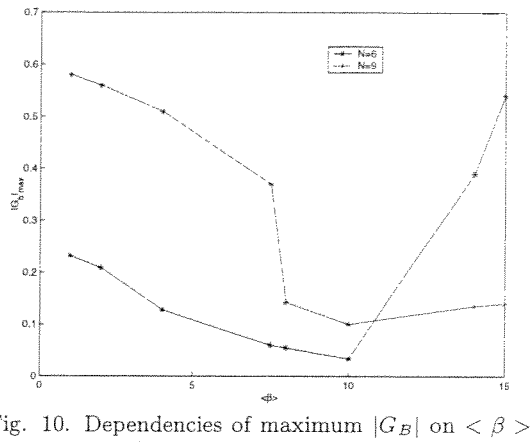

Fig. 10. Dependencies of maximum $|G_B|$ on $< \beta >$ for $< \beta >= 10\%$ optimized configurations.

Conclusions

It is shown by numerical optimization that in near quasi-isodynamic configurations with B=constant lines on the magnetic surfaces in the poloidal direction, the bootstrap current can be eliminated with high accuracy.

The requirement of vanishing of the bootstrap current is not in contradiction with the conditions of improved collisionless particle confinement and local mode stability.

Acknowledgments This work was supported by INTAS Grant No 99-00592; by the Russian-Germany agreement WTZ-RUS-01/581; by Russian Federal program on support of leading scientific school researches, Grant No 2024.2003.2; by the Russian Fund for Basic Research, Grant No 03-02-16768,; by the Fonds National Suisse de la Recherche Scientifique, Euratom; by Department of atomic science and technology, Minatom RF. One of the authors (M.I.M) would like to thank Prof. K. Yamazaki for helpful discussions during his stay in NIFS, Japan.

References

[1] M.C. Zarnstorff et. al. Plasma Phys. and Controlled Fusion **43** A237 (2001).

[2] J. Nührenberg, R. Zille, Phys. Lett. A **129** 113 (1988).

[3] S. Gori, W. Lotz, J. Nührenberg, Theory of Fusion Plasmas (International School of Plasma Physics), Bologna: SIF 335 (1996).

[4] W.A. Cooper, M.Yu. Isaev, M.F. Heyn et al., "New schemes for confinement of fusion products in stellarators" IAEA conference, Lyon, France, 2002.

[5] W.A. Cooper, S. Ferrando i Margalet, S.J. Allfrey et.al. Plasma Phys. and Controlled Fusion **44** B357 (2002).

[6] M.I. Mikhailov, V.D. Shafranov, A.A. Subbotin et.al., Nuclear Fusion **42** L23 (2002).

[7] S.P. Hirshman and O. Betancourt, J. of Comput. Physics **96** 99 (1991).

[8] J. Nührenberg, R. Zille, Theory of Fusion Plasmas (Varenna 1987), Editrice Compositori, Bologna 3 (1988).

[9] J.L. Johnson, K. Ichiguchi, Y. Nakamura, M. Okamoto, M. Wakatami, N. Nakajima, Phys. Plasmas **6**, 2513 (1999).

[10] K.C. Shaing and J.D. Callen, Phys. Fluids, **26** 3315 (1983); N. Nakajima and M. Okamoto, J. Phys. Soc. Jpn. **61** 833 (1992); K.Y. Watanabe et al., Nuclear Fusion **35** 335 (1995).

[11] V.D. Shafranov, W.A. Cooper, M.Yu. Isaev et al., 30th EPS Conf. on Controlled Fusion and Plasma Physics, St. Petersburg, (2003).

Observation and modelling of the anomalous particle pinch in TCV

H.Weisen, A. Zabolotsky and TCV Team

Centre de Recherches en Physique des Plasmas,
Association EURATOM - Confédération Suisse, EPFL, 1015 Lausanne, Switzerland

Introduction. Moderately peaked electron density profiles are observed in virtually all plasma conditions in TCV. The behaviour of the density profiles from a database of 300 Ohmic and ECH/ECCD discharges is compared to predictions of models based on the Ware pinch, the anomalous curvature pinch (or Turbulent Equipartition) and Turbulent Thermodiffusion (TTD). The database covers a wide range of plasma conditions:
$1 < \kappa_a < 2.6$, $0.5 < \delta_a < 0.7$, $2 < q_{95} < 7$, $1.2 \cdot 10^{19} m^{-3} < n_e < 12 \cdot 10^{19} m^{-3}$, $0.02 < \nu^*_{75} < 10$, $0.1 < T_i/T_e < 0.8$, where κ_a and δ_a are the elongation and the triangularity at the LCFS and ν^*_{75} is the electron collisionality at 75% of the poloidal flux.
The behaviour of stationary sawtoothing Ohmic plasmas, where the density profile widths $\langle n_e \rangle / n_e(0)$, ($\langle\ \rangle$ volume average) scales with the current profile width parameter $\langle j \rangle / (j_0 q_0)$ and can be modelled reasonably well by either of the three above mechanisms, using suitable choices of the transport parameters. The scaling parameter $\langle j \rangle / (j_0 q_0)$ is a generalisation of the historical scaling parameter $1/q_a$ for circular cross sections [1]. With high power ECH ($P_{ECH} >> P_{OH}$) the peaking of the density profiles is reduced, especially at low values of $\langle j \rangle / (j_0 q_0)$. The peaking remains however significant and cannot be modelled with the Ware pinch alone, unless $D << \chi_{eff}$ is assumed. The inadequacy of a pure Ware pinch model is unambiguously demonstrated by the observation of peaked density profiles in stationary, fully relaxed, fully current driven ECCD discharges with $V_{loop}=0$. A satisfactory description throughout the database can however be obtained by combining an anomalous pinch with the Ware pinch.

Observations and modelling principles.
Figs.1 & 2 show the widths of the density profiles $\langle n_e \rangle / n_{e1}$, where n_{e1} is the density at the sawtooth inversion radius for the Ohmic and ECH datasets. The Ohmic density profiles scale with $\langle j \rangle / (j_0 q_0)$, whereas profiles with ECH are broader, especially at low values of $\langle j \rangle / (j_0 q_0)$. Plasma shape has no direct effect [1]. The absence of a scaling with $\langle n_e \rangle$ shows that density peaking is not explained by neutral penetration. From the diffusive-convective transport equation, $\Gamma = V n_e - D \nabla n_e$ we obtain a generic model for steady-state density profiles, for the three processes

$$\frac{\nabla n_e}{n_e} = \frac{V_{Ware}}{D} + \alpha \frac{\nabla T_e}{T_e} - \eta \frac{\nabla q}{q}$$

The diffusion coefficient D is assumed to be proportional to χ_{eff}, as determined from the heat balance equation.

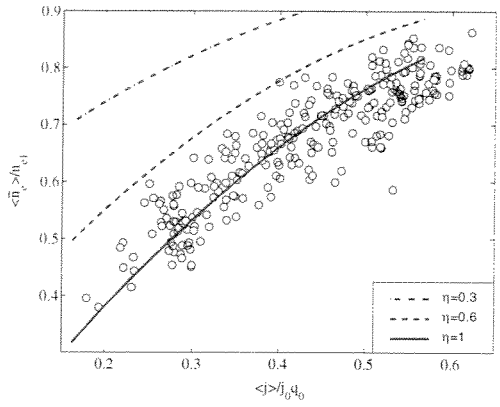

Fig.1 Scaling of density profile widths in OH plasmas with current profile peaking factor.

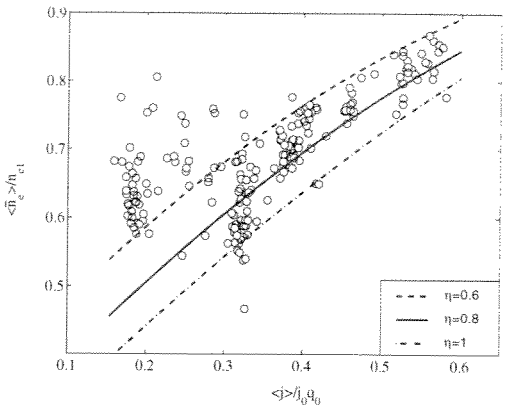

Fig.2 Scaling of density profile widths with current profile peaking factor with ECH.

Ohmic plasmas are reasonably well fitted by a pure Ware pinch model, assuming D/χ_{eff}~0.25 (lines in fig.3). With this ratio, however, ECH heated plasmas are predicted to have excessively flat profiles. A pure Ware pinch model can also not explain density peaking in a fully current driven plasma as in fig.4. For this experiment the Ohmic transformer current was kept constant ($E_{//}$=0) for 4 seconds by feedback, far longer than the measured current profile redistribution time (0.5s), whilst the density profile remained unchanged.

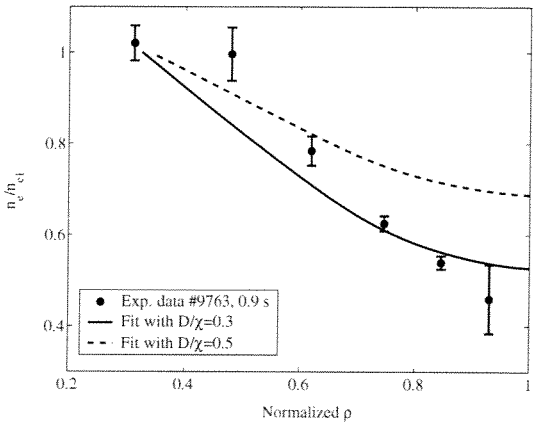

Fig.3 Ware pinch model prediction for scaling of density profile widths in OH plasmas.

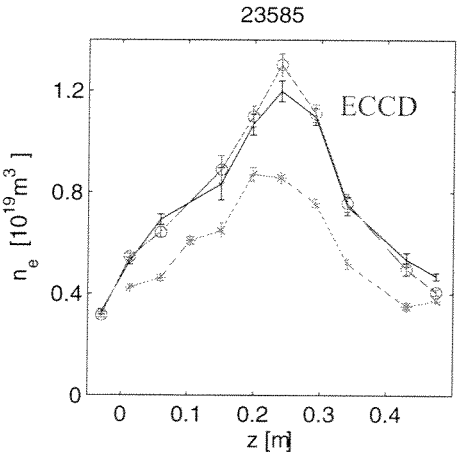

Fig.4 Profiles of 100kA fully ECCD discharge (red, blue) and of Ohmic target (green).

TTD alone, with $\alpha \approx 0.5$, provides a good fit for the Ohmic dataset (lines in fig.5) as well as of ECH plasmas, when the shape of the electron temperature profile does not depart from the Ohmic case. However with strong central ECH, T_e profiles can steepen up considerably without a corresponding steepening of the n_e profile. This would require a lower value of α in the core.

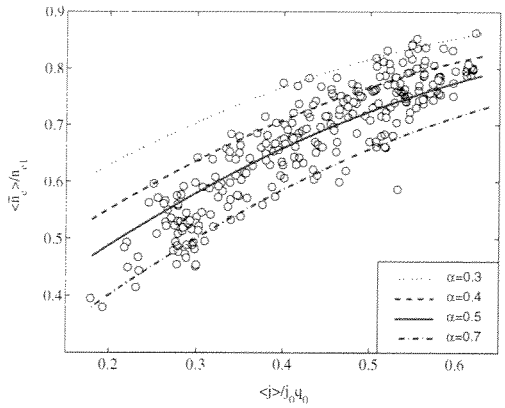

Fig.5 Prediction for scaling of density profile widths in OH plasmas by pure TTD.

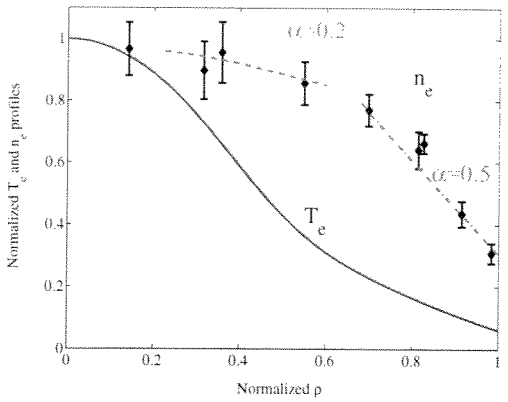

Fig.6 Profiles of ECH discharge exhibiting different L_n/L_{Te} in core and in periphery.

Turbulent Equipartition (TEP) is based on the hypothesis of conservation of the 2nd adiabatic invariant during turbulent transport. This leads to density profiles roughly proportional to $(q\partial V/\partial\Phi)^{-\eta}$ with $0.3\leq\eta\leq1$ depending on the relative contributions of trapped and passing particles to transport [3]. The fluid equivalent of TEP is the curvature pinch [4]. TEP provides good fits to the density profiles, with $\eta\approx1$ in Ohmic plasmas [1]. The broader profiles with ECH correspond to $0.6\leq\eta\leq1$ for $\langle j\rangle/(j_0q_0)>0.3$, but η can be as low as 0.3 with high ECH power and $\langle j\rangle/(j_0q_0)<0.3$.

None of the three processes on its own can describe the entire Ohmic and the ECH dataset satisfactorily with a fixed coefficient. Combinations of an anomalous pinch, such as TEP together with the Ware pinch are however fairly successful for the dataset of sawtoothing plasmas, as shown in figs.7 & 8 [2]. In these models, density peaking in plasmas with high ECH power, which have low $E_{//}$ and high D, is dominated by the anomalous pinch.

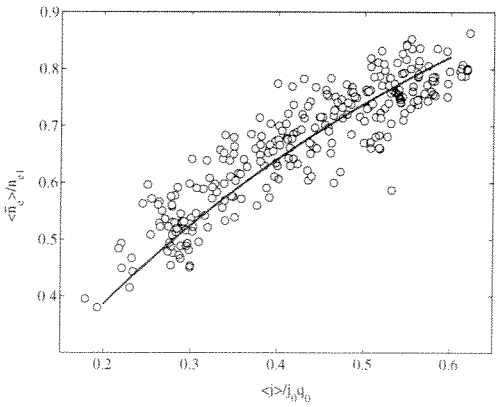

Fig.7 Scaling of $\langle n_e\rangle/n_e(0)$ in OH plasmas with $\eta=0.45$, $D/\chi_{eff}=0.4$ and $\alpha=0$.

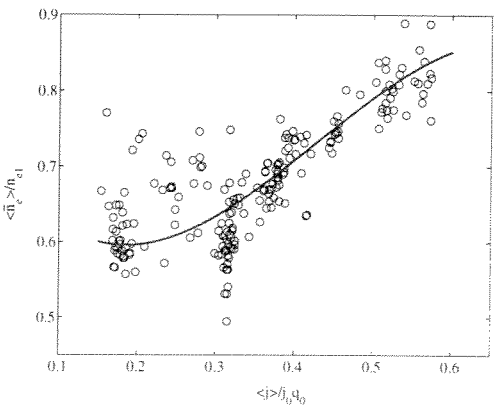

Fig.8 Scaling of $\langle n_e\rangle/n_e(0)$ in ECH plasmas with $\eta=0.45$, $D/\chi_{eff}=0.4$ and $\alpha=0$.

Internal transport barriers with reversed shear

In TCV ITB's can be produced either by central counter current drive or fully non-inductively by off-axis co-current drive [5]. Both of these methods produce a reversed shear in the core region. When MHD-quiescent, these plasmas have monotonic, peaked density profiles, which are not consistent with TEP, but may be described by thermodiffusion with $\alpha \leq 0.2$, as shown in the example of fig.9 a&b [6]. Since transport is reduced in ITB's this may correspond to neoclassical, rather than turbulent thermodiffusion. Another hint that neoclassical thermodiffusion may be important in the core comes from the observed reversal of the direction of the convective velocity when the core is helically perturbed by a large (m,n)=(1,1) mode and hollow density profiles are produced irrespective of the sign of shear [6]. Outward Thermodiffusion convection is predicted by neoclassical theory in non-axisymetrical configurations.

Fig.9

Electron temperature (a) and density (b) profiles in a quiescent reversed shear ITB plasma produced with 1.3 MW on-axis counter ECCD and 0.9 MW off-axis ECH.

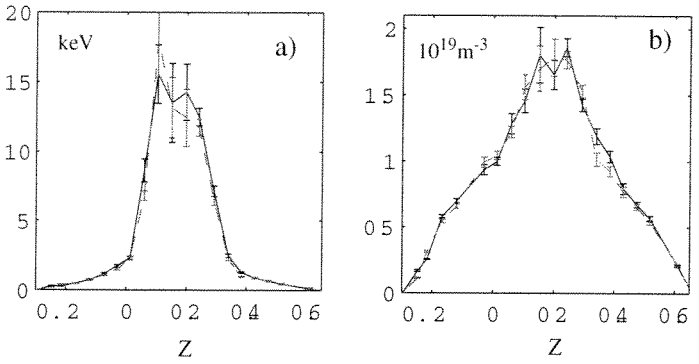

Summary discussion

The Ware pinch alone cannot explain peaked density profiles in full ECCD plasmas. Combinations of the Ware pinch with TEP and/or TTD successfully for modelling most sawtoothing plasmas. The existence of thermodiffusive convection is suggested by reversed shear plasmas which have normally peaked density profiles. Since the wide variety of plasmas considered may include more than one turbulence regime, different processes may contribute in variable proportions to the resulting density profiles. Additional effects to be considered include neoclassical pinches due to the fast electron produced by ECCD, as well as neutral penetration, which may be important at low density.

References

[1] H. Weisen et al, *Nuclear Fusion* **42** (2002) 136 *

[2] A. Zabolotsky et al, *Plasma Phys. Contr. Fusion* **45** (2003) 735 *

[3] D.R. Baker & M.N. Rosenbluth, *Phys. Plasmas* **5** (1998) 2936

[4] X. Garbet et al., accepted for *Physical Review Letters* (2003)

[5] R. Behn et al, poster P-3.208, http://crppwww.epfl.ch/archives/conf2003.htm#behnc03

[6] I. Furno et al, *Phys. Plasmas* **10** (2003) 2422 *

* preprints available at http://crppwww.epfl.ch/~weisen/publications/publication_abstracts_downloads.html

Influence of Non-Maxwellian Velocity Distributions during ECCD on Electron Temperature Measurements by Thomson Scattering

G. Zhuang, R. Behn, O. Sauter, P. Nikkola

Centre de Recherches en Physique des Plasmas,
Association EURATOM-Confédération Suisse, EPFL, CH-1015 Lausanne, Switzerland

Introduction

The absorption of electron cyclotron (EC) waves at high power densities (more than 10 MW/m^3) during EC heating and current drive generates a population of fast electrons and therefore may lead to a significant modification in the electron velocity distribution function. Since thermodynamic equilibrium can no longer be assumed, the approximation by a Maxwellian distribution function becomes questionable. This has to be taken into account for the interpretation of the data from incoherent Thomson scattering, which has become the standard method for measuring the electron temperature and density in a tokamak. Normally the spectral distribution of the scattered light intensity is interpreted on the basis of a Maxwellian velocity distribution.

In this paper a few cases will be investigated, which are representative of ECH and ECCD experiments on the TCV tokamak. Numerical simulations have been performed using a Fokker-Planck code (CQL3D) to obtain the expected velocity distribution functions for each case. These distribution functions are then used to calculate the spectra of scattered radiation for the particular conditions of the Thomson scattering diagnostic on TCV. The comparison with the spectra obtained under the assumption of a Maxwellian distribution will show whether the distortion also affects the low energy part which is analysed to obtain the electron temperature. In the case of significant deviations, an estimate of the systematic error in the analysis of the Thomson scattering data is given.

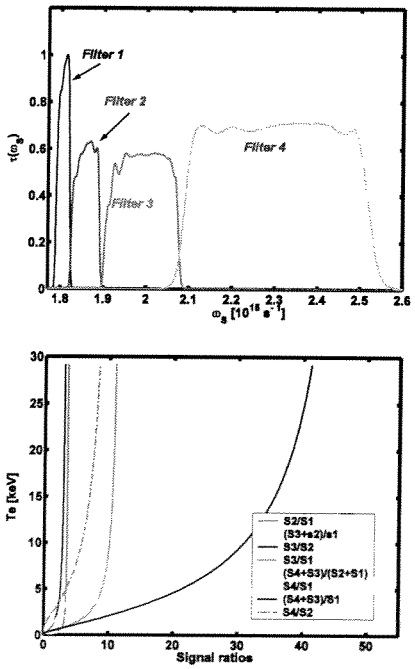

Fig.1. ***Top****: Spectral Response functions for a spectrometer with 4 filters.* ***Bottom****: Conversion functions for the measurement of T_e from signal ratios*

Thomson scattering system on TCV

The Thomson scattering system on TCV has been designed to measure T_e and n_e in 25 points within a poloidal cross section. Due to the chosen geometry, the differential k vector has only a very small component in the toroidal direction. For analysis of the scattered light spectrum, spectrometer equipped with 3 or 4 wide-band spectral filters are used. Fig.1 shows the 'Spectral Response Functions' $\tau(\omega_s)$ of 4 filters. The detector behind each filter receives the scattered intensity inside a specified band $P_{f\,\mathrm{hom}} \propto \int \tau(\omega_s) S(\omega_s) d\omega_s$, where $S(\omega_s)$ - spectral density function - describes the spectral distribution of the scattered light. Usually, the

spectral density function is calculated assuming a Maxwellian velocity distribution function with the electron temperature as free parameter. For a given set of filters, the ratios of signals from different spectral channels can be calculated and tabulated as a function of T_e. In this way single valued conversion functions are obtained permitting a simple and fast measurement of the electron temperature.

The CQL3D code

The CQL3D Fokker-Planck code solves the bounce-averaged Fokker-Planck equation in two velocity dimensions $(v_\perp, v_\parallel)$ and one radial coordinate ρ. The code accepts the main plasma parameters (T_e and n_e) as the simple input variables. The ray paths of EC beams are derived by TORAY-GA, and local power densities are calculated self consistently. It has been adapted to include radial diffusion of electrons. This code is widely used to analyse cases of EC heating and current driven in TCV and its predictions are usually found in good agreement with experimental results.

Calculation of T_e using different distribution functions

Thomson scattering measurements on TCV provide signals from 4 spectral channels (filters) for each observation point. Using up to 8 combinations of signal ratios, 8 T_e values may be obtained from the conversion functions. Ideally, these values should be identical, but noise in the signals or systematic errors will lead to deviations, which are expressed by an ''error bar'' (uncertainty interval).

For a numerical simulation of the measurement using different velocity distribution functions $f(\vec{v})$, we first compute the spectral density function $S(\omega_s)$ [1]. Artificial ''signals'' are then obtained by integrating $S(\omega_s)$ over the filter pass band. Thus, another set of signal ratios is generated and converted into temperatures using the conversion functions described above. As distribution functions we have used either the ideal Maxwellian distribution function (including relativistic effects) or the 3D distribution function $f(v_\perp, v_\parallel, \rho)$ provided by the CQL3D code. Since the geometry of the TCV Thomson scattering restricts the measurements essentially to the perpendicular velocity component, we also used the simplified function $f(v_\perp)$, which neglects the anisotropy contained in $f(v_\perp, v_\parallel)$.

The simulations based on the model of a relativistic Maxwellian distribution function for the particular T_e should reproduce this value independently of the signal ratio used. Here it will be used to verify the analysis procedure and set a reference for comparison with the results using other distribution functions.

Ohmic heating and EC heating cases

As a typical case we choose TCV shot (#19424) with an injected power of 0.9 MW for off-axis EC heating during 0.4s-1.8s. Two time points, one is 0.35s, the other 1.0s, have been selected to represent the 'Ohmic heating' and 'EC heating' case respectively.

For Ohmic heating only, we do not expect a deviation from a Maxwellian distribution function. Nevertheless, the same procedure has been applied to obtain $f(\vec{v})$ from CQL3D, which, indeed, is indistinguishable from a Maxwellian.

In case of EC heating phase, the differences in the spectral density functions derived by the model Maxwellian and $f(v_\perp, v_\parallel)$ or $f(v_\perp)$ from CQL3D are extremely small. As shown in Fig.2 (a), small discrepancies can be seen between the simulated and measured signals. However, these differences are within the uncertainty of the measurement. It should be noted

that the experimental T_e values obtained from the different signal ratios are not identical, but lie within a 5% margin of the Maxwellian model. This may be regarded as the typical uncertainty range of the experimental measurement. From these results we conclude that for the given EC heating power, there is already a small deviation from the Maxwellian distribution in the low energy part. Also, anisotropy of the distribution function starts to play a role. However, the effects are small and cannot be resolved by the Thomson scattering system installed on TCV.

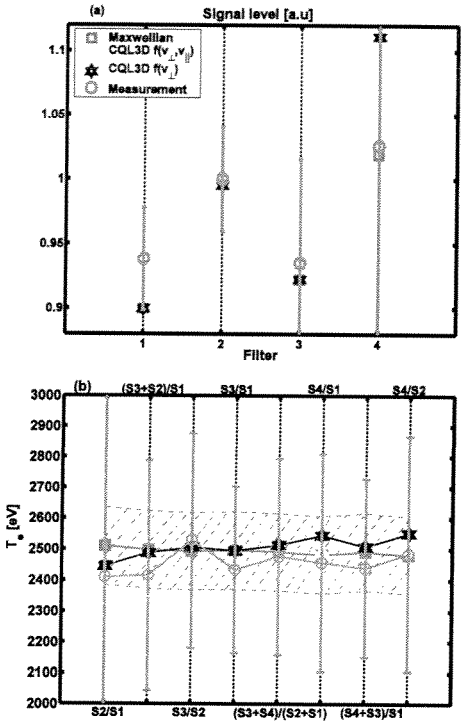

Fig.2. (a) Comparison of the theoretical signals of 4 filters computed by the suggested distribution functions and the measured ones of 4 filters. Note that signals of filter 4 are multiplied 10. (b) Te values derived by different signal ratios. Note that the 'red' shadow covers the 5% range of the Maxwellian estimated Te values.

ECCD scenario

ECCD scenarios rely on the generation of a high energy tail in the velocity distribution function. The effect on the low energy part is less obvious and it is not clear a priori to what extent Thomson scattering measurements may be affected. During the representative TCV shot (# 18532), 3 gyrotrons (1MW off-axis CO-ECCD, 0.5MW central CO-ECCD) with the same toroidal launching angle of 24° have been used to drive a plasma current of 165kA. For the analysis we have chosen signals from 3 spatial channels (Nos. 9, 8, and7 near the plasma centre) at t=1.75s during the stationary ECCD phase.

As shown in the Fig.3 (a-c), the spectral density based on $f(\vec{v})$ from CQL3D clearly deviates from a Maxwellian. The differences are largest within the pass bands of filters 1,3 and 4. This also can be seen in the signal levels shown in Fig.3 (d). The interpretation of the signal ratios using the conversion functions (based on a Maxwellian) leads to discrepancies in the resulting T_e values, which depend on the particular ratio used. As seen in Fig.3 (e), the different ratios do not give the same T_e value. This tendency is seen on all 3 spatial channels (7,8, and 9). It turns out that the experimental data set produces very similar results to that obtained on the basis of $f(\vec{v})$ calculated by CQL3D. We concluded that the results from CQL3D provide a better description of $f(\vec{v})$ than the assumption of a Maxwellian. In this situation, the systematic error is best quantified by considering energies rather than temperatures. For the particular case the total electron energy, integrated over the distribution function contributed by CQL3D, is 20-30% higher than that obtained from a Maxwellian at the given temperature.

Summary and conclusions

Results from a series of cases, which are representative of ECH and ECCD experiments on the TCV tokamak, have been presented. For the EC heating case, it is shown that the

electron velocity distribution function is only weakly perturbed and the induced error in T_e measurements by Thomson scattering can be estimated to about 5%, which is of the same order as other experimental uncertainties. For the ECCD case, the perturbation of the distribution function was found to be more pronounced. The deviation from a Maxwellian becomes significant and the usual interpretation of the data by conversion functions leads to systematic errors. For a case representative for ECCD experiments on TCV, the calculations based on results from CQL3D have led to 20-30% higher electron energies. Observed discrepancies in T_e values obtained from different signal ratios may be used as an indicator for a non-Maxwellian distribution function.

References:

[1] T. Matoba, *et al*, Jap. J. Appl. Phys. 18, 1127(1979)

This work was partly supported by the Swiss National Science Foundation

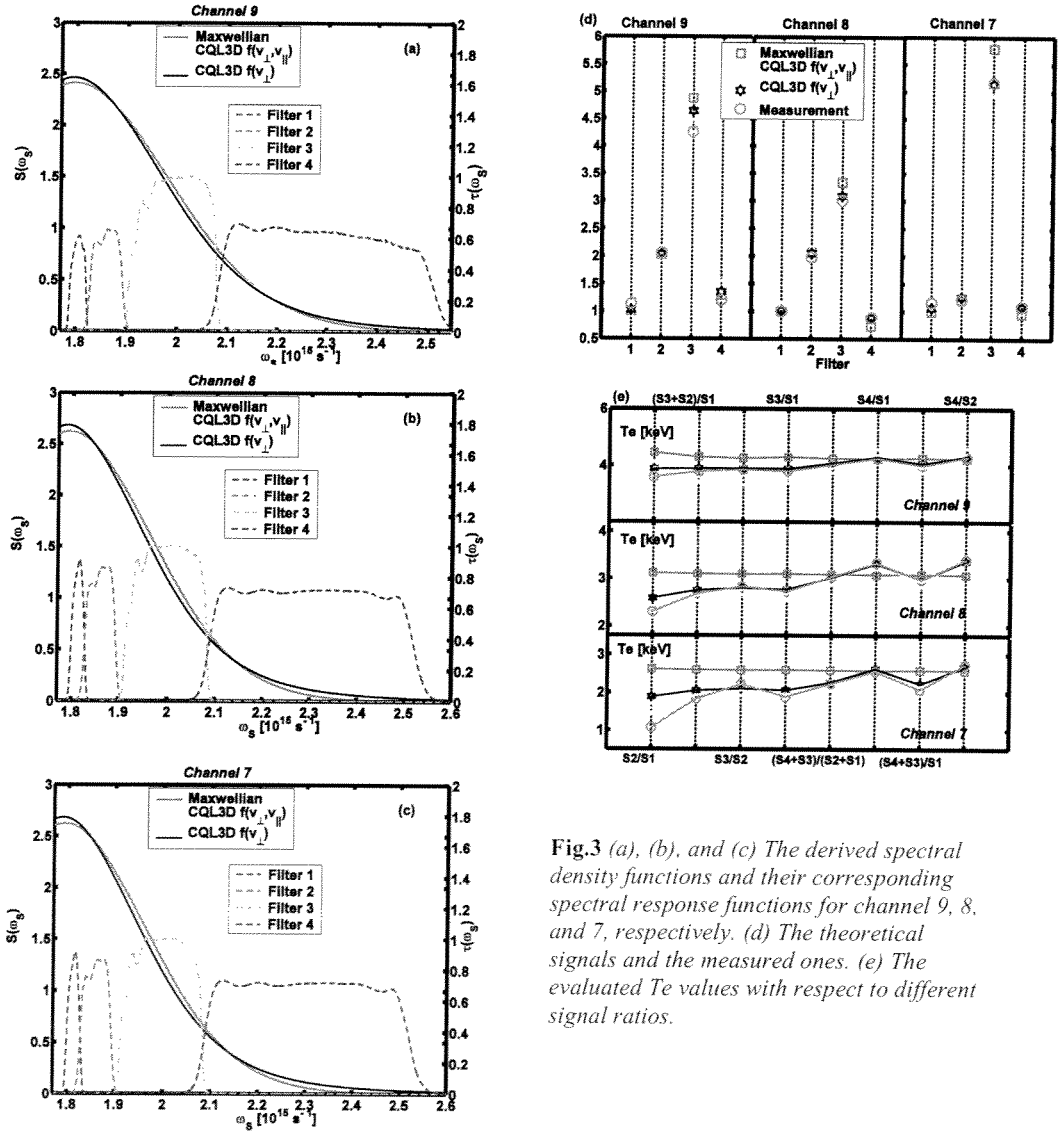

Fig.3 *(a), (b), and (c) The derived spectral density functions and their corresponding spectral response functions for channel 9, 8, and 7, respectively. (d) The theoretical signals and the measured ones. (e) The evaluated Te values with respect to different signal ratios.*